# Multiple Memory Material Processing for Augmentation of Local Pseudoelasticity and Corrosion Resistance of NiTi-based Shape Memory Alloys

by

Jeff Wang

A thesis
presented to the University of Waterloo
in fulfillment of the
thesis requirement for the degree of
Master of Applied Science
in
Mechanical Engineering

Waterloo, Ontario, Canada, 2013

## Declaration

I hereby declare that I am the sole author of this thesis. This is a true copy of the thesis, including any required final revisions, as accepted by my examiners.

I understand that my thesis may be made electronically available to the public.

## Abstract

Possessing unique thermomechanical properties, the discovery of nickel-titanium shape memory alloys (SMAs) has sprouted a plethora of applications in various fields, including aerospace, automotive, microelectronics, and medical devices. Due to its excellent biocompatibility and its ability to mimic biological forces, the medical implant industry has shown strong interest in expanding the application of NiTi SMAs. However, traditional SMA functional properties are limited by a single set of thermomechanical characteristics in a monolithic component. Past efforts in overcoming this limitation have had little success until recently with the invention of the multiple memory material (MMM) processing technology. This novel processing technology enables multiple functional responses through the augmentation of local microstructure and composition using a high power density source such as a laser. This thesis presents an investigation of the effect of laser processing on pseudoelastic behaviour and corrosion response of medical grade SMAs.

Partial laser processing of ternary NiTiCu SMA wires was studied to investigate the influence of this novel processing technique on the crystallography, composition, phase transformation temperatures, and mechanical properties. Application of laser energy through pulsed fibre laser was shown to partially solutionize the base metal, removing its cold work and causing two different deformation mechanisms within a single monolithic wire. It was found that, following laser processing, pseudoelastic forces were able to be controlled by adjusting laser parameters and could be predicted using a phenomenological model. Although more work is needed to understand the exact deformation mechanisms, this extension of the MMM technique offers high resolution and precise pseudoelastic force tuning which, until now, has not been possible.

In order to understand the corrosion behaviour of the laser processed surface independent of the base metal, a careful study was carried out to investigate the surface composition and corrosion response of NiTi strips. Ti-rich NiTi alloys were fabricated from Ni-rich alloys by partial melting and ablation. The resultant surface had significantly lower corrosion rate and decreased reactivity. The Ni ion release was also decreased. The improvement in corrosion response was attributed to the slight increase in oxide thickness and the decrease in surface Ni concentration, identified through X-ray photoelectron spectroscopy (XPS) and electron dispersion x-ray spectroscopy (EDS).

## Acknowledgements

I would like to thank my supervisor, Dr. Y. Zhou, for his support, guidance, and excellent life advice during my research. The freedom in research and connection to industrial applications has kept me highly motivated during the course of my studies.

I would also like to thank the current and past members of the microwelding group: Dr. Ibraheem Khan, Andrew Pequegnat, Yongde Huang, Matthew Daly, Boyd Panton, and Siu Kei Tang, as well as other students at the Centre for Advanced Materials Joining. I would like to give special thanks to Andrew for his help with revision of this thesis.

# Table of Contents

## List of Figures

## List of Tables

## List of Equations

# Chapter 1

## 1. Introduction

The application of shape memory alloys (SMA) in industry has greatly increased since the discovery of nickel titanium (NiTi) in 1963 by Buehler et al. [1]. The strong demand for application is thanks to its excellent strength, ductility, biocompatibility, and its superior functional properties. The unique functional properties of SMA have the ability to respond and convert input energy (i.e. temperature or stress) into meaningful mechanical work in an elegant and compact manner. The shape memory effect (SME) allows the alloy to recover its original shape by the application of thermal energy, even after large deformation approaching 10 % strain. The pseudoelastic effect or pseudoelasticity (PE) of SMAs allows for large recoverable strains (i.e. 8 % in polycrystalline materials) simulating many of the mechanical response in the human body, such as the hair, bone, and tendons [2].

Recent research efforts have allowed deeper understanding of SMAs and their functional properties. Cutting-edge SMA devices are therefore now utilized in many applications of the automotive, aerospace, and biomedical industries [3, 4]. In the age of "green" initiatives and in the search of low mass, high work density, and biocompatibility, NiTi SMAs are emerging as the next-generation of programmable materials [5]. In particular on the medical front, SMAs have become an established material in applications such as medical stents (gastrointestinal and arterial) [6–8] and orthodontic archwires [9–11]. However, research efforts are now focused on increasing the functionality and customization of SMA devices in order to enhance their application [11–14].

## 1.1 Motivation

Since the discovery of NiTi SMAs in 1960s, metallurgists have been able to uncover the complex mechanisms behind various NiTi SMA phase transformations through rigorous microstructural analysis and simulation [16, 17]. It has been determined that the unique functional properties of NiTi are attributed to a reversible, thermo-elastic, and diffusionless phase transformation. However, difficulties arises in engineering with these alloys, as the SME, PE, and biocompatibility properties are extremely sensitive to the composition and thermo-mechanical treatments, including cold work, heat treatment and/or other necessary processes such as welding [17–21]. As a result, the manufacture of orthodontic wires and stents has been focused on changes in microstructure (i.e. thermomechanical treatments), composition (i.e. Ni, Ti, ternary elements) and precise modification of device dimensions [8, 22–25].

Remarkably, localized changes in composition and microstructure have now been realized as an opportunity for increasing the functionality of SMA devices. For example, with the recent development of the multiple memory material technology (MMM), a novel laser processing technique is employed to locally modify the thermo-mechanical property in a monolithic SMA component [26–28]. Using a high power density energy source it has been shown that local microstructure, and more importantly, composition can be modified to induce a change in phase transformation temperatures, leading to multiple stage actuations in monolithic SMA devices [29, 30]. Similarly changes in pseudoelastic properties have been suggested by Khan et al. [19]; however, this phenomenon has until now not been studied in depth. A detail understanding of the pseudoelastic augmentation would create a whole new dimension of customization of current SMA medical devices and open many doors to new design possibilities. At the same time, new corrosion behaviour has been reported for different laser welding process [31–33], and can be expected for this laser processing method as well. Therefore, the immense opportunities to increase functionality and corrosion performance of current SMA devices are the basis for this research project.

## 1.2     Objectives

The ability to modify the PE of NiTi-based SMAs for commercial medical applications requires a detailed investigation into the effects of laser processing on the mechanical, functional, and corrosion properties of these SMAs post-processing. The goal of the current thesis is to understand the changes in PE and corrosion performance of NiTi-based SMAs following laser processing operations. In more detail, the three main objectives of this thesis work are to:

1. Investigate the effects of partial penetration laser processes on alloy composition, crystallography, phase transformation characteristics, and functional properties.
2. Determine the relationship between laser processing parameters, laser processed zones, and the alteration in PE.
3. Identify the effects of laser processing on Ni ion release and associated corrosion resistance for medical grade NiTi sheets.

## 1.3 Thesis organization

The present work studies the effect of laser processing on the pseudoelastic property of NiTiCu and biocompatibility of both ternary NiTiCu and binary NiTi SMAs. Chapter Two presents a review of existing literature relating to SMA physical metallurgy, corrosion resistance, laser processing, and current direction in medical SMA technology. The augmentation of pseudoelastic force in SMAs through laser processing is presented in Chapter Three, addressing objective one and two. Metallurgical, mechanical, and thermomechanical responses of the laser processed SMAs are examined by scanning electron microscope, thermoanalytical instruments, x-ray diffraction, and tensile testing equipment. A phenomenological model of the pseudoelastic force modification is also presented. Chapter Four investigates the corrosion property of laser processed surface and base material separately in order to isolate the effect of galvanic coupling. Finally, a thesis summary, conclusions, and recommendation for future research are provided in Chapter Five.

## 1.4 Contributions

### 1.4.1 Journal publications

1. **Wang, J.,** Pequegnat, A., Zhou, Y. and Khan, M.I. (2013) "PE tuning in NiTiCu through fibre laser processing", (In preparation)

2. Pequegnat, A., Daly, M., **Wang, J.**, Khan, M.I. and Zhou, Y. (2012) "Dynamics actuation of a novel laser processed NiTi linear actuator", Special Issue: Smart Materials and Structures. 21, No.9, 094004. **Invited paper**.

3. **Jeff Wang**, Anming Hu, John Wen, Y. Norman Zhou, John Persic, (2010), "Thermal Stability and Thermite Mechanism of Coated Al Nanoparticles with CuO", *Journal of Physics and Chemistry of Solids, vol 72, June 2011, 620-625*

### 1.4.1 Refereed conference proceedings

1. **Wang, J.**, Pequegnat, A., Zhou, Y. and Khan, M.I. (2012), "NiTi corrosion and biocompatibility enhancement through localized microstructure modification", Proceedings of Materials Science and Technology Conference 2012, Biomaterials Science – Processing, Properties and Applications III, Pittsburgh, PA, USA, October 7 – 11, 2012.

2. Tam, B., **Wang, J.**, Pequegnat, A., Zhou, Y. and Khan, M.I. (2012), "Resistance microwelding of NiTi shape memory alloys wires", Proceedings of Materials Science and Technology Conference 2012, Joining of Advanced and Specialty Materials (JASM XIV), Pittsburgh, PA, USA, October 7 – 11, 2012.

# Chapter 2

## 2. Literature Review

## 2.1    Physical Metallurgy of NiTi SMAs

The SME was first discovered in Au-47.5%Cd [34] and InTl alloys [32, 33] in the 1950s, but it wasn't until the discovery of NiTi by Buehler et al.[1] of the Naval Ordinance Laboratory before SMA research and applications increased in popularity.  This popularity is partly due to the publicity given to NiTi thanks to its discoverers, and its superior mechanical properties and biocompatibility [16].

The NiTi shape memory alloy is a binary nickel titanium alloy with a near equiatomic composition [37].  NiTi alloys are considered an organized intermetallic compound (IMC).  As shown in Figure 2.1 [37], only above 903 K (630 °C) does Ni become soluble in Ti to form NiTi.  The solubility limit of Ti is close to 50% Ni and drops steeply below 50%, whereas in the Ni-rich side has a larger range of solubility up to roughly 55%.  In order to produce NiTi, the molten alloy must be rapidly quenched within the soluble range denoted by the red box.  The same is not true for Ti-rich NiTi alloy due to its low solubility.  Furthermore, Ti-rich species $Ti_2Ni$ is undesirable due to its poor mechanical properties, which for example often cause cracking during rapid solidification that is typically experienced during welding procedures [38].  Besides difficulty in production, poor performance is another reason that Ti-rich NiTi alloys are not common. On the other hand, there are however many useful stable Ni-rich IMCs.  The Ni-rich species, such as $Ni_4Ti_3$, $Ni_3Ti_2$, and $Ni_3Ti$, could be precipitated via aging treatments to customize functional characteristics of NiTi SMAs [39, 40].

Functional properties of NiTi SMAs are a result of a reversible solid-state phase transformation triggered by thermomechanical stimulation [41–43].   This involves a diffusionless martensitic transformation of the cubic B2 austenite phase to the monoclinic B19' martensite phase.  The crystal structures of the two phases are shown in Figure 2.2 [16]. The B2 austenite phase is of the CsCl cubic structure with lattice parameter of 0.3015nm, and the B19' martensite phase is of the monoclinic structure with lattice parameter of a = 0.2889, b=0.4120, and c = 0.4622 nm with a monoclinic angle ($\beta$) of 96.8°. Intermediate phase transformations can also exist which include the trigonal R phase [44] and orthorhombic B19 phase created by thermomechanical treatment or addition of a ternary elements [45, 46].  The details of R phase transformation are outside of the scope of this thesis; however, the B19 phase transformation will be discussed in more detail along with the effect of ternary alloying elements.
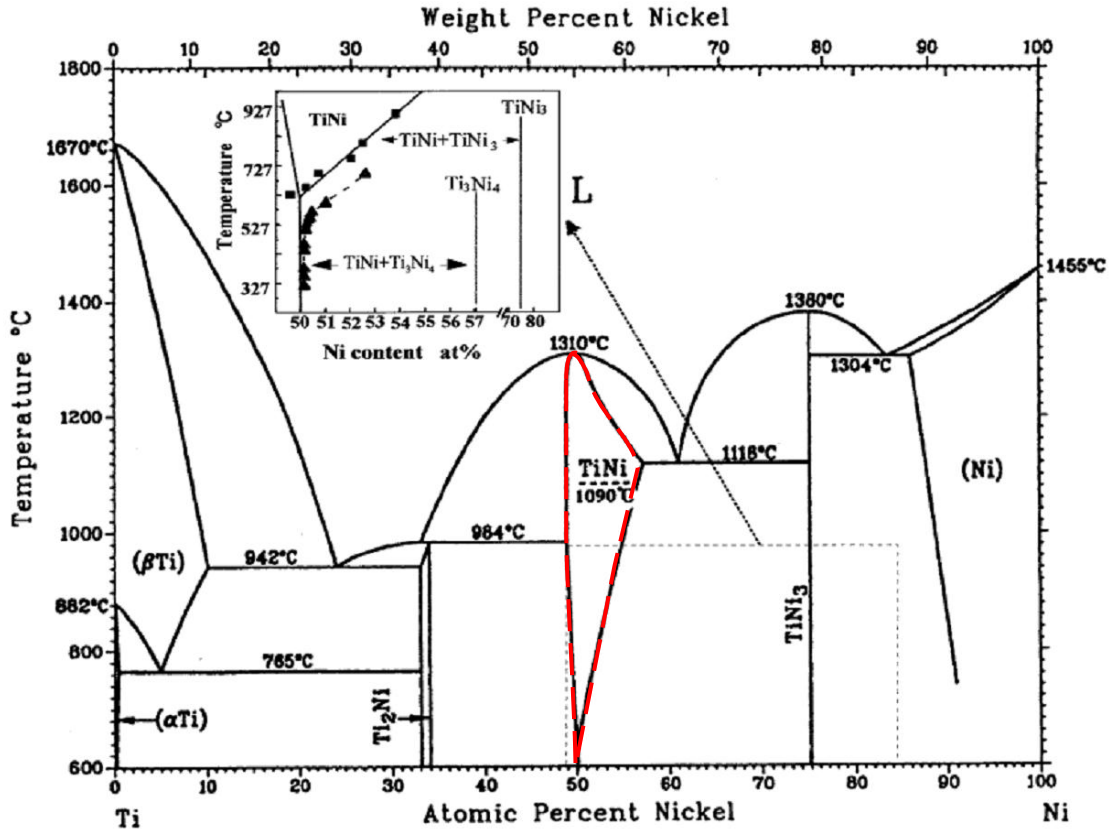
**Figure 2.1** Binary phase diagram of nickel-titanium with SMA range highlighted, taken from [37].
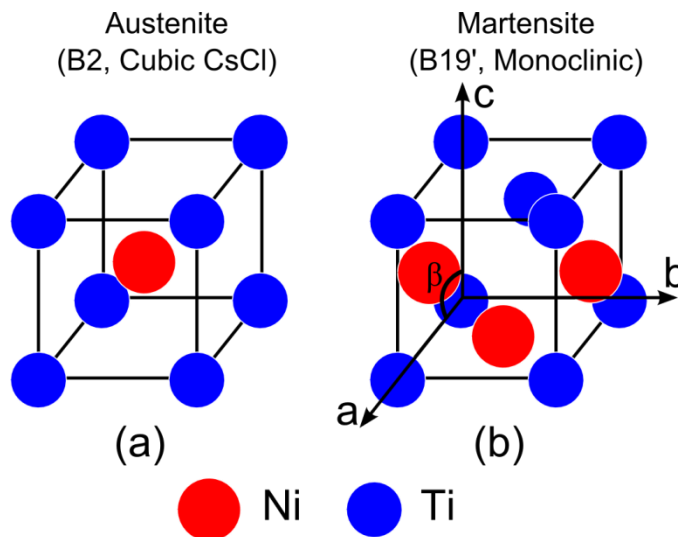


**Figure 2.2** Unit cells of NiTi (a) B2 cubic austenite phase and (b) B19' monoclinic martensite phase [16].

5

### 2.1.1    Reversible martensitic phase transformations and thermomechanical response

The austenite to martensite phase transformation can be divided into two parts, lattice deformation and lattice invariant shear.  Lattice deformation occurs when a small atomic shift occurs in the lattice, often less than one atomic spacing.  The second part, lattice invariant shear is an accommodation step resulting from the lattice deformation.  Illustrated in Figure 2.3 [41], the accommodation in volume and shape change can happen through slipping of the lattice or through twinning.  Slipping involves gliding of the atomic planes over high energy slip planes, creating irreversible dislocation and change in the crystal lattice.  FCC and BCC lattices are prone to slip due to a higher availability of slip systems and high stacking fault energies.  On the other hand, twinning is the shear of crystal lattice in which the structures on each side of the habit plane are mirrored and shifted less than one atomic spacing [41].  Martensitic transformation in NiTi SMAs accommodates the energetic change by twinning and shape change.
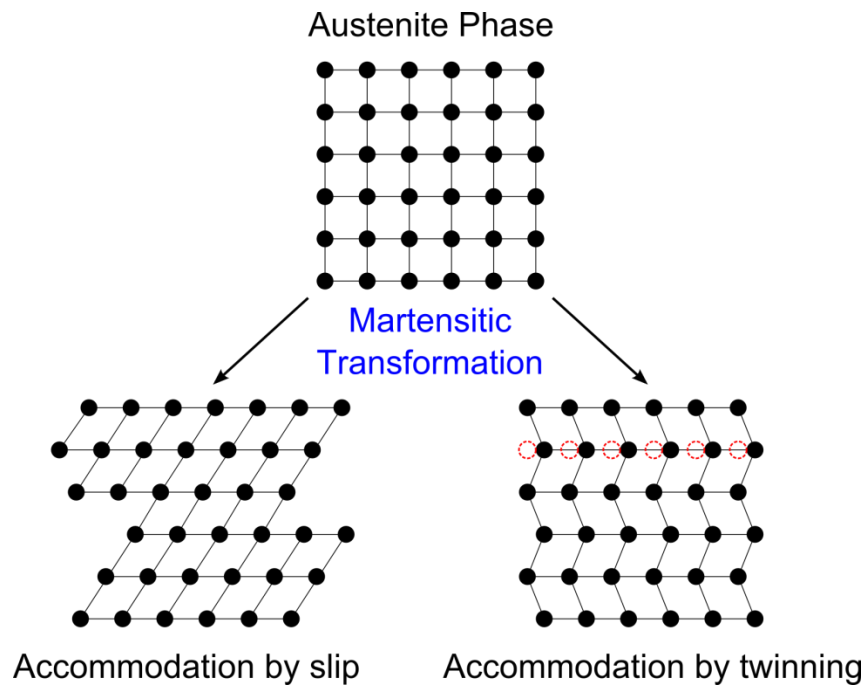


**Figure 2.3**  Stress accommodation of martensitic transformations by slip or twinning. Schematic adapted from [41].

Martensitic transformation can happen in three different paths depending on the alloying composition and aging treatments.  NiTi exhibits the B2 austenite to B19' martensite transformation when it has been solution treated or been through mild cold work and precipitation.   The ternary alloy, NiTiCu exhibits transformation from B2 austenite phase, to orthorhombic B19 phase, and then to B19' martensite. The B2 to B19 transformation is only observed when Cu compositions are above 7.5%, according to a

thermodynamic phase calculation [45, 47]. The effect of ternary alloying will be discussed further in later sections. The third path is from the B2 phase, to trigonal R phase, and then to B19' phase. The R-phase forms when the B19' martensite transformation is either suppressed by the Fe alloying element, dislocations created through cold work or Ni-rich precipitates following aging treatment [44, 48].

The B19' twinned martensite can further "detwin" to adapt to externally applied stress. Shown in Figure 2.4(a) [42], the detwinning processes occur as the twinned martensite variants slides to accommodate to the shear stress ($\tau$) and deform along the stress favorable orientation [42, 43]. Each different twin orientation is called a twin variant. In an ideal case, a single crystal martensite could detwin into a single variant as illustrated in step number three. The detwinning of the martensite can be observed in the tensile loading curve in the region of the low strain plateau. In Figure 2.4(b) [42], the stress and strain curve of the SMA is split into three parts. Number one is the elastic deformation of the twinned martensite. Number two, the plateau region, is when the sliding of the twin variants occurs. The yield stress behaviour can be attributed to the frictional stress between the twin boundaries, which are quite mobile. Since it does not deform by the generation of dislocations like typical metal alloys, the sliding stress of the twin boundary is constant. In the third section, upon full detwinning of the martensite variants, the martensite starts to elastically deform in the typical elastic-plastic manner. This deformation occurs at the martensite finish temperature, $M_f$, when the entire NiTi lattice is in martensite phase. Shape recovery behaviour begins when deformed martensite is heated above the austenite start temperature, $A_s$, and complete recovery occurs at the austenite finish temperature, $A_f$. Deformation and recovery is further detailed in section 2.2.1.

Twinned martensite can accommodate external stress through detwinning and this process can be reversed to restore the crystal lattice to the original configuration with little to no defects. The restoration process is called the reversible phase transformation, induced by a thermomechanical response to the stimulus in which martensite to austenite phase transformation occurs. This unique property enables storage of energy in the twin martensite lattice, and macroscopically, allows the lattice to *remember its shape*. This reversible phase transformation not only gives the alloy its name, but it is also critical to the functionality and industrial application of SMAs devices.
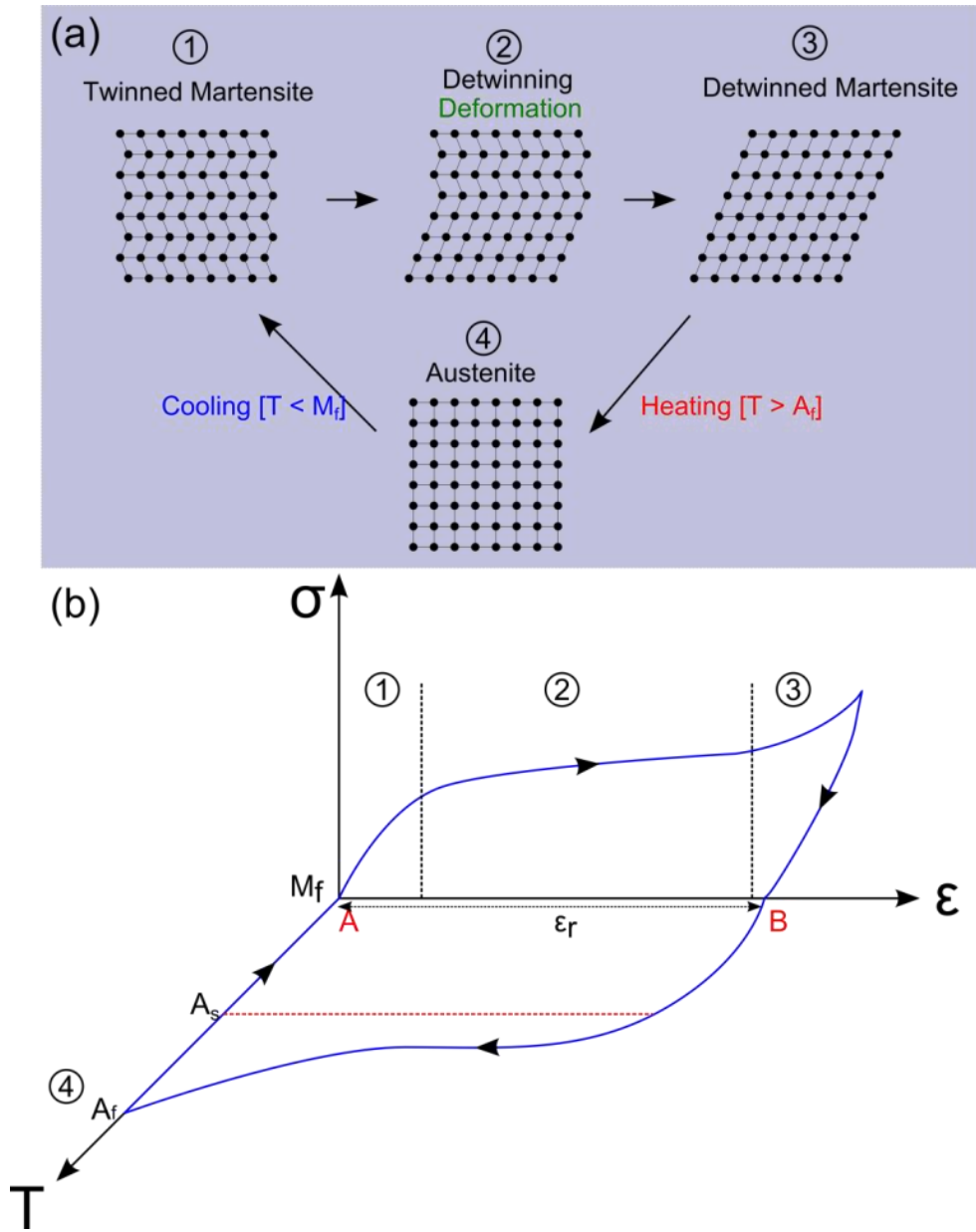
**Figure 2.4** (a)Illustration of lattice deformation and recovery during SME, (b) Stress-strain-temperature response during SME. Adapted from [42].

## 2.2 Functional properties of NiTi

The functional properties of NiTi based SMAs are a result of the special thermomechanical response of the NiTi lattice. The two functional properties, SME and PE, are the results of the thermally induced and stress induced austenite and martensite transformation, respectively [41–43]. The types of transformation occur depend firstly on the thermal stability of the austenite and martensite and secondly on the type of stress applied to the lattice. The following sections break down the scenario in which thermally induced transformation and stressed induced transformation take place.

8

### 2.2.1 Mechanism of SME

The shape memory phenomenon is a result of the thermally induced phase transformation. The austenite and martensite phases in NiTi are the stable lattice configurations within specific temperature ranges. Upon change in temperature, the NiTi lattice will respond and transform to its corresponding stable phase. To characterize the phase transformation temperatures, often differential scanning calorimetry (DSC) is employed following the ASTM F2004-05 standard. The heat flow analytical technique identifies four phase transformation temperatures: martensite start ($M_s$), martensite finish ($M_f$), austenite start ($A_s$), and austenite finish ($A_f$). The transformation temperatures are defined as the intersection of the tangents from the baseline heat flow and onset and completion of the exo- and endo-thermic phase transformation peaks.

Figure 2.5 shows a typical DSC curve of a fully solutionized NiTi SMA. Starting from the bottom heating curve in the figure, martensite phase is the preferred lattice structure. When the temperature reaches $A_s$, the twin martensite lattice transforms into austenite phase [49]. $A_f$ marks the end of the martensitic to austenitic transformation. During cooling, the austenite NiTi starts to transform into martensite at $M_s$ and completes the phase transformation at $M_f$. In the cooling process, between $M_s$ and $M_f$, both martensite and austenite co-exist, and the same is true for when temperature is between $A_s$ and $A_f$ during heating [43, 50]. The thermal hysteresis of the two transformations can be up to 50 °C in NiTi alloys [41]. The hysteresis is a product of the interfacial friction, defects, and the path of transformation. The width of the hysteresis can be controlled through Ni:Ti composition, alloying, cold work, and thermomechanical processing [51, 52].

The SME is defined as the ability of a material to remember a specific form factor, such that complete recovery is possible after apparent by plastic deformation. SME in NiTi alloys is made possible by the combination of the thermal response and the detwinning mechanics of martensite NiTi. Illustrated in Figure 2.4(a) is the simplified lattice deformation mechanism during the shape deformation and recovery, and the macroscopic deformation is illustrated in steps 1 to 3 of Figure 2.6. Under applied stress, the martensite lattice accommodates the force through detwinning in its preferred variants. In this detwinning process, the numerous crystallographic planes in the martensite grains slide with respect to one another less than one lattice spacing in the preferred direction. The apparent deformation in SME is a macroscopic manifestation of all the microscopic martensitic self-accommodations. NiTi is capable of deforming easily up to 8 % strain in polycrystalline materials [49]. From steps 3 to 4, the deformation recovery is induced by heating above $A_f$, during which the sheared martensitic variants (Figure 2.4(a), ③) recovers its B2 austenite lattice (Figure 2.4(a), ④) formation upon phase transformation. Once the restored austenitic NiTi is cooled below $M_f$, the SMA is returned to the martensite phase.
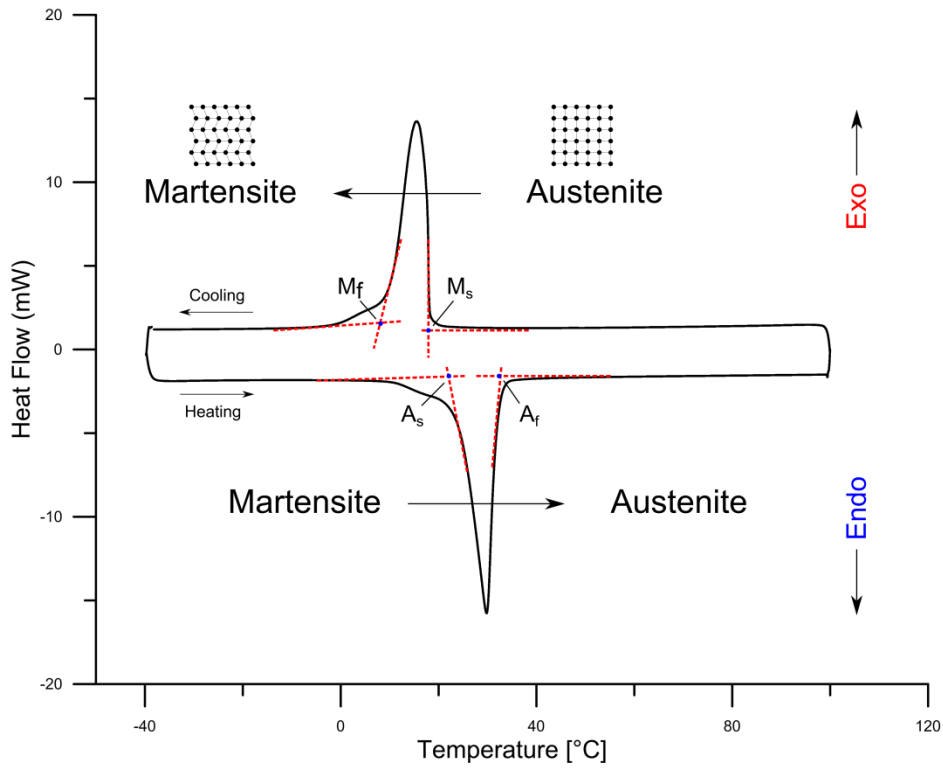
**Figure 2.5** A typical DSC plot for an solutionized NiTi alloy. Phase trnasformation temperature are the intersection of tangents of the phase change peak and base line heating curve.
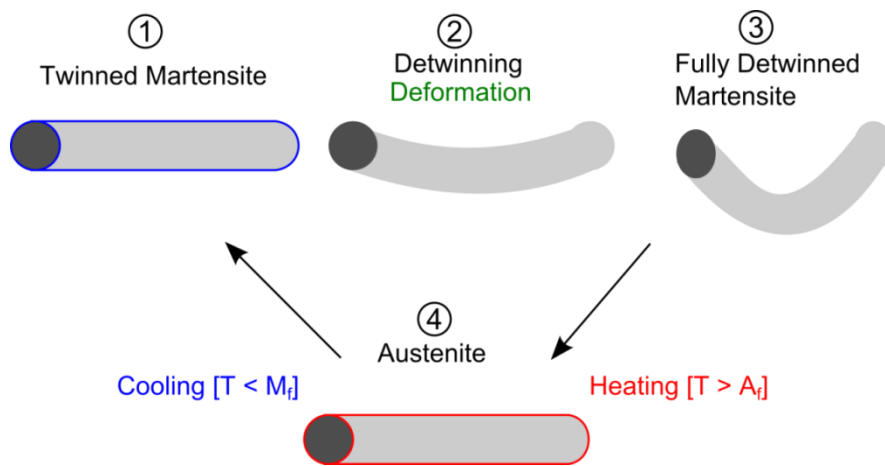


**Figure 2.6** Illustration of the macroscopic shape memory alloy deformation and recovery cycle.

### 2.2.2   Mechanism of the Pseudoelastic effect

The second functional property of shape memory alloy is PE; the ability to respond to external strain in an isostress manner. Similar to the SME, PE is enabled through a phase transformation from austenite to stress induced martensite (SIM). This transformation will only happen when the slip stress ($\sigma_s$) exceeds the stress required to form SIM ($\sigma_m$). Like the shape memory behaviour, the SIM undergoes a return transformation upon removal of stress. The condition can be created through typical hardening processes for metal alloys, including cold work on the order of 25% [53] and precipitation hardening through matrix coherent $Ti_3Ni_4$ intermetallic [54].

PE can be shown experimentally through tensile testing methods. Shown in Figure 2.7 is the typical cyclic tensile loading curve of austenitic NiTi. The PE is realized from the SIM in the forward loading curve from A to B, and from the return transformation in the unloading curve from B to A. There are three distinct regions in this cyclic loading curve: 1. Linear elastic regions of austenite; 2. phase transformation region; and 3. elastic region of the SIM. Austenitic NiTi behaves in the typical elastic deformation manner under stress prior to reaching $\sigma_m$. In region 2, initiation of stress-induced transformation begins when the load is greater than $\sigma_m$. At this load, the austenite phase starts to shear into SIM in an isostress fashion, following a Lüders-like deformation in which a shear band propagates across the specimen [55, 56]. Upon complete SIM transformation, the SIM again deforms in typical linear elastic manner. The characteristic maximum recoverable strain for NiTi is about 8% [57], any further straining causes the SIM to plastically deform. The SIM recovers first elastically after load has been removed, and then returns to austenite phase. A stress hysteresis is associated with the transformation, due to loading occurring at a higher stress than reversal force upon unloading.

The magnitude of the $\sigma_m$, also known as the pseudoelastic plateau, follows the Clausius-Clapeyron relation [58, 59] that increases proportionally with rise in temperature. The thermodynamic stability of the austenite phase increases further as the temperature rises above $A_f$, and thus the stress required to initiate the SIM transformation increases proportionally.
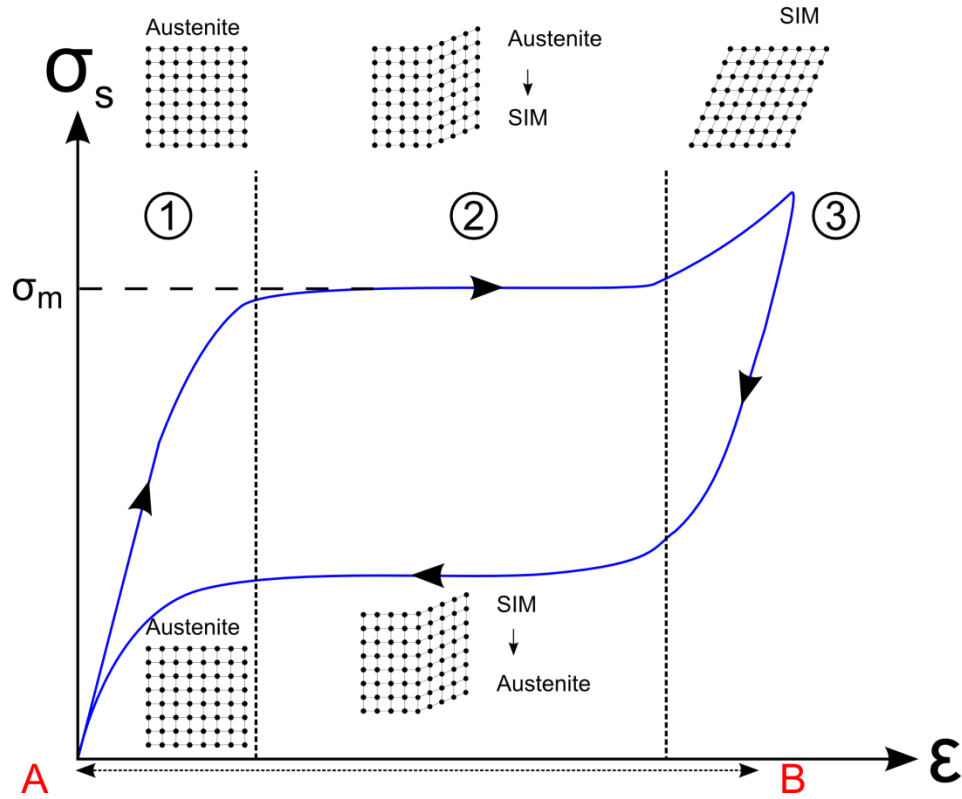
**Figure 2.7** Typical pseudoelastic tensile response of austenitic NiTi alloy with different stages of the stress induced transformation.

### 2.2.3 Conditions for functional properties through thermomechanical treatments

Both functional properties of NiTi SMAs are closely related phenomena enabled through phase transformations. Specific conditions in the lattice and temperature are needed for SME or PE to occur, as illustrated in Figure 2.8 [60]. For the temperature criteria, below $A_s$ the SME occurs with applied stress on twinned martensite, whereas above $A_f$, PE occurs with detwinned martensite stabilized under stress. Regarding the critical stresses for the lattice, the critical stress for slip can either be higher (A), or lower (B) than the critical stress to induce martensite, $\sigma_m$. For SIM to form and PE to be pronounced, the critical stress for slip must be higher than that of $\sigma_m$, such as scenario (A). In the case of (B), the strain on the austenite NiTi will be accommodated through the slip mechanism and result in permanent deformation [60]. The temperature dependent $\sigma_m$ follows the Clausius-Clapeyron relationship as mentioned earlier and reaches a maximum limit when intersected with critical stress for slip. Such intersection marks the maximum temperature, $M_d$, for SIM formation, above which permanent deformation will occur as critical stress for slip is smaller than $\sigma_m$ [60].
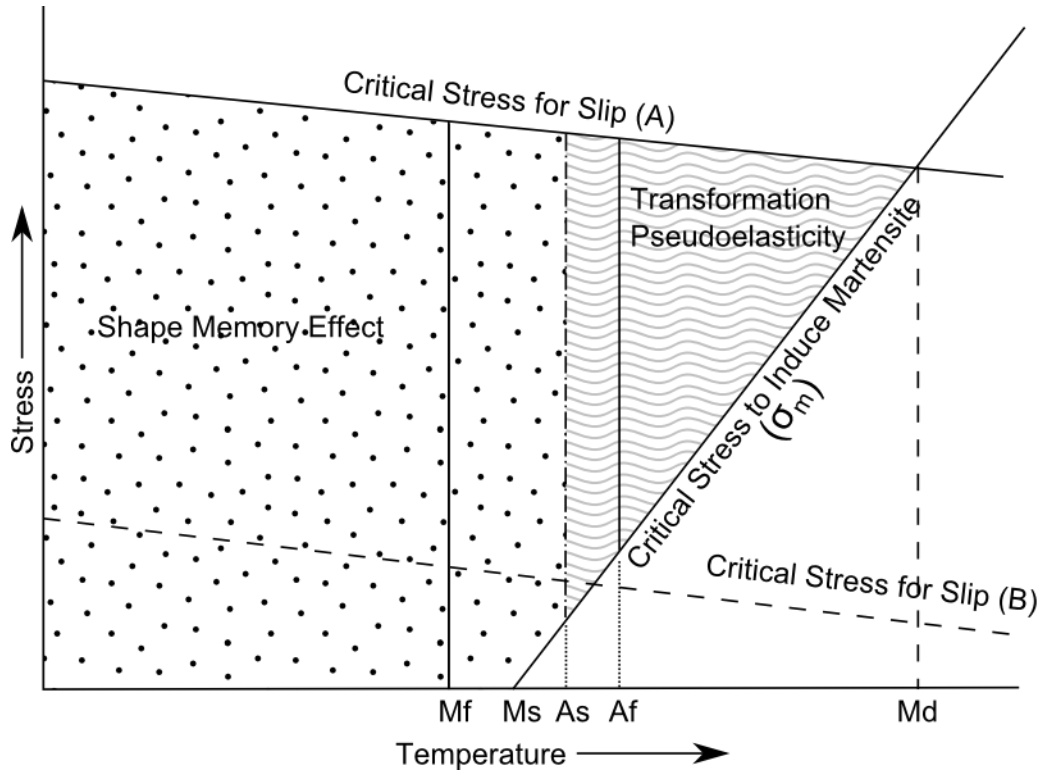
**Figure 2.8** Stress and temperature criteria and regions of activity for SME and PE in NiTi SMAs adopted from [60]

Several procedures can be used for engineering the characteristic stresses and transformation temperatures in the NiTi lattice, namely adjustment of alloying composition, aging heat treatment protocols, and cold working. Tang et al. [61] and later Frenzel et al.[51] conducted detailed studies on the effect of alloying ratio on the transformation temperatures. Shown in Figure 2.9 [51], the $M_s$ temperature increases with decreasing Ni ratio, from -60°C to 65°C within 1.5% change in composition [51]. High $M_s$ NiTi alloys with near 50 at% Ni are in the martensite phase at room temperature and suitable for SME actuator applications. Pseudoelastic applications, such as medical stents and flexible glasses frames, often use Ni-rich NiTi alloys with very lower $M_s$. Careful control of composition during casting is critically important in tailoring the transformation temperature for SMA applications. Aging heat treatment and cold work are equally important for IMC precipitation and strain hardening of the lattice, both of which increase the critical stress for slip and facilitate transformation from B2 → SIM rather than slip.
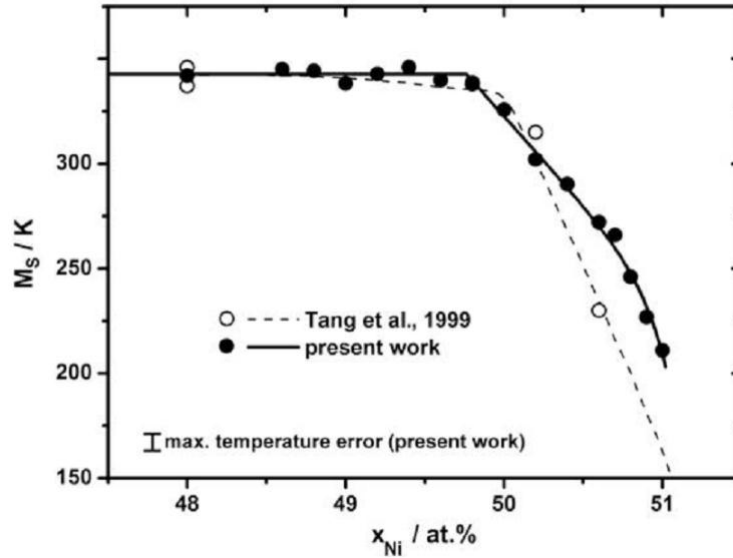
**Figure 2.9** Theoretical (dash) and experimental (solid) result of $M_s$ temperature in relation to NiTi atomic fraction of Ni, taken from [51]

### 2.2.4    Effect of Ternary alloying of Copper, NiTiCu

Addition of ternary elements similar in size to Ni and Ti can also be used to modify functional properties. Substitution of Ni with Co, Fe, Cr has been shown to decrease the martensitic transformation temperatures so that the SMA stays in the austenite phase at room temperature. In particular, addition of Cu, the elemental neighbor of Ni on the periodic table, provides great benefit in many applications for narrowing transformation hysteresis and lowering martensitic yield strength [46].

Figure 2.10 shows the phase dependence on the Cu fraction in the NiTi matrix [62]. At the room temperature, the austenitic phase of NiTi retains the B2 cubic structure up to 30% of substitution of Cu for Ni at the eutectic temperature. Cu also has a stabilization effect on the austenite phase, increasing the range of stable B2 austenitic phase from about 920 to 1583 K in NiTi (Figure 2.1) to about 390 to 1300 K in various NiTiCu concentrations [42, 59]. With 10% or more alloyed Cu, the phase transformation starts as B2 to B19 orthorhombic martensite, then progresses to B19 to B19' monoclinic martensite [42, 45]. As more Cu is added, the B19 to B19' transformation temperature is depressed, and thus at high Cu alloying (>15%), the transformation becomes only B2 to B19 above 273 K.

Because of the change in transformation paths, Cu addition also changes the transformation temperatures and hysteresis of transformation in heating and cooling cycles. The effects of Cu alloying are highly desirable in industrial applications for many reasons. The transformation temperature is less sensitive to Ni or Cu composition change in NiTiCu alloys, which simplifies control required for manufacturing. Thermo-hysteresis measured by the DSC curve is narrowed from around 30 K for binary

alloy to less than 15 K for alloy with 5% or more Cu. Lower hysteresis translates to faster shape memory response to change in temperature; especially important in thermo actuator applications. The stress hysteresis is also decreased in the pseudoelastic loading/unloading plateaus. The return pseudoelastic force in NiTiCu is much larger than that of binary NiTi. The energy storage density in pseudoelastic springs is, therefore, correspondingly higher.
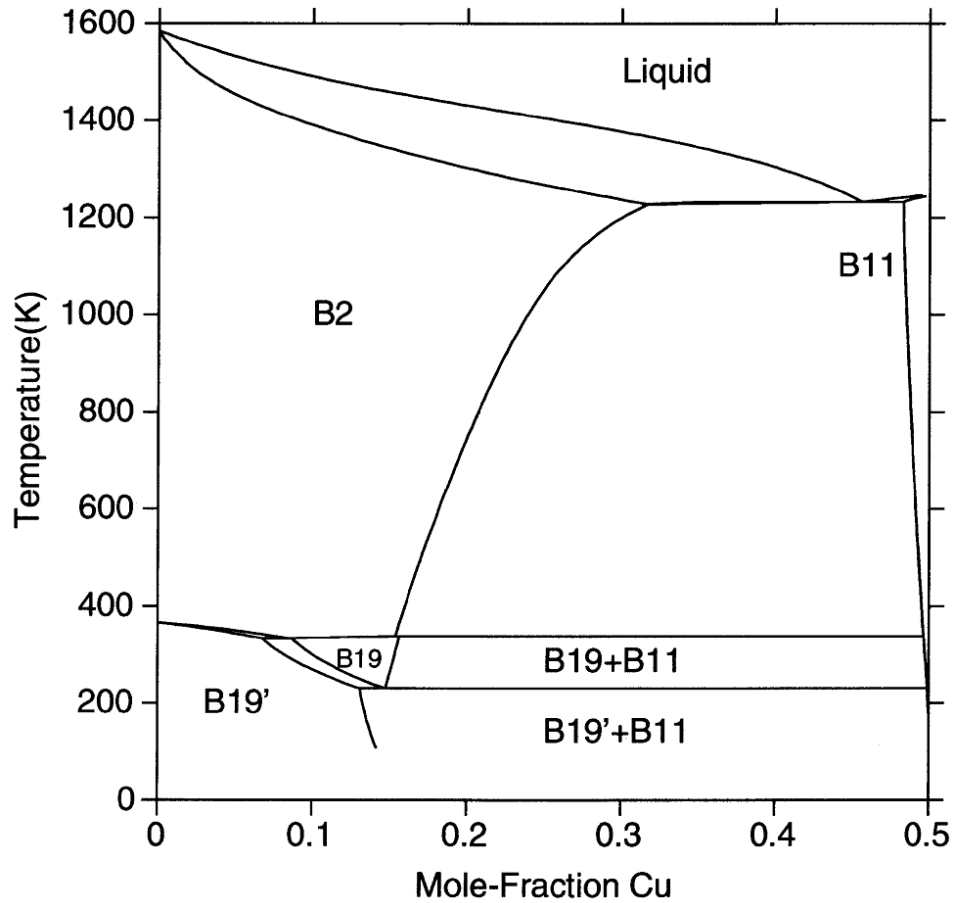


**Figure 2.10** Pseudobinary TiNi-TiCu phase diagram including low-temperature B19 and B19' phases [62].

## 2.3      Corrosion resistance of NiTi SMAs

The pseudoelastic property of NiTi SMA is similar to that of human bone[63], and since its discovery in 1962, these unique effects are extensively applied in various medical applications, including stents, surgical tools, bone implants, and orthodontic arch wires [4]. Apart from the superior mechanical

properties, NiTi is a self-passivating alloy much like titanium alloys (i.e. Ti6Al4V) and stainless steel. The standard $\Delta G$ of formation of $TiO_2$ and NiO are -940 kJ/mol and -212 kJ/mol, respectively [64]. Due to the thermodynamics stability of titanium oxide ($TiO_2$), $TiO_2$ forms preferentially on NiTi surfaces upon exposure to air [65]. Titanium oxide passivation layer enables the metal to have relatively high corrosion resistance and low cytotoxicity. However, like other self-passivating alloys, NiTi is susceptible to pitting corrosion[66], and as well as Ni ion release; a common allergen released from the surface of medical implants [67–69]. Shown in Figure 2.11 is the accelerated corrosion of the present thesis work.
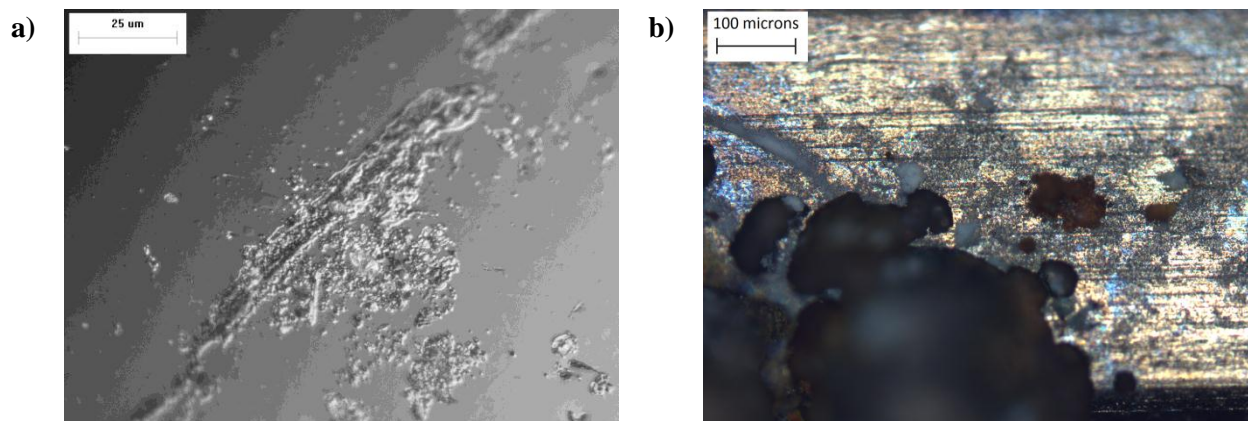


**Figure 2.11**. Experimentally accelerated corrosion inducing a) typical pitting corrosion on a NiTi alloy, b) pitting corrosion on an NiTiCu wire

### 2.3.1    Benchmarks and method of characterization

Key experimental methods for characterization of corrosion resistance include cyclic potentiodynamic polarization, potentiostatic polarization, electrochemical impedance spectroscopic measurements, and long period ion release tests in simulated biological environments. This thesis work only focused on the pitting resistance assessment using cyclic polarization and Ni ion release simulations, for preliminary feasibility investigations. In cyclic polarization tests, the break down potential and passivation current are major indicators of passivity, and high break down potential of 800mV to 1300mV vs SCE can be achieved in NiTi with good surface treatments [63]. For Ni ion release, the mass of Ni ion released per area is used by convention. The safe limit for Ni ion release in medical implants is still an area of research, although a reference amount have been determined for safe drinking water (20 ng/mL of Ni) [70]. Scholars have already established that high level of soluble Ni can cause allergic relations [71] and cytotoxicity *in vivo* [68, 69]. Simulated environments used in different tests often mimic bodily environments of different pH and ion concentrations, such as blood plasma (Hanks' solution), simulated saliva, and phosphate buffered saline [68, 74].

### 2.3.2   Common corrosion resistance improvement techniques

Beside mechanical fatigue, the longevity of medical implants is determined by the corrosion resistance in the human body; a chemically dynamic environment with varying pH and oxidative stressors.  Current research direction on the corrosion resistance of NiTi aims toward the reduction of Ni at the surface and modification of the surface oxide characteristics.  There are several common methods used to achieve corrosion resistance improvements which include: mechanical polishing [74, 75]; chemical etching [2, 68, 76]; heat treatments [65, 68, 74, 77]; $H_2O_2$/water boiling [78–80]; plasma ion implantation [81–83]; and carbon surface coating [82].

One of the most traditional methods, mechanical polishing, reduces surface defects and therefore, actual surface area, by grinding the SMA surface with gradually finer carbide, silica, or alumina sand paper or particle slurry.  Smooth surface also become devoid of crevices and pits in comparison to cast material, which can limit pitting corrosion [68].

Heat treatment relies on the growth of the $TiO_2$ layer and out diffusion of Ni ion from the oxide surface by heat treating at temperatures ranging from $300 \, ^{\circ}C$ to $750 \, ^{\circ}C$ for 15min to 10h in atmosphere of air and argon [65, 77].  The heat treatment thickens and homogenizes the oxide, decreasing the diffusion paths of the Ni ion in the base metal to the exterior surface.  During manufacturing of NiTi devices, the surface oxide heat treatment is often done *in situ* to the essential heat treatment that induces special mechanical properties of PE and SME.

Aging in boiling water removes Ni in the oxide like furnace heat treatments, though Ni ions are removed through diffusion and dissolution rather than by increasing oxide thickness.  Reported methods are direct immersion, steaming [80], and autoclaving [65, 84].  Water boiling has been shown to deplete the surface oxide layer of Ni with 30 min immersion, but Ni concentration increases after further boiling [84].  Shabalovskaya et al. observed a depletion of Ni not only in the oxide, but also the innermost surface by up to 5~10% [85].  The nickel depleted surface has thus been shown to have great biological performance similar to that of pure titanium [85, 86].

Chemical etching of NiTi often employs a combination of concentrated HF and $HNO_3$ mixture, and this surface modification method relies on preferential removal of oxide and Ni and then thermodynamically preferential regrowth of $TiO_2$ [63, 70].  The exact mechanism behind the reduction of Ni in chemical etching is often attributed to difference in rate of Ti and Ni oxide formation [2, 63]; however, the exact mechanism is not well understood due to rapid speed of oxide formation.

## 2.4      Traditional fabrication and processing of NiTi alloys

Fabrication of NiTi requires precise manufacturing processes which often includes the following steps: ingot melting; hot working; cold working; and aging heat treatments [87]. Ingot composition and purity are extremely important so vacuum induction melting is often done to ensure tight composition and impurity control. The hot working process shapes the general form of the ingot through forging, extrusion, and/or rolling techniques at temperatures of 600-800°C. The combination of cold working and subsequent heat treatments are two established methods to achieve the desired phase transformation behaviour for specific applications.

As previously mentioned in section 2.2.3, specific lattice and microstructural conditions are required for SME. Cold working creates random dislocations, detwinning, and permanent deformation of the twinned martensite structure. These dislocations impede the mobility of the slip planes, decreasing the slip stress [88–90]. Approximately 25% cold work is required to raise $\sigma_s$ above the $\sigma_m$ to enable B2 $\rightarrow$ B19' SIM transformation and PE [53]. Lastly, aging treatments are required for relaxation of lattice strain and reorganization of permanent deformation created by cold-working [31, 39, 90]. Typical heat treatment temperatures range between 450 to 800°C. Besides lattice relaxation, according to the phase diagram in Ti-rich NiTi alloys the $Ti_2Ni$ IMC can precipitate and for Ni-rich alloys $Ti_3Ni_4$, $Ti_2Ni_3$, and $TiNi_3$ can be precipitated. The Ni and Ti content of the larger NiTi grains (i.e. matrix) are depleted through precipitation and subsequently the transformation temperatures are altered [16, 51, 91]. Since the $A_f$ and $\sigma_m$ follows the Clausius-Claperion relation, an increase in $A_f$ from Ni depletion will lead to a decrease in $\sigma_m$ and, thus, lower pseudoelastic forces [58]. R-phase transformation path can also result from aging treatments [92]; however, the R-phase transformation will not be covered in this thesis as it is outside of the scope of this work.

## 2.5      Laser processing of SMAs

Due to the sensitive relation of composition, microstructure, and mechanical properties of SMAs, lasers are one of the most common sources of energy for welding and cutting of these alloys due to high cooling rates and extremely localized heat input [21]. Recently, considerable research interest has been placed in the performance improvement of SMA with laser processing on its biocompatibility [93] and shape memory characteristics. Specifically, efforts have been focused on creating local compositional or microstructural variance in a single SMA device. Such a device would have increased functionality resulting from programmable actuations, multiple shape settings, and locally improved biocompatibility.

This thesis focuses specifically on the Multiple Memory Material technology (MMM), developed by Khan et al. [27, 28]. The MMM technology has shown great versatility in creating multiple memory

micro-gripper [30] and multiple memory linear actuator [29]. The basic principles of microstructural and compositional augmentation are achieved through application of high density energy, for example via a laser, causing full or partial melting of the base metal. At the same time, vapourization also occurs leading to local loss of elemental constituents [28]. It has been shown that preferential vapourization of Ni occurs relative to Ti due to a lower equilibrium vapour pressure of Ni than that of Ti as illustrated in Figure 2.12 [28].
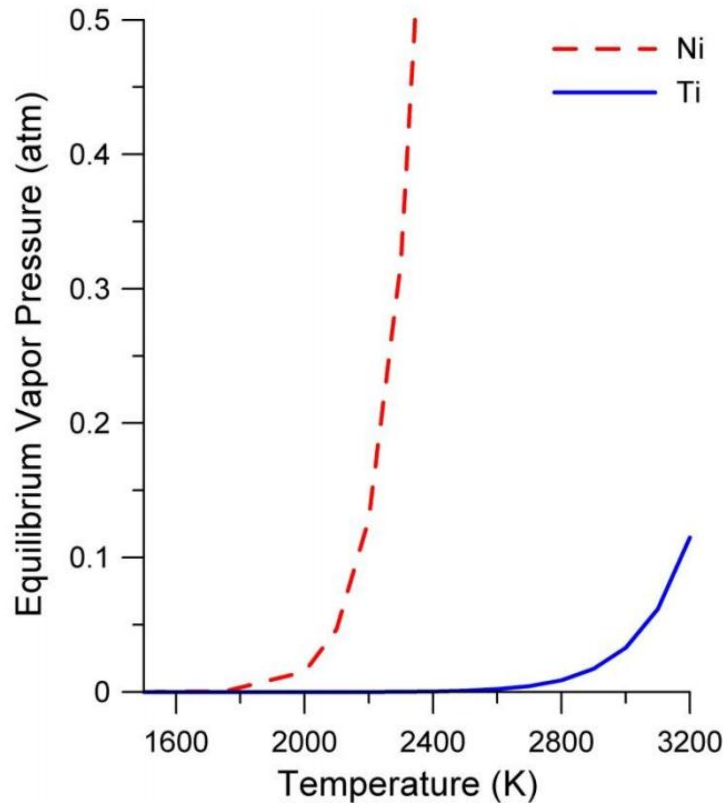


**Figure 2.12** Calculated vapour pressures of Nickel and Titanium over an equiatomic NiTi mixture. Ni has significantly higher vapour pressure at the same temperature, creating a larger vapourization flux. Taken from [28]

Laser pulsing was shown to cumulatively remove Ni from the alloy, and thus, change the local composition from Ni-rich to eventually Ti-rich as desired [28]. As a result, the laser process zones (LPZs) have correspondingly higher phase transformation temperatures with increasing Ti composition shown in Figure 2.13 [28]. These findings correlate well with the Ni-dependence of transformation temperature reported by Frenzel et al. [51]. Through localized and controllable change in the NiTi

19

composition, multiple memories can be embedded and programmed in a single monolithic piece of SMA. With the large change in composition and microstructure, it is expected that the laser process alters not only the functional properties but the mechanical properties and biocompatibility as well.
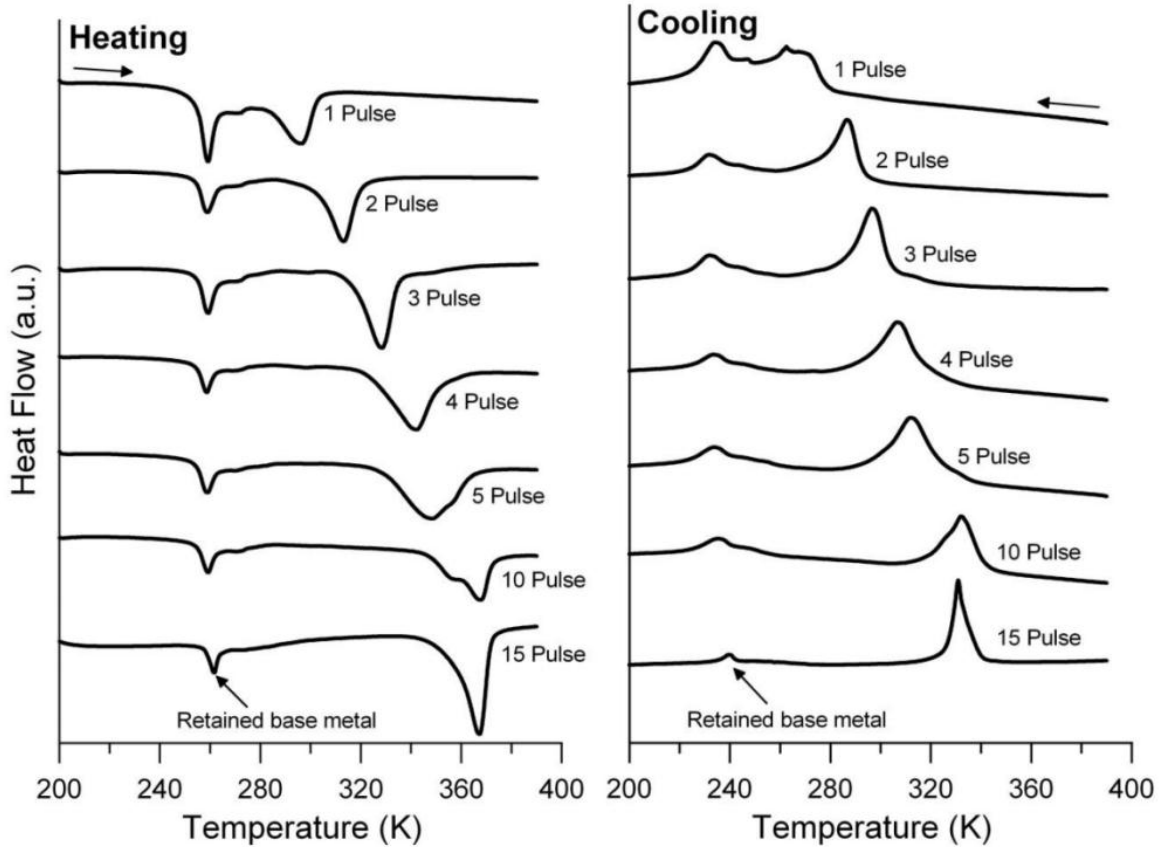


**Figure 2.13** Differential scanning calorimetry analysis of laser pulse processing of Ti-50.7 at%. 5Ni alloy wire. A second set of phase transformation peaks is identified at higher temperatures in both the heating (B2→B19') and cooling (B19'→B2) curves. The second set of peaks (i.e. at higher temperature) is from the laser processed sections [28].

### 2.5.1 Effects of laser processing on mechanical properties

The laser melting process is similar to laser welding and both, therefore, have a significant effect on the yield strength, working strain, and fatigue limit as shown in the literature [18, 31, 94–96]. The removal of cold work causes distinct softening of the weld zone shown in Figure 2.14 [21]; an effect reported separately by Tam et al.[21] and Chan et al. [20]. The rapid melting and solidification process returns the metal back into its solutionized state in which lattice is no longer work-hardened or strengthened through precipitation hardening. The weld zone or laser processed zone then becomes the

20

location of stress concentration and yield. As a result, past studies have found a decrease in ultimate tensile strength and elongation in welded metal in Ni-rich NiTi after pulse Nd:YAG butt welding [18, 27].
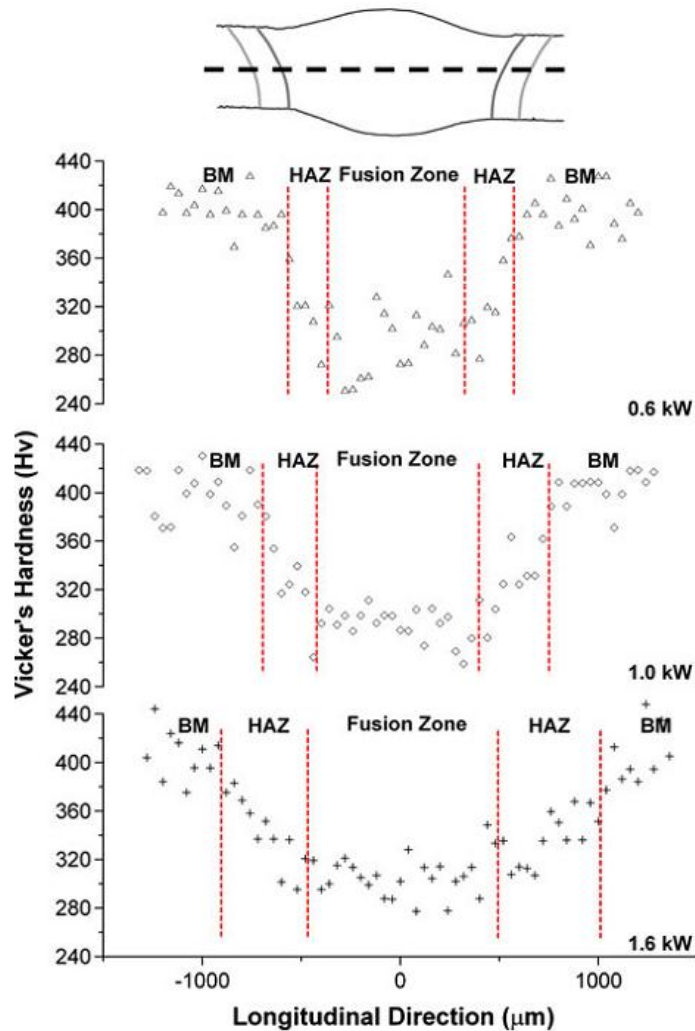


**Figure 2.14** Vickers hardness across the fusion zone of welds at increasing laser power. The hardness profile decreases steadily from the heat affected zone (HAZ) to the center of the fusion zone. The hardness at each zone is relatively independent of increasing laser power. [21]

### 2.5.1 Current observation of MMM processing on pseudoelastic behaviour

The unique technology has already been shown to be able to control shape memory characteristics through controlling vapourization of Ni. However, the alteration in PE has only been superficially discussed in the thesis of M. Daly [97]. In the work of M. Daly [97], the processed wire was an aged NiTi wire with pseudoelastic forward and reverse loading plateau of 730 and 400 MPa at 60°C. The wire was pulsed with Nd:YAG laser at energy above the Ni vapourization threshold with equal length of base metal zone and laser processed zone alternating throughout the wire. The tensile response of the

resultant wire is provided in Figure 2.15 [97] and showed two pseudoelastic plateaus roughly 100 MPa apart. Processed NiTi wire showed a higher austenite finish temperature, which indicates the austenite phase is less stable. Thus a lower stress was required to induce formation of SIM compared to the base metal at the same temperature. After 20 tensile cycles, the two stage pseudoelastic wire was stabilized with around 2.4% elongation. The multiple pseudoelastic plateaus are not from two distinct sections of the wires but from a mixture of alternating processed and base metal zones. This particular configuration is not a truly distinct augmentation of the pseudoelastic forces and has limited usage in applications. Nevertheless, it is expected that following clues from this methods, true augmentation can be achieved through different laser processing protocols which prompted the investigation in this work.
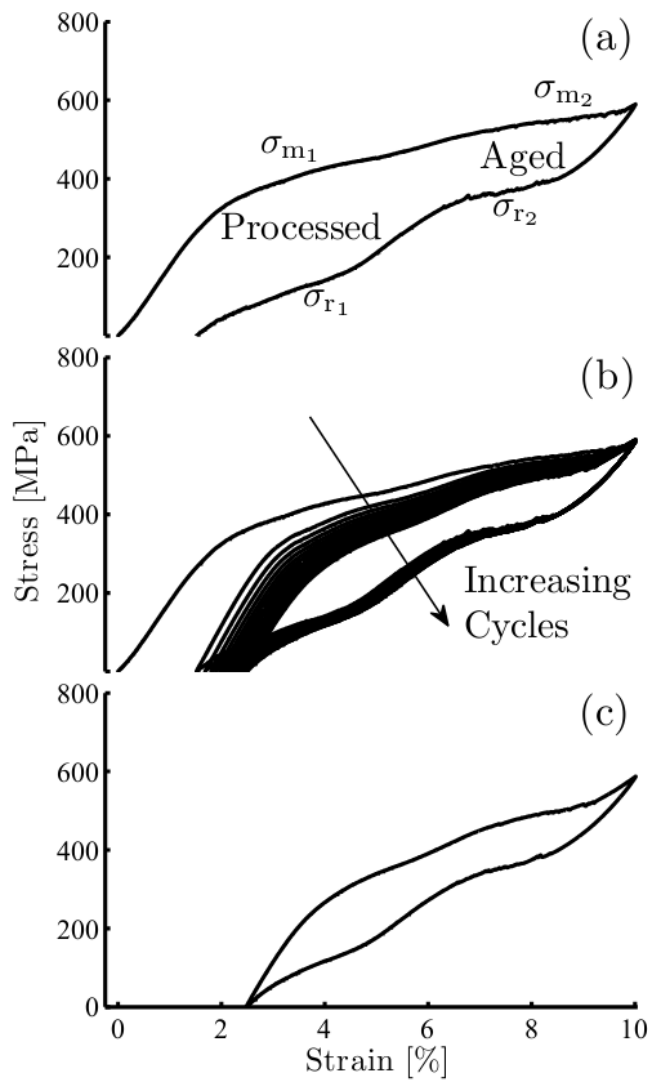


**Figure 2.15** Pseudoelastic response of laser processed NiTi SMA wire demonstrating (a) combined tensile behaviour of laser processed and base metal regions, (b) reduced strain recovery after cycling, and (c) perfect PE (strain recovery) after 20 cycles. [97]

### 2.5.1 Current state SMA engineering for medical applications

The biocompatibility and ability to mimic biological force of NiTi based SMAs makes them ideal for medical applications [5, 105]. Since the 1970-80s, SMA have been pioneered in orthodontic arch wires for moving teeth by G. Andreasen [10] and arterial stents for expanding clogged blood vessels by C. Dotter [6]. Medical devices like catheter guide wires and orthodontic archwires take advantage of the pseudoelastic property [10, 106]. Gastrointestinal and vascular stents, in comparison, take advantage of SME for installation and PE for constant force and ability to withstand a high degree of strain during service [5, 23].

Due to the traditional manufacture process, the pseudoelastic force is constant throughout the whole monolithic component, which greatly limits the functionality of conventional SMA materials. For the sake of further customization of medical devices, researchers have since attempted to improve the functionality of these NiTi devices achieving multiple functional properties throughout a SMA device. Some of these techniques include powder metallurgy, direct electric resistance heat treatment (DERHT), cross sectional deformation, and joining of multiple alloys. Controlling NiTi composition through powder metallurgy has been successful in tailoring the shape, phase transformation temperatures, and porosity density [100–102] but has yet to demonstrate high strain PE [103]. Since the invention in 1988 by Miura et al., DERHT process, shown in Figure 2.16(a), has been investigated by multiple researchers to modify local mechanical properties by applying local annealing through resistive heating on NiTi and NiTiCu arch wires [11, 13, 104]. Another promising method, cross sectional deformation of hollow NiTi wires, shown in Figure 2.16(b), has also been shown to modify the anisotropic pseudoelastic bending force [14]. More recently, an attempt to address this problem has been made by Sevilla et al. [12] by creating multiple pseudoelastic regions in a single orthodontic wire through dissimilar joining of NiTi and NiTiCu. Specifically, Sevilla et al. reported two distinct pseudoelastic plateau in one stress-strain cycle of a welded archwire.

However, there are limitations in local annealing, cross sectional deformation, and laser welding segments of wires. First, the critical length of the different pseudoelastic segments will be limited by the length of the heated region, deformation tool, and welded wires. The precision in altered pseudoelastic force of each method is largely limited by the required annealing protocol, degree of deformation, and availability of SMA materials with specific compositions. Dissimilar welding of SMA wires also reports problems, such as deformation of the original wire form factor, intermetallic formation, and solidification cracking [19–21]. These previously proposed techniques also do not allow for large resolution between pseudoelastic stresses and can be extremely time consuming. A finer increment of control is needed in the pseudoelastic customization of SMAs. It was, therefore, proposed that, with the development of the

MMM laser processing, the augmentation of pseudoelastic stress with great degree of control and accuracy could be possible; meeting the demands of medical device applications such as the orthodontic arch wire and stent.
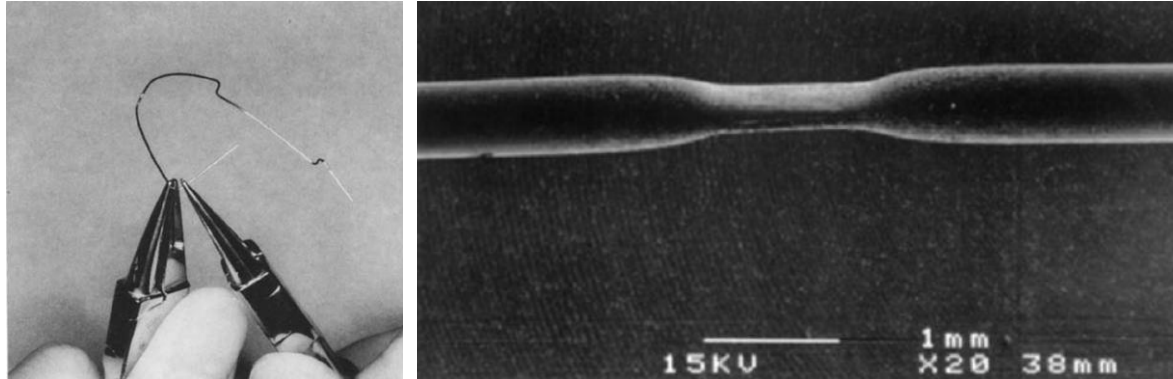


Figure 2.16 (a) direct electric resistance heat treatment (DERHT) process for orthodontic archwire [11] (b) SEM image of cross sectional deformation of hollow NiTi wires for bending and pseudoelasticity augmentation [14]

### 2.5.2 Effects of laser processing on corrosion properties

Laser processing such as the MMM technology can drastically change the surface conditions of the NiTi and apart from changes in mechanical properties and functional properties, biocompatibility and corrosion properties have also been altered. The corrosion resistance of NiTi has been studied carefully and as a result, the alloy is recognized as a biocompatible material suitable for medical applications [105]. Nevertheless, there are many conflicting studies on the effects of laser welding and laser processing, showing both improvements [31, 93, 106] and degradation [32, 33] of corrosion resistance following laser processing. Improvement from laser processing has been attributed to surface defect removal (smoothing) [106], removal of carbon impurities through vapourization [31], and lowering Ni surface concentration [93]. However, the exact mechanism has not been proposed in these studies. On the other hand, Chen et al. in 2012 showed that welded NiTi wires have poor corrosion properties with increased conductivity of the surface and higher oxide breakdown potentials, shown in Figure 2.17 [33]. Comparing the break down potential of "Base NoHT" (~350mV) and "Weld NoHT" (~250mV), the welded NiTi is significantly lower in breakdown potential than base material. Heat treatment is required to restore the corrosion property to that of the original state [33]. As Shabalovskaya et al. suggested in a comprehensive review [2], the variance in corrosion performance in NiTi research can be traced to differentiation in experimental setup, region of specimen tested (isolated laser processed zone or mix of base and processed metals), polishing techniques prior to test, quality of base metal (as determined by impurity concentration), and processing parameters. Since specific laser processing protocols yield

24

different results, a set of corrosion performance assessment must be made in order to confirm the exact effect of MMM technology on the corrosion behaviour.
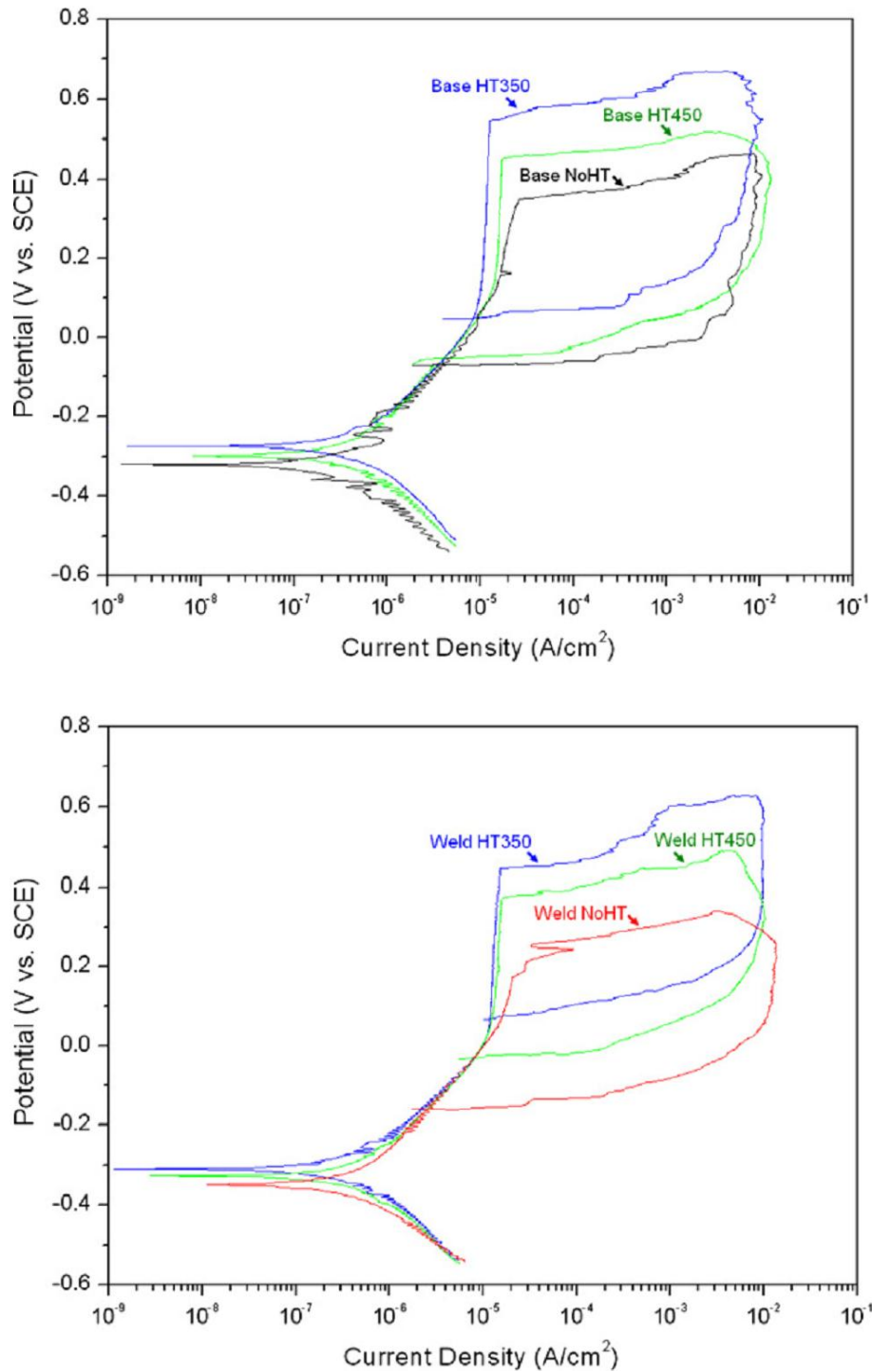


**Figure 2.17** Cyclic polarization plots of (a) base metal NiTi and (b) welded NiTi with heat treatment at 350°C and 450°C in Hank's solution at 37.5 °C at scan rate of 0.5mV/s. The welded NiTi has higher overall corrosion current and higher breakdown potentials. [33]

25

# Chapter 3

## 3. MMM processing for pseudoelasticity augmentation of NiTiCu SMA

The present work attempts to address the current shortcomings of PE augmentation presented in section 2.5.1. Current techniques often encounter a limitation on maximum augmentation zone when physically modifying the SMA, due to size limitation on either heat source in DERHT [11], weld configuration in dissimilar joining [12], or minimum bending angle of hollow wires [14]. With the recent success of the MMM technology in the augmentation of NiTi SME, similar laser processing principles could be applied to achieve fine adjustment of local microstructural properties and thus precise pseudoelastic augmentation.

Building on the work by Khan et al. [19, 26, 28], the first portion of this chapter shall demonstrate the physical effect of combining MMM processing using a high precision fibre laser on medical grade SMA material. The penetration profile of fibre laser is of high aspect ratio, compatible absorption wavelength for most metals, and most importantly, capable of sub 100 μm spot diameter. These were all considered advantages compared to the Nd:YAG laser source. The fibre laser also allows for flexibility in position of the laser beams and welding applications [107]. In the case of this study, the fibre laser was able to grant greater control over the laser processed zone area compared to traditional MMM processing done with an Nd:YAG laser.

The second half of the chapter demonstrates the ability of the laser processing protocol for augmentation of pseudoelastic property. Correlations are drawn between laser processing parameters, microstructural changes and performance of the SMA. To better understand the underlying mechanism and expedite application in future generation medical devices, a phenomenological model was derived from the relation laser processing protocol, laser processed zone dimensions, and augmented pseudoelastic force plateaus.

## 3.1 Experimental

### 3.1.1 Materials

Medical grade NiTiCu wires, supplied by SmarterAlloys Incorporated (Toronto, Canada), were used for the entire set of experiments. The as-received NiTiCu base metal wires (referred as BM) were of 50.7 at.% Ti, 44.5 at% Ni, and 4.8 at.% Cu in composition and 0.018 by 0.025 inch (635 x 465 μm) rectangular cross-section. The as-received material has been thermomechanically processed by the manufacturer to possess pseudoelastic properties at room temperature for use in medical device

applications. The wire material was cleaned with ethanol and deionized water prior to laser processing in order to remove surface contaminants.

### 3.1.2 Laser processing and LPZ geometry

For all the mechanical and analytical experiments, laser processing of the as-received wire was conducted with IPG model YLR 500 MM Ytterbium diode pumped laser source equipped with a nominal post-optical spot size of 50 µm. In this study, the samples were laser pulsed in a Miyachi Unitek MX2000 glove box in an argon atmosphere for complete oxygen shielding during the laser process. The wire was secured in a groove on a stainless steel fixture to facilitate uniform heat distribution and prevent movement during processing as illustrated in Figure 3.1. All laser pulses used in this study were 10 µs square pulses fired at 1 Hz frequency between pulses with no overlap. To demonstrate the precise control of the pseudoelastic properties, the experimental samples were processed with single laser pulses ranging from 30, 40, 50, 60, 70, 80, and 90% of the maximum peak power (i.e. 500 W). These parameters were chosen to ensure only partial processing of the wire occurred. Each spot was directly adjacent to the previous spot (i.e. 0% overlap), as shown in optical micrograph in Figure 3.2.

Through ImageJ v1.46r (open source image analysis program by National Institute of Health, USA), the cross section area and volume of the processed samples were measured and integrated from dimensions of the laser processed zone (LPZ) using the approximation of cylindrical trapezoid illustrated in Figure 3.1. The LPZ diameter, tip width, and penetration depth corresponds to the top width, $D_1$, bottom width, $D_2$, and height, $h$, of the trapezoidal cone. $D_2$ was taken as the intercept of the lowest point of LPZ and the two inclines of the trapezoid. Nine cross sections of LPZ were made for each laser power parameter (30 to 90%) for this volume calculation. The results of the measurements are presented in Table 1.

**Table 1**. Dimensions of laser processed zones for various parameters

| Parameter (% of peak power) | Top width, $D_1$ (µm) | Penetration, $h$ (µm) | tip width, $D_2$ (µm) | aspect ratio, $h/D_1$ |
|:---:|:---:|:---:|:---:|:---:|
| 30 | 251 | 65 | 92 | 0.258 |
| 40 | 292 | 115 | 94 | 0.395 |
| 50 | 368 | 207 | 74 | 0.563 |
| 60 | 425 | 308 | 76 | 0.723 |
| 70 | 457 | 376 | 95 | 0.824 |
| 80 | 466 | 434 | 141 | 0.930 |
| 90 | 471 | 463 | 178 | 0.983 |
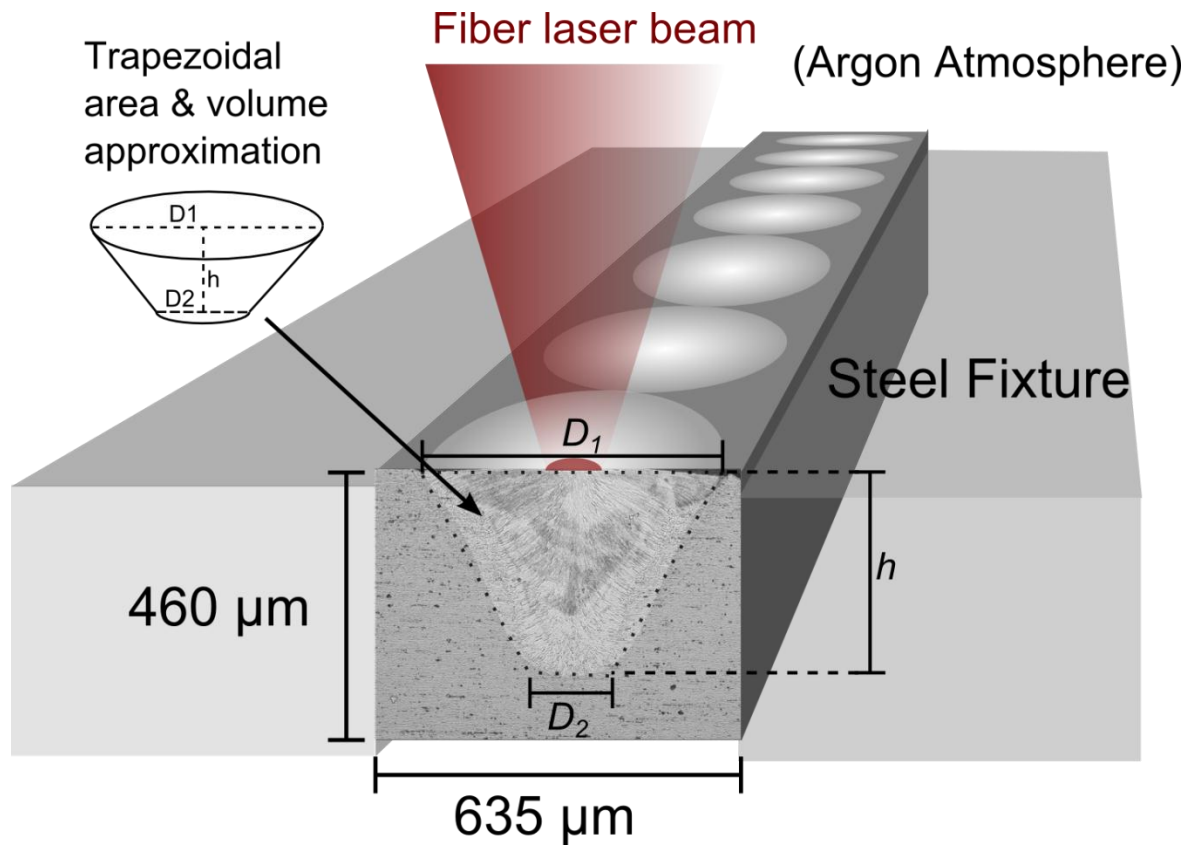
**Figure 3.1** Schematic showing laser process configuration, dimensions of NiTiCu wire, and approximation method of laser processed zone (LPZ) dimensions
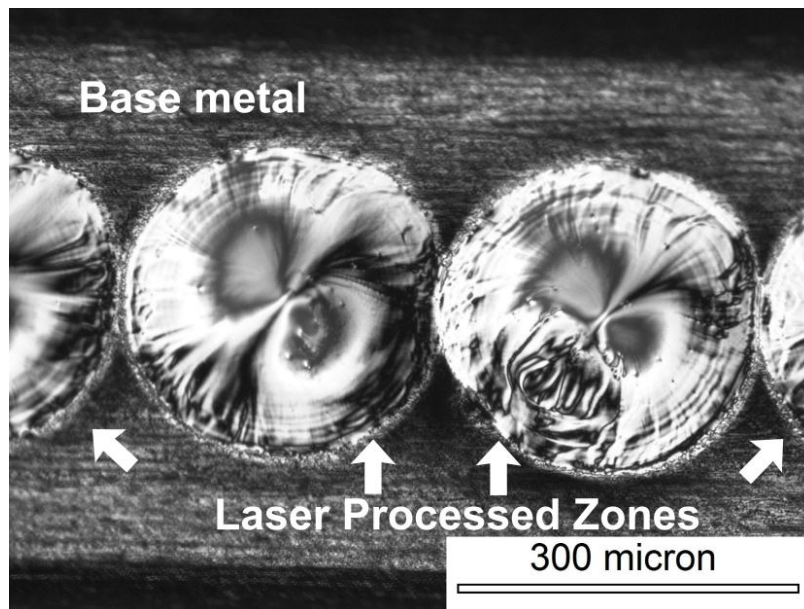


**Figure 3.2** Top view optical image of the LPZ

### 3.1.3 Composition and phase analysis

Wire cross-sections were used to investigate the microstructure, composition, and estimate the volume of the processed regions. The microstructural analysis was performed using an Olympus BX51M Metallurgical Optical Microscope equipped with a differential interference contrast polarizer. Compositional analysis was conducted using a Jeol JSM-6460 scanning electron microscope (SEM) equipped with an INCA energy system 350 EDX microanalysis system. X-ray diffraction (XRD) was used to determine and compare the phase change and homogeneity of the NiTiCu BM and processed specimens. A D8 Focus XRD (Bruker AXS Inc.) was used for this analysis. The X-ray wavelength, $\lambda$, is Cu-k-$\alpha$ wavelength (1.54Å). The samples were mounted on a flat surface and placed on a rotational stage (0.5 rev/sec) during analysis to minimalize the directionality effect.

Cold worked, solutionized, and laser processed SMAs have well known differences in phase transformation characteristics. Many studies have confirmed that the fusion zone of laser welded SMA has property similar to that of solutionized material [16–18, 21]. Thus solutionized BM was used alongside as-received BM in this study for comparison. Solutionizing treatment was done through annealing as received BM at 800°C for 1 hour in vacuum and then immediately quenching. A Thermal Analysis Q2000 differential scanning calorimeter (DSC) manufactured by TA instruments was used to determine the thermal behaviour of as-received material, solutionized material, and laser processed specimens; following a modified ASTM F2004-05 testing standard. The scanning temperature ranged from -40 to 120°C at a rate of 5°C/min for heating and cooling cycles. The austenite and martensite start and finish transformation temperatures were determined using the method described in section 2.2.1 with assistance of Universal Thermal Analysis 2000 v4.5 from TA instruments.

### 3.1.4 Mechanical properties

To assess the effect of laser processing on the pseudoelastic response of the NiTiCu material, tensile tests and three point bending tests were performed on the base metal and the processed samples following the methods described in the ISO15841 standard [108]. Mechanical tests were conducted on an Instron 5548 microtensile tester manufactured by Instron Corporation, Norwood, MA which was retrofitted with a temperature chamber set at 35°C, the specified operating temperature of the metal, for all tests. To determine the pseudoelastic plateau stress, the tensile coupons were cycled twice up to 8% strain at crosshead speed of 0.8mm/min. Test gauge length was set to 2 cm for all the tensile experiments. For processed wires, the entire gauge length was processed as described in section 3.1.2. The forward and return pseudoelastic plateaus stress then were determined from the 4% strain mark of the second cycle. For three-point bend test, the crosshead rate was set to 7.0 mm/min. The specimens were 35 mm in length and rested between supports which were spaced 10 mm apart and loaded using a 0.1 mm diameter

indenter and fulcrum. Vickers hardness line profile of the LPZ was measured using a Shimadzu Bench type micro-hardness tester using 50 gf with a 20s dwell time and 30 μm spacing between spots at minimum.

## 3.2　　　Effects on microstructure and phase transformation

### 3.2.1　Effects of laser processing on LPZ dimension and microstructure

The volume and shape of the LPZ are dependent on the power input and energy density of the laser beam as well as the surface absorptivity and thermal conductivity of the material. To simulate industrial manufacturing processes, this current study limits the process variable to only the input power density, keeping constant pulse time of 10 μs and pulse frequency of 1 Hz. The LPZ dimension measurements are obtained as described in section 3.1.3 and listed in Table 1.　Figure 3.3(a-c) are the typical cross-sectional profiles of the NiTiCu wires processed from 30 to 90% of laser peak power (i.e. 100% = 520 W). There was a clear trend showing the aspect ratio (h/D1) increased linearly with laser power. At the same time, the dimension of the LPZ changed from a shallow half-ellipsoid to a deep penetrating trapezoidal cone.

Figure 3.3 (a) shows a representative image of LPZ produced at a relatively low energy density at 40% power. The LPZ solidification structure was a well-established characteristic of conduction mode welding, in which it was shallow and wide [62, 109].  As the energy input was below the critical value for vapourization, only a small area around the point heat source was heated above the melting point in conduction mode. At 50% power the laser interaction mode progresses from conduction mode toward keyhole mode shown by increase in penetration depth and hence aspect h/D1 in Figure 3.3 (b). The LPZ structure then became that of a keyhole mode above 50% power as shown in Figure 3.3 (c), and continuously increased in keyhole penetration at higher laser power  [62, 109]. It should be noted that porosity was observed occasionally in middle of the LPZ at high power. The author suspected the porosity was a result of vapour trapped in the weld pool from the extremely short pulse durations and rapid solidification and, hence, termination of the keyhole. Similar vapour entrapment has been observed in fibre laser beam welding of stainless steel [110] and pulse Nd:YAG laser welding of Ti alloy [109]. This porosity condition could, therefore, be avoided by using longer pulses or by using lower peak powers and processing both sides of the material to increase process material volume in a different fashion.
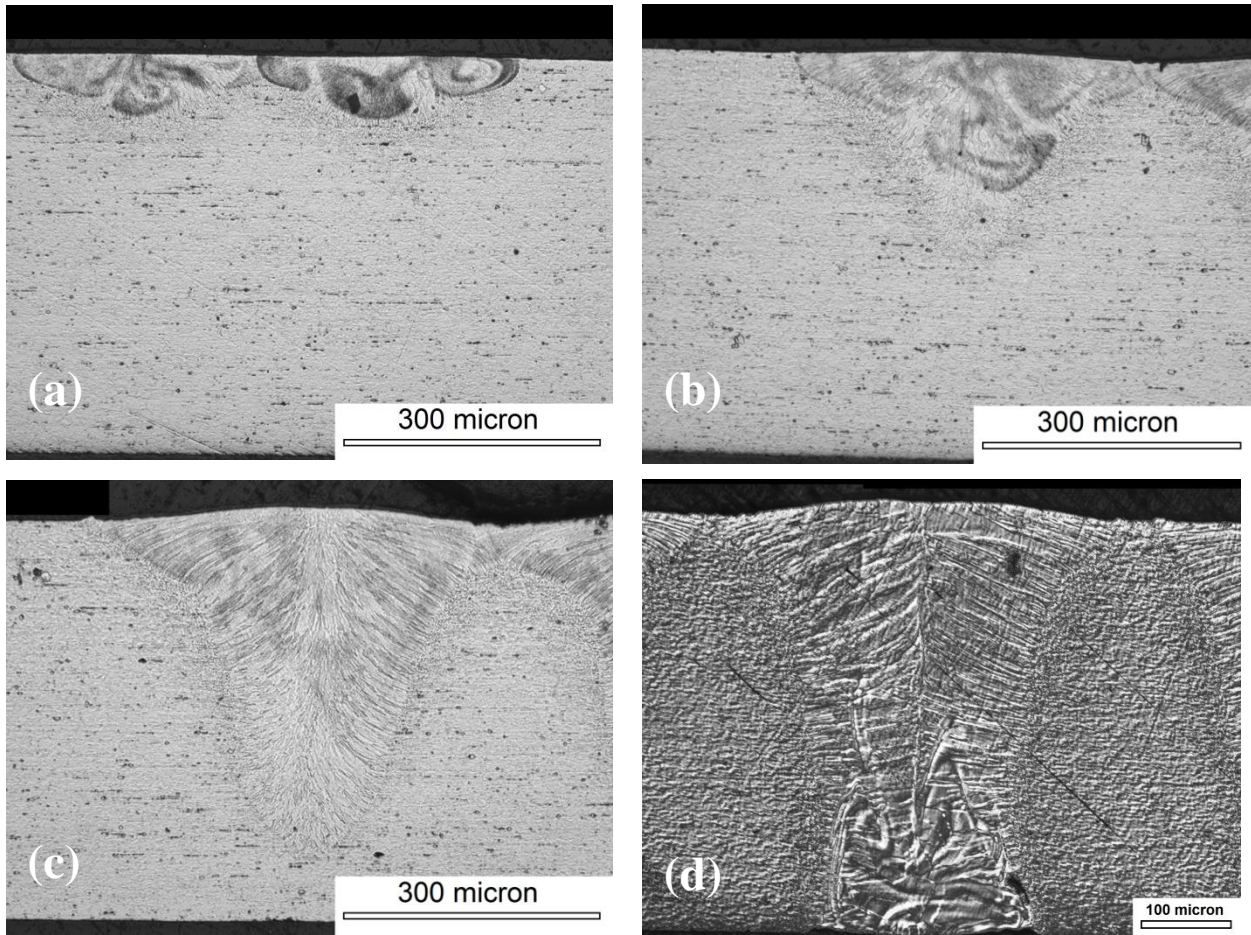
**Figure 3.3** Cross sectional view LPZ created by (a) 40%, (b) 60%, (c) 80%, and (d) 90% peak power (520W). (d) also shows full penetration of the wire

A representative close up micrograph is shown in Figure 3.4 (a) of the boundary of the LPZ, heat affected zone (HAZ), and the BM. The border can be easily identified by the cold-drawn elongated grain of the base metal, the equiaxed grain structure of the HAZ, and the dendritic grains of the LPZ. Grain recrystallization occurred in the HAZ and no significant coarsening was observed. Due to a small area of laser pulse and high undercooling at the interface of BM and molten pool, it was suspected that a high rate of solidification caused the HAZ to be relatively small, ranging from 16 to 30 μm in width. The LPZ grains can be observed solidifying epitxially from the parent grain at the HAZ-LPZ interface in the SEM image Figure 3.4(b).

Energy-dispersive X-ray (EDX) spectroscopy line scan across the LPZ revealed a change in composition caused by vapourization. Figure 3.5 provides the change in elemental constituents in the LPZ of low power (40%) and high power (90%) parameters. Table 2 provides the average composition of the

samples in comparison to that of the BM. On average, no change in Ni and Ti were observed in the LPZ at low power, with the exception of slight decrease in Cu. At high power, there was little change in the overall composition. Slight chemistry change was suspected to be selective vapourization of elemental constituents having low vapour pressure, namely Ni and Cu. This result was similar to the selective vapourization of NiTi through Nd:YAG laser, as reported by Khan et al. [28]. Also observed by Khan et al., at high laser power, more energy is available to induce molten material flow via Maragoni mixing and homogenization of the LPZ. Thus high energy parameter presented less compositional variation.
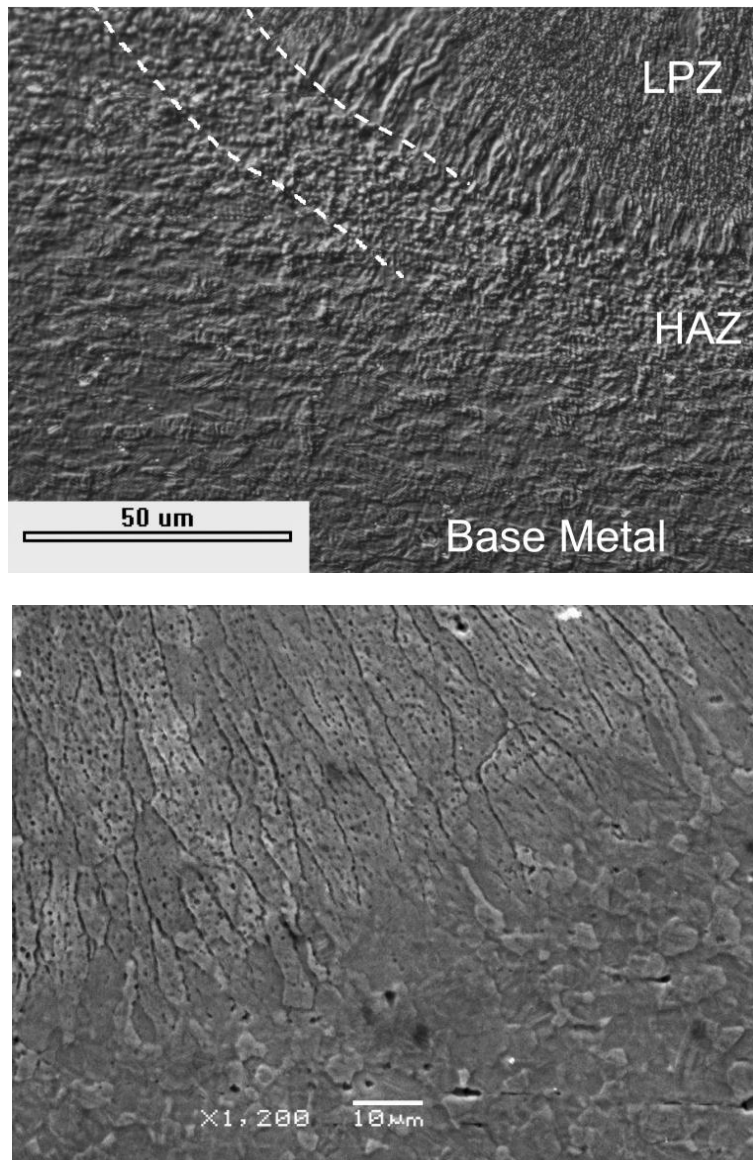


**Figure 3.4** (a) Close up optical micrograph of base metal, HAZ, and LPZ boundary. (b) Scanning electron microscopy showing columnar dendritic solidification of the LPZ stemming from the recrystallized HAZ grains.

**Table 2.** Average composition of laser processed samples compared to that of base metal from EDX analysis

|  | Ti (at %) | Std. dev. | Ni (at %) | Std. dev. | Cu (at %) | Std. dev. |
|---|---|---|---|---|---|---|
| **BM** | **50.8** | **0.42** | **44.5** | **0.42** | **4.7** | **0.37** |
| **40% power** | 51.8 | 0.99 | 44.3 | 1.14 | 3.9 | 0.81 |
| **90% power** | 50.6 | 0.79 | 44.6 | 0.88 | 4.8 | 0.51 |
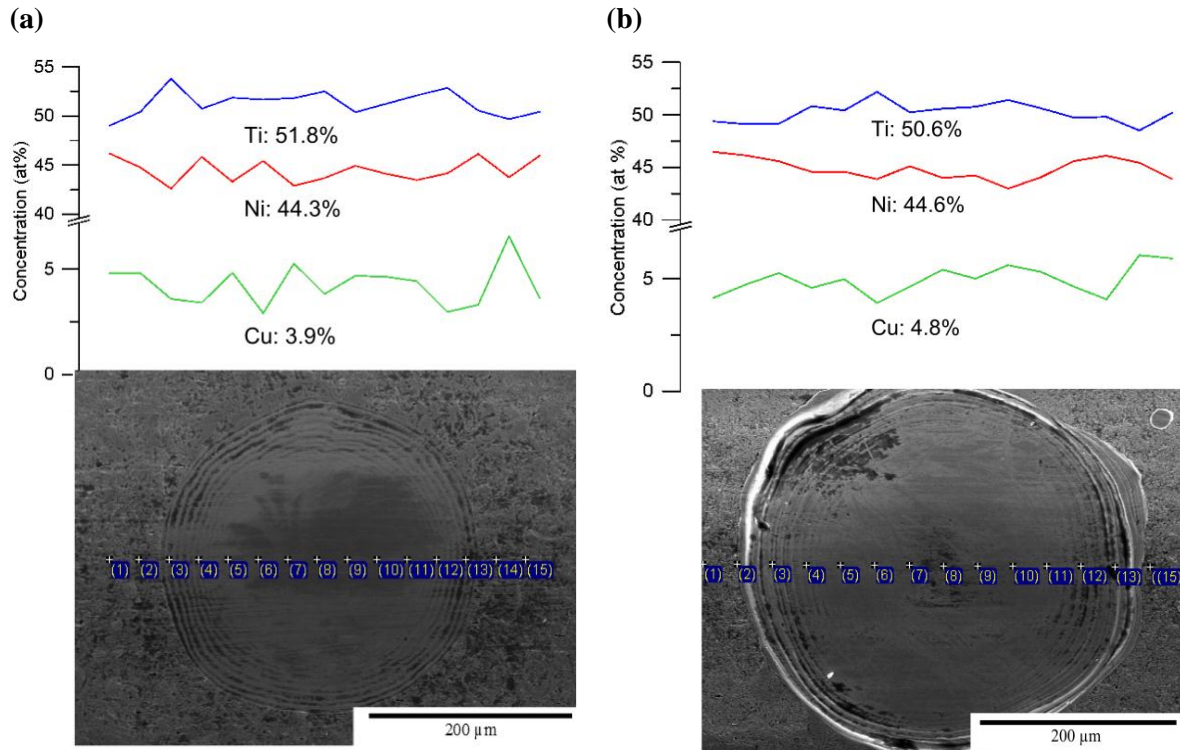


**Figure 3.5** Compositional line scan and average concentrations of alloying elements in the laser processed zone (LPZ) of NiTiCu wire. (a) Energy-dispersive X-ray spectroscopy(EDX) line scans across LPZ of 40% power parameter. A small reduction of Cu was measured in the LPZ. (b) EDX line scan across LPZ of 90% power parameter with no change in all constituents.

### 3.2.2 Changes in phases and transformation temperature of LPZ

Phase transformation properties of NiTi alloys can be affected by alloy chemistry, precipitates and dislocations induced by thermomechanical processing. Phase transformation information is essential in that it can be used to predict shape memory and pseudoelastic behaviour of the SMA at various temperatures. The LPZ solidification structure was suspected to be homogenized, solutionized and, softened from the laser processing, and in this section, these assumptions are confirmed through XRD, DSC analysis, and hardness measurement.

Figure 3.6 shows a XRD spectrum of (a) LPZ and (b) BM. The BM had a phase composition of primarily B2 cubic austenite phase with some partially transformed B19 orthorhombic martensite phase. The mix composition and broader B2(110) peaks in BM were likely due to a more refined and diverse microstructure from cold-work and aging treatment of the manufacturer, shown in earlier micrographs. On the other hand, laser processed NiTiCu introduced no new peaks, indicating no observable change in phase of the LPZ material. The structure in the LPZ was expected to mimic a solutionizing treatment through annealing due to laser processing inducing temperature that surpassed the melting point and subsequently quenching and removing any cold work history. The stability of the B2 phase was due to the large solidification range of B2 phase in the $Ni_{45}Ti_{50}Cu_5$ system; 380 to 1450K according to pseudo-binary TiNi-Cu phase diagram by Tang et al. in 2000 provided in Figure 2.10 [62]. The XRD result also confirmed that composition change, observed in EDX data, and did not affect the local phase composition at room temperature.
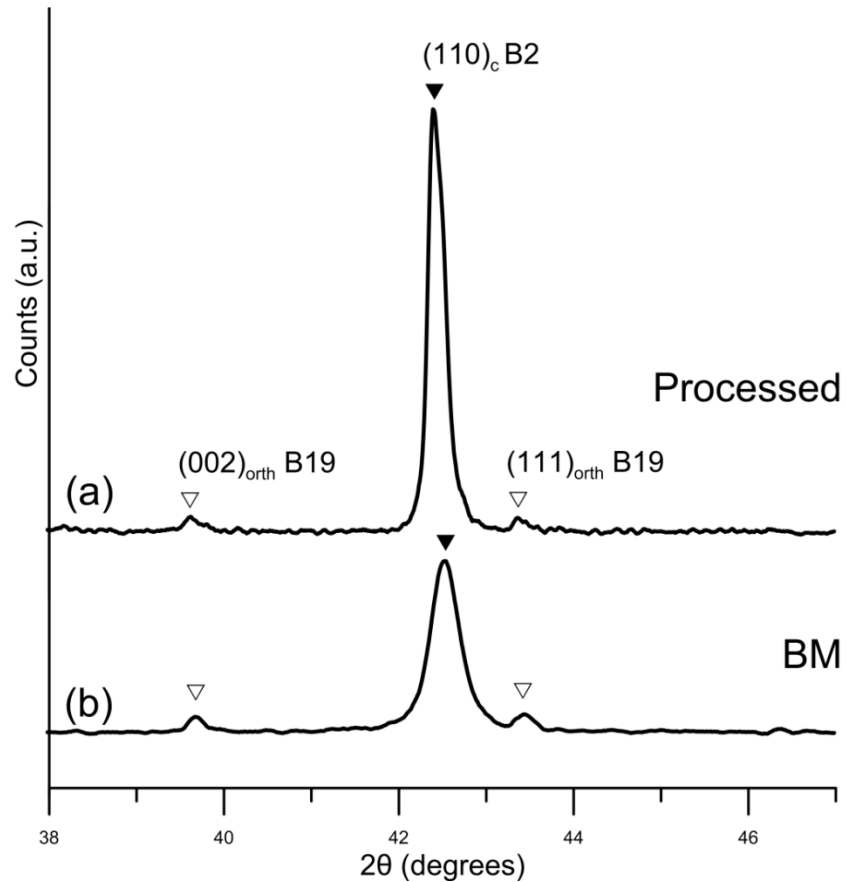


**Figure 3.6** X-ray Diffraction spectrum of B2 cubic austenite and partially transformed B19 orthorhombic martensite crystal of (a) 80% power processed specimen and b) BM.

DSC scans of the as-received material, solutionized BM, and laser processed specimens are shown in Figure 3.7 and their respective austenite finish, $A_f$, and martensite start, $M_s$, temperature are summarized in Table 3. The wide peak of the base metal is a characteristic of high dislocation density from thermo-mechanical processing of SMA wires [41]. The NiTiCu alloy was in the B2 austenite phase at room temperature (i.e. 25 °C). For the solutionized BM, the DSC peaks were narrowed and shifted to higher temperature by approximately 12K. The narrowing and shift of the transformation temperature was a result of the removal of internal stresses from cold-working and dissolution of intermetallics from the heat treatment process, much like an as-cast NiTiCu material. Comparing solutionized BM and as-cast material reported by Nam et al. [45], it was observed that both phase transformation behaviours were indeed identical.
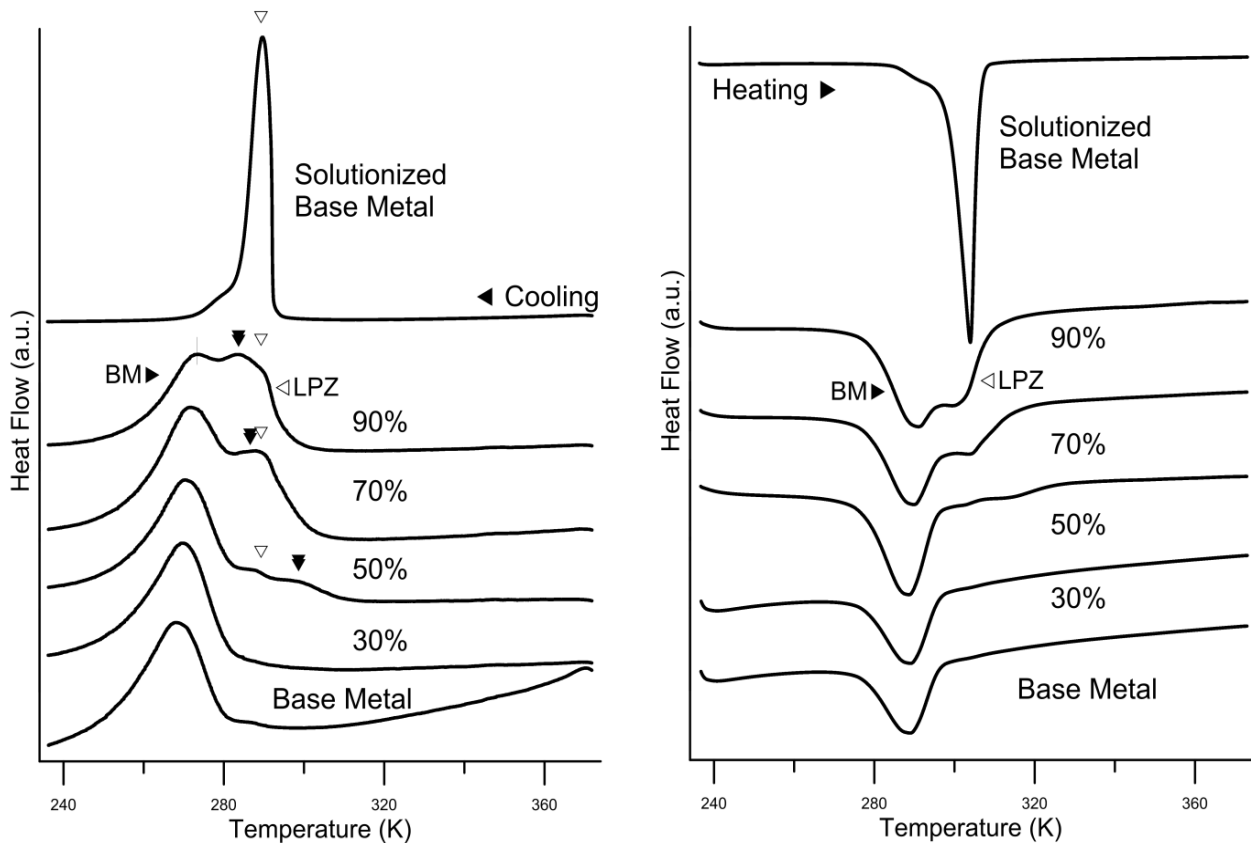


**Figure 3.7** DSC heating and cooling scans for base metal, solutionized wire, and wires of various laser processing parameters

35

**Table 3.** Onset phase transformation temperatures for as received base metal and base metal solutionized through annealing at 750(°C) for 1 hour.

| Wire Conditions | $A_f$ (K) | $M_s$(K) | $\Delta T_{peak}$ (K) |
|---|---|---|---|
| **As received BM** | 296.4 | 281.9 | 18.8 |
| **Solutionized BM** | 310.0 | 293.6 | 15.0 |
| **% of Peak Power (500W)** | | | |
| **30%** | No measurable change | | |
| **40%** | No measurable change | | |
| **50%** | 318.6 | 303.2 | 15.5 |
| **60%** | 321.1 | 302.0 | 14.2 |
| **70%** | 314.3 | 299.6 | 15.4 |
| **80%** | 309.5 | 295.4 | 16.2 |
| **90%** | 309.1 | 295.1 | 15.5 |

In the laser processed wires additional transformation peaks are observed in both heating and cooling curves. The additional peaks belonged to the LPZs in the samples, and their onset transformation temperatures are 13 to 22K higher than that of as-received BM. These peaks, labeled with non-filled triangles, are in the same location as solutionized BM. Many studies have reported similar localized change in phase transformation temperature in laser welded and resistance welded joints [16–18]. Studies done by Meng et al. indicate the mechanism behind the change is the removal of cold-work and heat treatment in the weld zone, similar to that of solutionizing treatment [111]. The most evident thermal peak shift can be observed at 90% peak power. The 90% power and solutionized BM have onset $A_f/M_s$ temperatures of 309.1 K / 295.1K and 310.0 K / 293.6 K, respectively. Both peaks also have similar transformation hysteresis of 15K, and it was clear that the major transformation temperature shift was through solutionization.

Composition change and segregation of alloying elements also could account for a minor transformation temperature change. A second set of shifted peaks, shown in black filled double triangles, appears with laser powers between 50% and 90%. From laser processing study by Khan et al., a small amount of target metal is removed through vapourization in each high energy laser pulse [112]. This study also confirmed similar decrease of Cu constituents at low power level, possibly due to vapourization. However, the reason for dependence of the second set of transformation temperature decrease on laser power was still unclear. Therefore, more accurate measurement technique will be required for exact assessment of elemental change.

## 3.3    Effects on mechanical properties

### 3.3.1    Effect of laser processing on hardness

Vicker's micro hardness measurements were made across the center of the LPZ cross sections of conduction mode and keyhole mode parameter, shown in Figure 3.8.  Base metal hardness was measured to be around 480 ±22 Hv 0.05/20, as expected from the fine-grain structure generated from cold-drawing wire fabrication process. Softening was observed in the LPZ and the HAZ for both modes of energy transfer.  Approximately 40% decrease in hardness value was seen in the lower power parameter and as much as 60% reduction in the keyhole mode. This phenomenon was caused by the recrystallization and the removal of cold-work, which had been previously observed in prior studies [16–18]. Therefore, the LPZ hardness was similar to average hardness of solutionized base metal, around 186 ±14 Hv0.05/20. It was strongly suggested by microstructural observation, XRD spectrum, DSC results, and corresponding hardness values that both conduction and keyhole mode LPZ showed a similar local solutionizing effect to that of resistance and laser welding [22, 118].
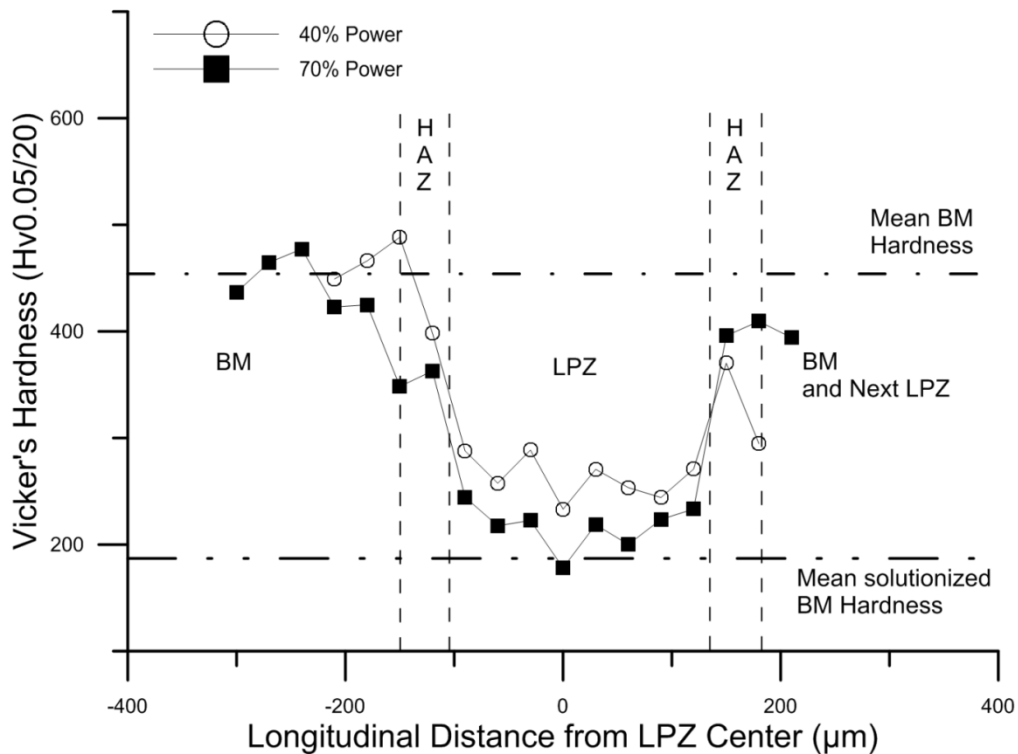


**Figure 3.8** Vicker's hardness profile across middle (1/2 *h*) of LPZ in conduction and keyhole mode

### 3.3.2 Pseudoelastic augmentation

Laser processing of NiTiCu alloy has been shown so far to locally solutionize the as-received BM. When laser processing was applied continuously across the length of the BM wire, a change was expected in the bulk mechanical response of the wire. Since the LPZ has shown to have mechanical property of a solutionized microstructure that is non-pseudoelastic, it was proposed that the increased volume of these non-pseudoelastic zones causes the proportionate decrease of the pseudoelastic response of the wire. To better control the PE modification, this work had set out to systematically uncover the relationship that exists between the LPZ geometry, the mechanical property change, and the processing parameters.

First, a relationship was observed between the LPZ volume fraction and laser processing parameters. Average volumes of the LPZ, $V_{LPZ}$, could be closely approximated as a trapezoidal cone with the method described in the experimental section 3.1.2. Following the dimension values shown in Table 1 and Eq. 1. The average fraction of LPZ volume in BM is determined by the fraction of LPZ volume divided by the base metal volume (635um x 465 um x $w$, top width of the LPZ). The volume fraction of the LPZ is summarized together in this section with together with laser power and augmentation in PE.

$$V_{LPZ} = \pi * \frac{h}{12} * (D_1{}^2 + D_1 D_2 + D_2{}^2) \qquad \text{(Eq. 1)}$$

The series of cyclic tensile plots shown in Figure 3.9 clearly showcases the modification of pseudoelastic property of the processed wires. The as-received material had a forward pseudoelastic force (FPF) of 327±12.5 MPa, return pseudoelastic force (RPF) of 170±12.5 MPa and residual strain of approximately 0.7 % according to the manufacturer which is shown experimentally in Figure 3.9 (a). On the other hand, (b) the solutionized wire had a FPF of about 139 MPa and a recovery of 1 % strain, which was typical for a solutionized austenitic SMA with no precipitation hardening and cold work [114]. Without thermo-mechanical treatment, critical stress for slip in NiTi family of alloys was much lower than the stress to induce martensite [60].

In Figure 3.9 (c-i), laser processed wires at 30, 40, 50, 60, 70, 80, and 90% peak power obtained FPF of 321, 299, 287, 266, 255, 241, and 236 MPa and RPF of 166, 157, 134, 123, 97, 82, and 79 MPa, respectively. Remarkably, as laser power increases from 30 to 90%, the RPFs decreases with no significant increase in residual strain.
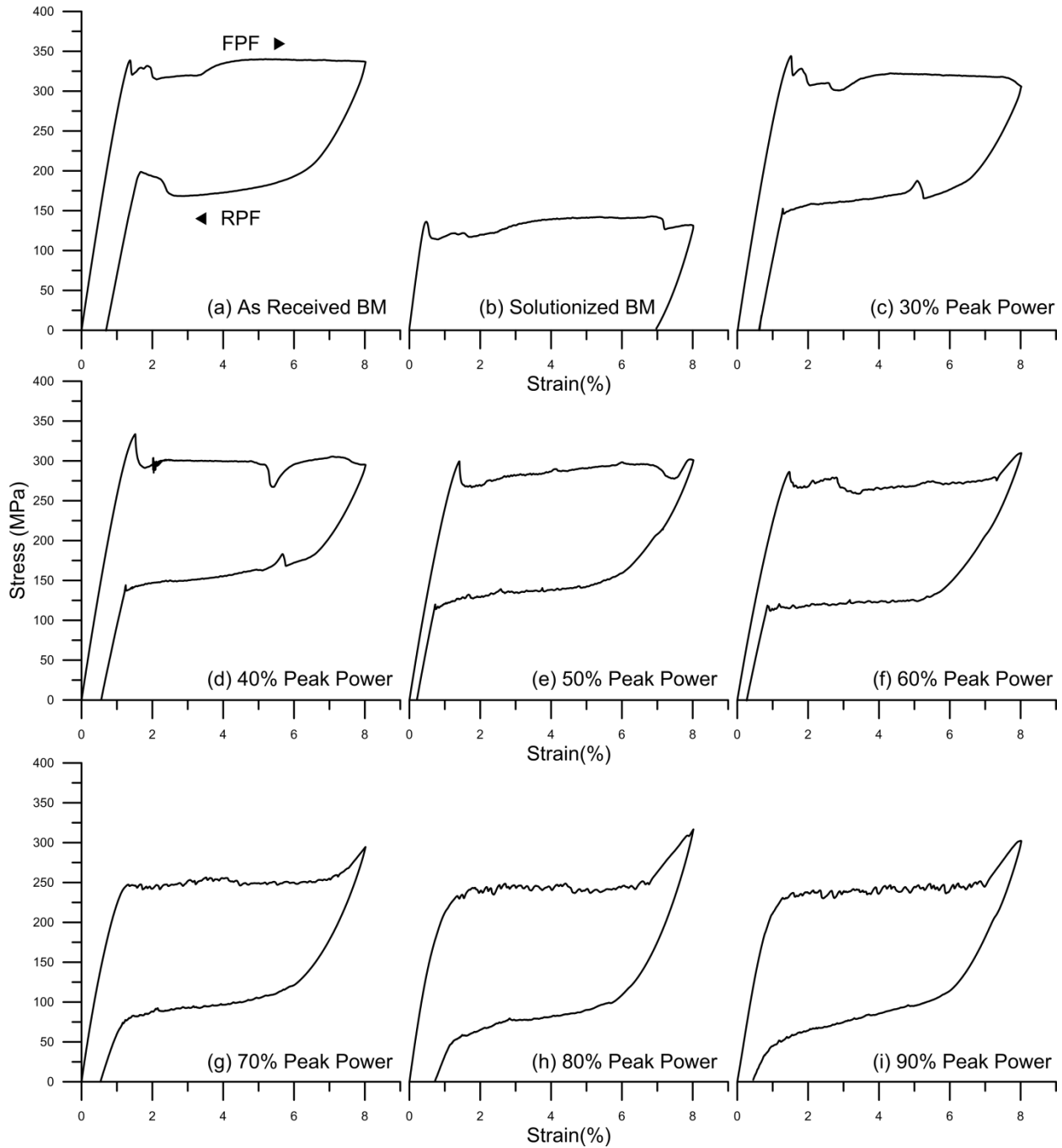
**Figure 3.9** Cyclic tensile test showing PE of (a)BM, (b) solutionized BM, and (c - i) PE augmentation by various laser parameters tested at 35°C

A summary of the LPZ volume fraction and RPF with respective laser processing power is shown in Figure 3.10. The RPF decreases gradually with increasing laser power. Laser processing at 30, 40, 50, 60, 70, 80, and 90% peak power created average fraction of 2.16%, 4.31%, 8.44%, 14.13%, 19.06%, 25.28%, and 29.67% LPZ volume in BM. The LPZ volume increases exponentially from conduction

39

mode parameters ($R^2$ =0.9999) and then follows a linear trend of increase in the keyhole mode ($R^2$ =0.9976).   LPZ microstructure from section 3.2.1 showed two modes of energy transfer, and the measurement of volume fraction confirmed the ranges of power where conduction mode and keyhole mode heat transfer occurs. From 0 to 40% power, the increase in volume was slow due to the inefficient anisotropic heat transfer mechanism of conduction mode. The transition mode was identified to be around 50% of peak power, above which energy transfers efficiently through keyhole heating.   On the other hand, the RPF and processing parameter showed slower decrease in the conduction mode parameters (30 and 50% peak power), steady decrease in the keyhole mode parameter, and slower again upon reaching full penetration at 90% power. The relationship between laser power, LPZ microstructure, and volume fraction seems clear; however, the correlation of PE augmentation to volume fraction and processing parameters is non-explicit.   Upon further exploration in the wire geometry a simple relationship was theorized, and a phenomenological model was proposed in the section 3.4.
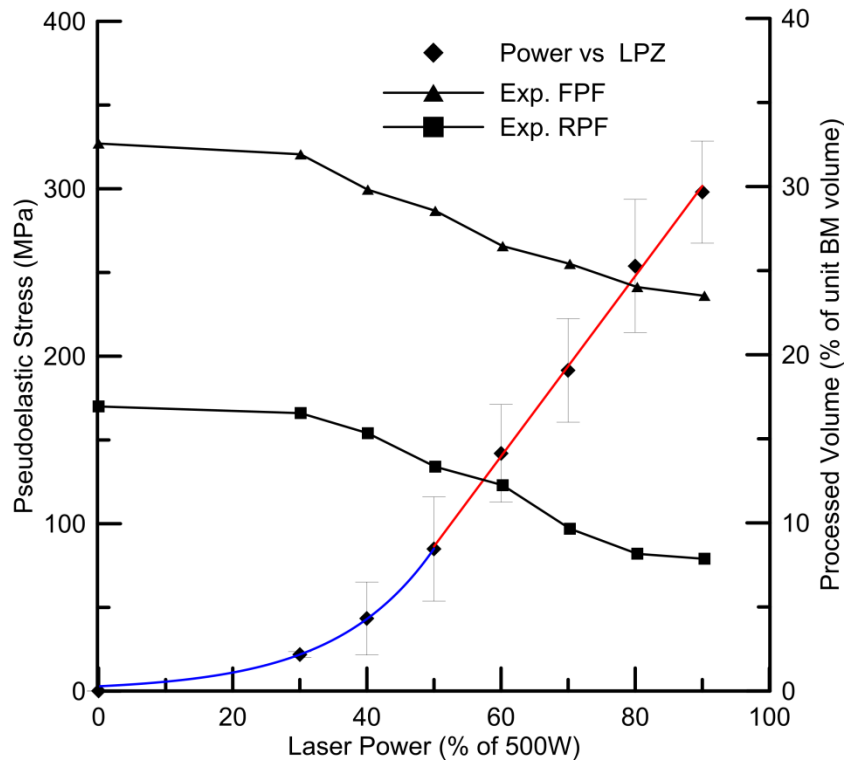


**Figure 3.10** Plot illustrating relationship of laser power on LPZ volume, forward and return pseudoelastic stresses at 35°C

### 3.3.3 Effect of laser processing on strain recovery

Since pseudoelastic SMA application requires maintenance of shapes and dimensions during the device life time, the effect of laser processing on the strain recovery was important factor to consider. In order to assess the strain recovery behaviour BM, low (30%) power and high (90%) power specimens were cycled 50 times up to 8% strain in microtensile tester. The results showed that low power processing has little effect on the strain recovery of the wire, whereas high power processing decreases the possible recovered strain by roughly 1% compared to BM. The solutionized LPZ was suspected to be work hardened during the cycling test, gradually increasing in rigidity, and decreasing recoverable strain. The resultant volume of LPZs from high power parameter was larger, and thus the larger residual strains were observed, as seen in Figure 3.11. The large residual strain could pose a problem for application.
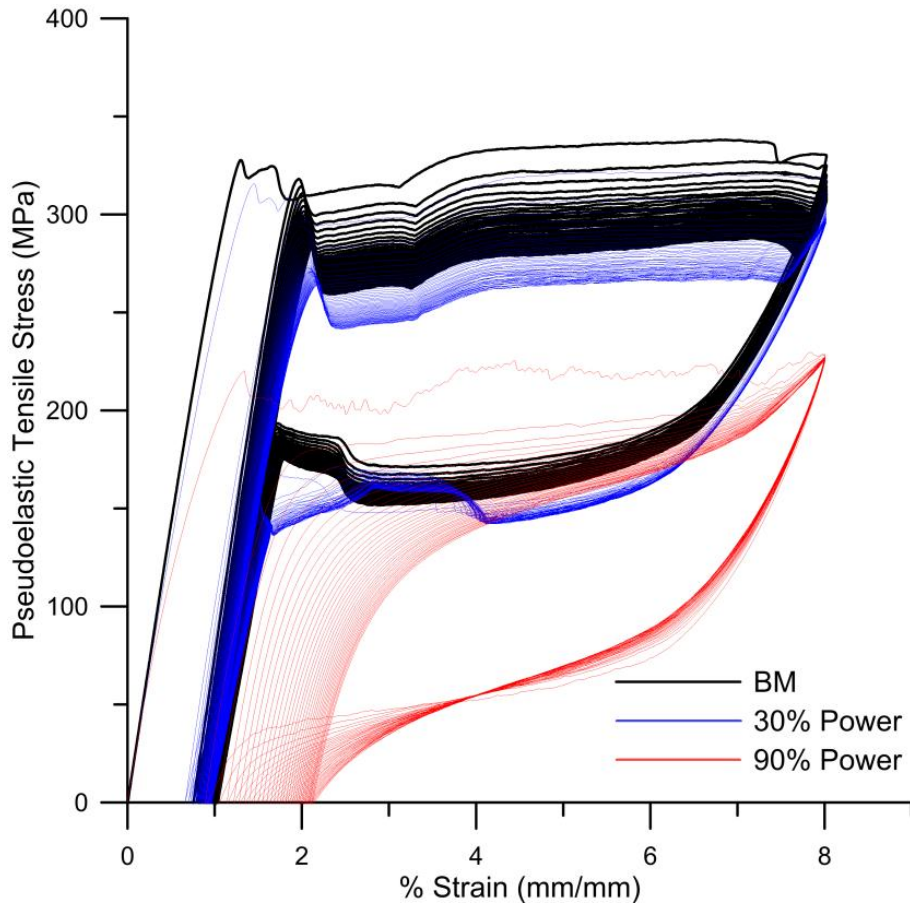


**Figure 3.11** Mechanical cycling response of BM and laser processed NiTiCu SMA wires during 50 cycles. High power processing exhibits 1% reduction in strain recovery compared to BM after cycling. Perfect PE (strain recovery) achieved after approximately 30 cycles.

41

### 3.3.4 Effect of laser processing on bending characteristics

Bending force is highly relevant to orthodontic and medical stent devices [6, 9, 10], and notably, the laser PE augmentation is not only observed in tension. The bending forces had demonstrated distinct reduction with increasing laser processing power, as shown in Figure 3.12. Taken at 2mm deflection, the return bending forces were 3.15, 2.95, 2.32, and 1.47 N for BM, 40%, 60%, and 80% power specimens respectively. At the same time, the residual deflection from bending increases with laser power as well, which were 0.039, 0.093, 0.11, and 0.19 mm for BM, 40%, 60%, and 80% power specimens, respectively. The increased residual strain observed in tensile and bending tests could negatively affect the flexibility of design of the SMA wire, therefore, further research on different laser parameters is required to reduce the residual strain build up observed under high power conditions.
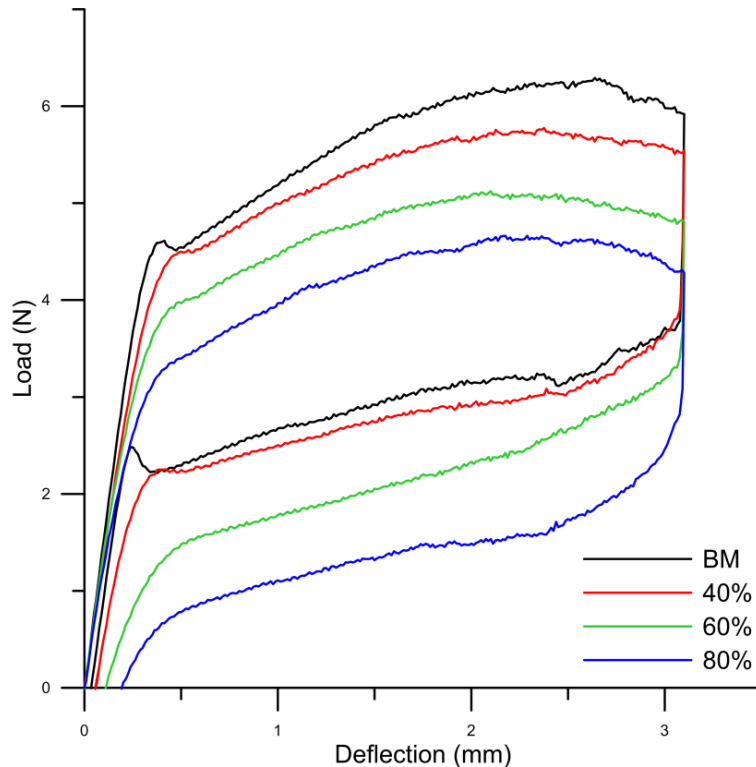


**Figure 3.12** Three point bending response of base metal, 40%, 60%, and 80% peak power wires modified through MMM processing.

## 3.4    Mechanism responsible for modification of PE

Based on the mechanical property observations, the current investigation theorized that the mechanism behind the pseudoelastic force modification is the effect of the replacement of a portion of the BM by a series of LPZs along the wire material. The LPZ hardness and tensile property had been established similar to that of solutionized BM. Thus, during the forward tensile cycle of the processed

wire, force contributions were no longer only from the BM and became 1) plastic deformation of the LPZ through the low stress slip mechanism and 2) diffusionless phase transformation of the BM from B2 austenite phase to B19' stress induced martensite phase (SIM). In the return cycle, the force contributions were 1) the reverse phase transforms of the BM from B19' to B2 and 2) the compression of the deformed LPZ back to the original gauge length by the neighbuoring pseudoelastic BM. The forward PE force was decreased from having less BM undergoing forward SIM transformations, whereas the return plateau was decreased from having less BM undergoing reverse transformation. Still, the softened LPZ was only partially responsible for the modification of pseudoelastic force.

### 3.4.1 Theorized LPZ and base metal interaction

Illustrated in Figure 3.13①, it is important to note that the section of BM between LPZs should be mostly static during the entirety of the tensile loading cycle. This assumption was made based on the observation that the LPZ deforms at much lower stress than the BM. In theory, the interstitial static BM (SBM), which is stronger, will only deform very little because the LPZ was much softer, similar to that of the solutionized BM shown in Figure 3.9 (b). The applied stress was likely to be concentrated on the straining of the LPZ and not the interstitial SBM, illustrated in Figure 3.14 ②. Thus, only the BM surrounding the non-PE band, which was composed of volume of LPZ and static BM region, undergoes stressed induced transformation. The combined SBM and the LPZ essentially forms a rough trapezoidal prism of non-pseudoelastic wire (shown in blue) embedded in the BM wire.
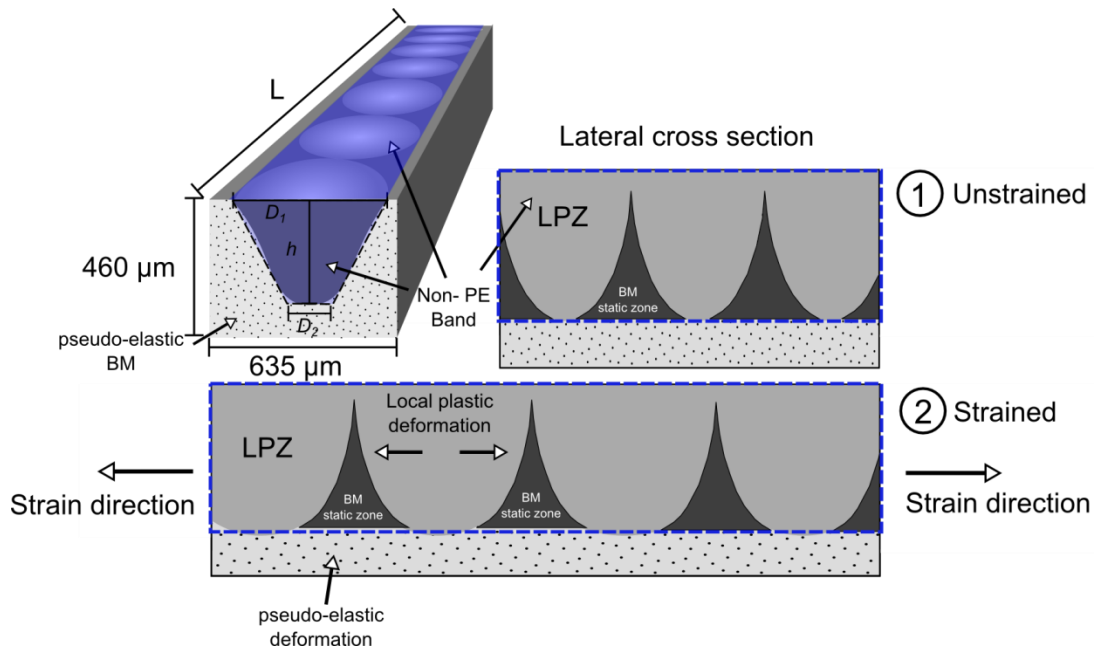


**Figure 3.13** Schematic diagram showing cross section of MMM processed wire in equilibrium and strained conditions.

43

### 3.4.2   Phenomenological model

Following the assumption that a trapezoidal prism of non-pseudoelastic material existed in the processed wire, a phenomenological model for the FPF and RPF after laser processing was proposed by drawing relationships between the geometry of the BM and the volume of the non-pseudoelastic region. The FPF response was theorized to be the sum of the tensile stress response of the retained BM and the trapezoidal prism formed by LPZ and SBM. The relationship of the modified FPF was simplified into an area fraction of LPZ and BM, since the variation in area fraction length-wise was negligible in a trapezoidal prism in a rectangular bar. The FPF phenomenological model based on area fraction is theorized as followed:

$$FPF = \ FPF_{BM} \ * \left(1 - \frac{A_{LPZ}}{A_{BM}}\right) + FPF_{LPZ} * \left(\frac{A_{LPZ}}{A_{BM}}\right) \qquad \text{(Eq. 2)}$$

where $FPF$ is the predicted FPF of the laser processed wire, $FPF_{BM}$ is FPF of the base metal , $FPF_{LPZ}$ is the approximated FPF of the LPZ, $A_{LPZ}$ is the cross sectional area of the LPZ, and $A_{BM}$ is the area of the BM. FPF of solutionized BM was substituted as the $FPF_{LPZ}$ for their similarity in thermomechanical performance.

The same system can be applied to model the RPF. The contributions to the RPF were theorized to be the reverse phase transformation of the SIM subtracted by the resistive force exerted by the deformed LPZs. Since the force used to compress the deformed LPZ is small and hard to measure, the RPF derivation will only take the BM volume fraction into account and factor the compression stress of the LPZ into uncertainty. Applying similar substitution of common lengths, the RPF model of the technique can be simplified to the following:

$$RPF = RPF_{BM} * \left(1 - \frac{A_{LPZ}}{A_{BM}}\right) \qquad \text{(Eq. 3)}$$

In Figure 3.14, the experimental pseudoelastic forces and experimental non-pseudoelastic volume is plotted along with the phenomenological model. The $FPF_{BM}$ and $RPF_{BM}$ values are taken from 4% strain mark of the base metal curve shown in Figure 3.9 (a), and $FPF_{LPZ}$ value are taken from 4% strain mark of the solutionized base metal curve shown in Figure 3.9 (b). The model showed a $R^2$ value of 0.9412 with sample size of 30 when predicting the tuned FPF. The model has a $R^2$ value of 0.9526 when

44

predicting the experimental RPF. The near 5~6% error could be attributed to the trapezoidal prism approximation for the bell-shaped volume of the LPZ, the uncertainty in the compression stress of the LPZ, as well as the manufacturer's variances in PE of the BM (±12.5MPa). The LPZ and BM interaction was understood to be complex, and the phenomenological model could be further improved with more systematic research in the microstructural interaction under strain.

This phenomenological model proposed a method to predict PE augmentation in a single monolithic wire through a fibre laser processing. Multiple pseudoelastic responses are now possible in a single SMA component and the method could extend to other types of NiTi-based SMA devices. A proof of concept of multiple plateaus is shown in Figure 3.15, where a double pseudoelastic response from a monolithic SMA wire with equal parts BM and laser processed sections is presented. To the best of the authors' knowledge, this laser processing technique was the first example of an SMA processing technique that enables PE augmentation with extremely high degree of mechanical and positional accuracy.
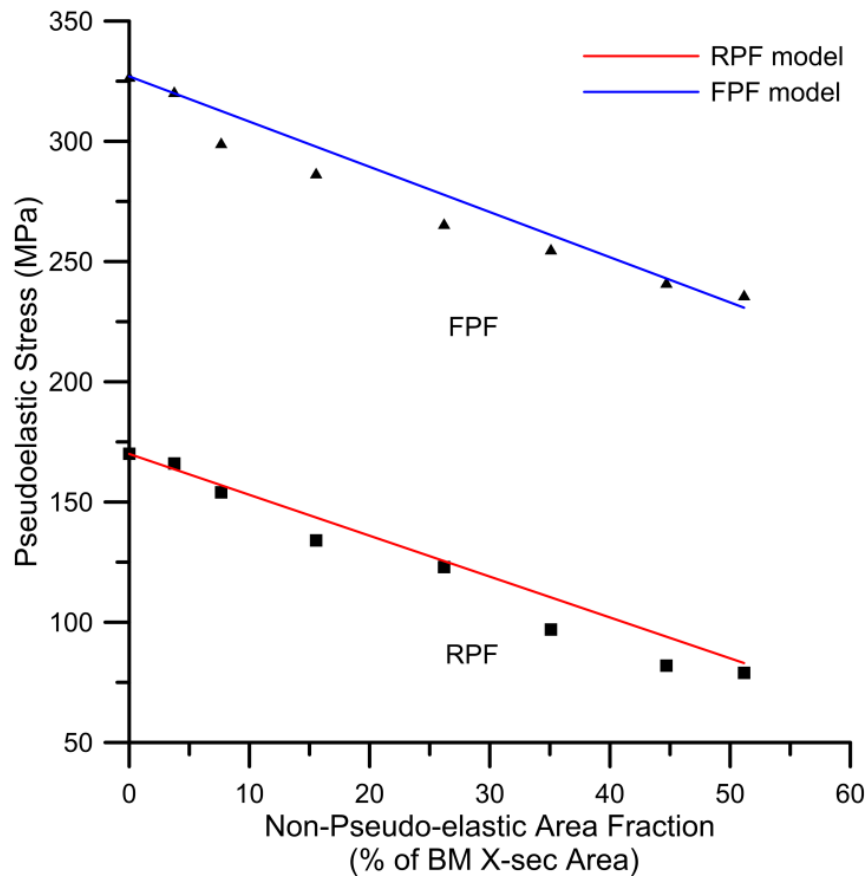


**Figure 3.14** Plot of (1) experimental FPF and RPF versus area fraction of the trapezoid in the base metal and (2) the phenomenological model approximation of the pseudoelastic augmentation

45
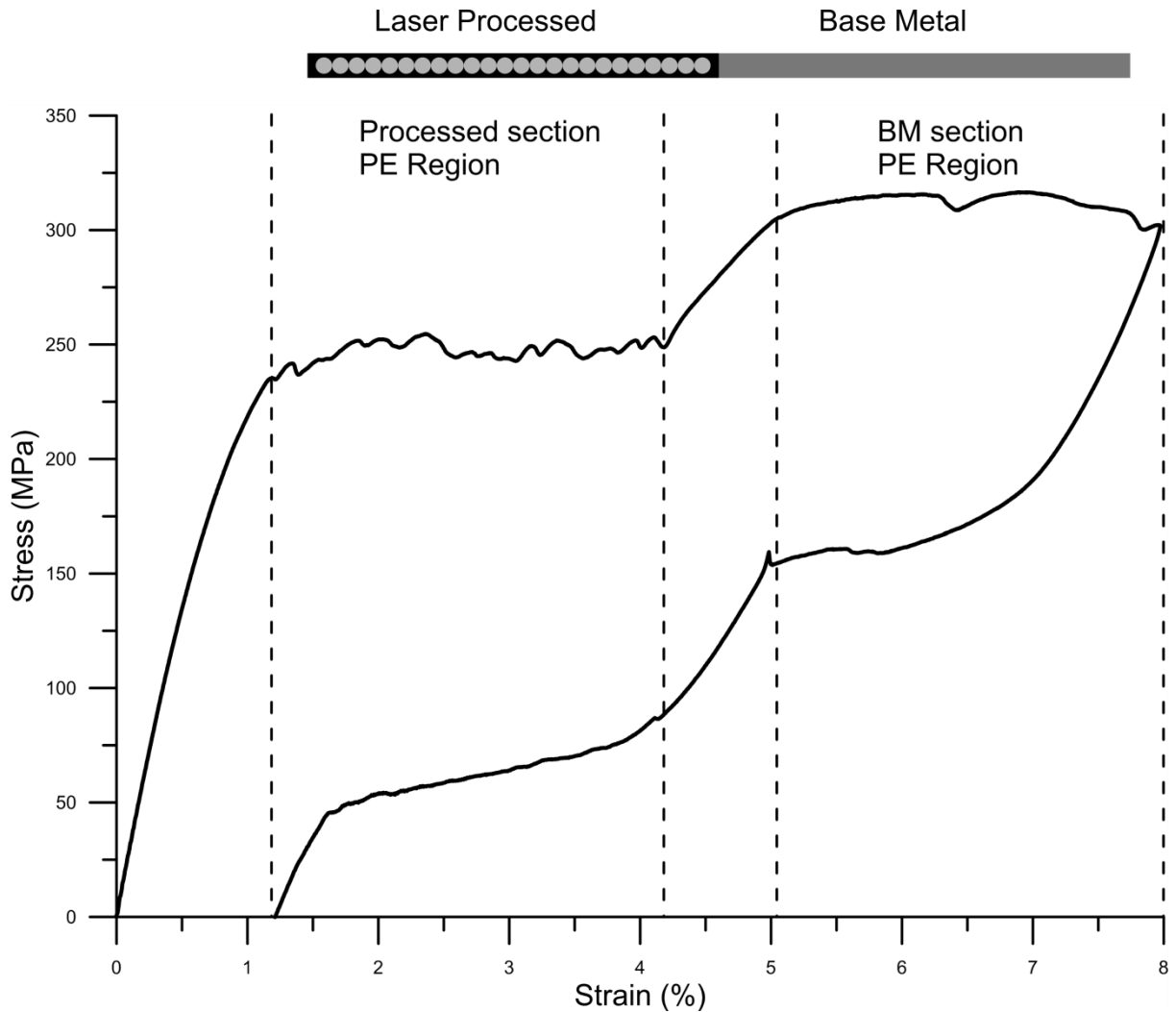
**Figure 3.15** Double pseudoelastic response of a monolithic wire with equal parts BM and laser processed sections, showing two distinct plateaus at 35°C. Half of the sample was laser processed at 80% peak power at 10μs.

## 3.5    Chapter summary

The multiple memory material technology was shown to precisely augment pseudoelastic properties in monolithic SMA wires. Furthermore, a relationship was identified between the laser power, the dimension of the LPZ, the mechanical behaviour of the LPZ, and the reduction in the pseudoelastic plateau stress. Investigation of the LPZ dimension showed an exponential growth in conduction mode energy transfer and a linear growth in the keyhole mode energy transfer. The localized melting and solidification was linked to a solutionizing effect in the LPZ. Thus, subsequent application of the laser processing through the middle of the wire achieves augmentation of the pseudoelastic plateau stresses. Moreover, the bending characteristic, a major design factor in medical implants, could also be modified with the same processing technique. The change in PE was dependent on the laser power and the change

46

in geometry of LPZ, and thus, a phenomenological model for the augmented PE was theorized through the interaction between the BM and the LPZ. The model could predict the pseudoelasticity with good accuracy, but more in depth study of the complex interaction is needed. The capability for precise control over pseudoelastic property of SMA materials shall offer tremendous improvement to the design freedom and the functionality of SMA devices.

# Chapter 4

## 4. Effect of laser processing on corrosion performance of NiTi strips

Nitinol surface characterization studies have often shown complications that arise due to the large strains attained resulting from the pseudoelastic effect. Through literature review, recent research direction has focused on bare surface treatments to achieve surface defect removal [106] and increasing Ti surface concentration [93]. The MMM laser processing technique has demonstrated the ability to selectively remove Ni from the NiTi metal and achieve added functionalities in shape memory and pseudoelastic effects [28]. At the same time, the removal of Ni may also achieve better corrosion properties. It was hypothesized that, due to an increase in Ti content and improvement in surface condition, the corrosion performance of the processed material should be improved. The surface formation of laser melted SMA is complicated by many factors including the new composition of SMA alloy near the surface, the heat input from the laser source, and the ambient atmosphere during processing.

The purpose of this investigation was to study the fundamental contributions to the change in corrosion resistance resulting from MMM processing. Due to the multiple factors affecting corrosion behaviour, this work was simplified by using a binary NiTi material. Also, the focus of this study was on the effects of the altered Ti:Ni ratio and microstructure by standardizing the surface morphology via mechanical polishing. The newly formed surface oxide profiles were analyzed with X-ray photoelectron spectroscopy (XPS) and EDX. The corrosion resistance behaviour was investigated through cyclic polarization and Ni-ion release testing in simulated biological environments.

## 4.1 Experimental

### 4.1.1 Sample preparation and laser processing

The NiTi samples used were SE508 Nitinol strip manufactured by Nitinol Devices and Components (NDC) Inc. with composition of 50.8 at % Ni and 49.2 at% Ti. The thick surface oxide on NiTi formed during thermomechanical processing was etched with $HF+HO_3$ mixture (7.5 wt% of HF and 20 wt. % of $HNO_3$) for five minutes and cleaned with deionized water prior to laser processing. Figure 4.1 (a) shows a typical laser processing fixture set up. Samples were clamped in a custom fixture for processing the strip material. An Ar shielding gas was supplied on both the top and bottom of the sample to prevent oxidation. Laser processing of the NiTi strip was performed with a Miyachi Unitek model LW50-A pulsed Nd:YAG laser having a 1.06 μm wavelength, top hat spatial profile, and a 600 um spot size. Figure 4.1 (b) shows the laser spot profile and overlap configuration. The laser protocol used was

0.8 kW with a 4 ms full power, 6 ms downslope profile. Sheet samples were processed with series of laser spots with 56% overlap between spots to ensure homogenous coverage. The overlap was defined as a percentage of the diameter of the laser spots, which in this case was 1000 um. Each laser spot received three or five laser pulses, which was tailored to produce medium or high change in surface chemistry. The sample names and fabrication methods are organized and listed in Table 4.

**Table 4.** List of surface treatments of BM NiTi, and processed samples

| Treatments<br>Samples | HF/HNO$_3$<br>Acid etch | Laser processing<br>(0.8 kW, custom profile) | Mechanical<br>polishing | Number<br>of Samples |
|---|---|---|---|---|
| BM NiTi | ✓ | | ✓ | 4 |
| 3 pulse | ✓ | ✓, 3 pulse, 56% overlap | ✓ | 4 |
| 5 pulse | ✓ | ✓, 5 pulse, 56% overlap | ✓ | 4 |
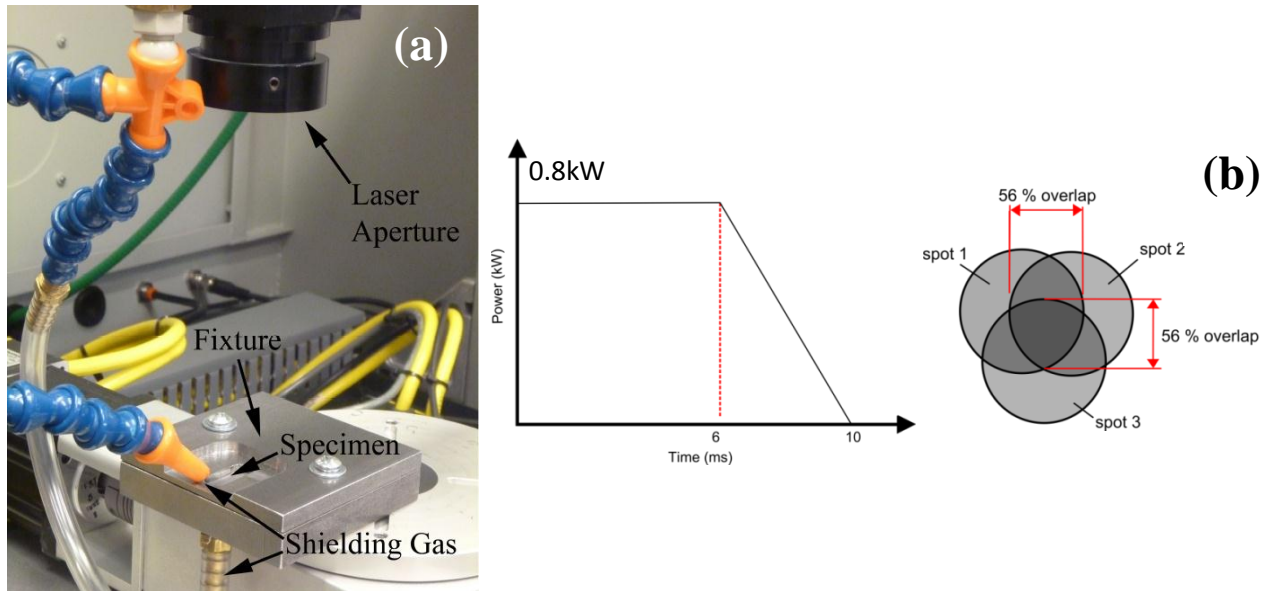


**Figure 4.1** (a) Laser set-up for processing NiTi sheet. The sheet was clamped in the fixture with Ar shielding gas blowing on top and bottom to prevent oxidation. (b) Laser pulsing parameter and overlap configuration for processing NiTi sheets.

The average surface roughness ($R_a$) of NiTi strip after etching, laser processing, and polishing was respectively 1.30 μm, 2.06 μm, and 5.74 nm, according to 3D optical profilometry analysis provide in Figure 4.2. The as-etched base metal and processed metal, shown in Figure 4.2 (a) and (b), differed greatly in surface morphology, which was not the focus of this study. Polishing surfaces of all the samples ensured that the comparative study was only affected by change in surface chemistry and the

49

resultant passivation layer morphology.    Mechanical polishing procedure started with grinding sequentially with silicon-carbide paper of 400 to 1200-fine grit and then polishing with colloidal silica suspension with 10% of $H_2O_2$ (30 wt.%) by volume.   The polished surface is shown in Figure 4.2 (c).
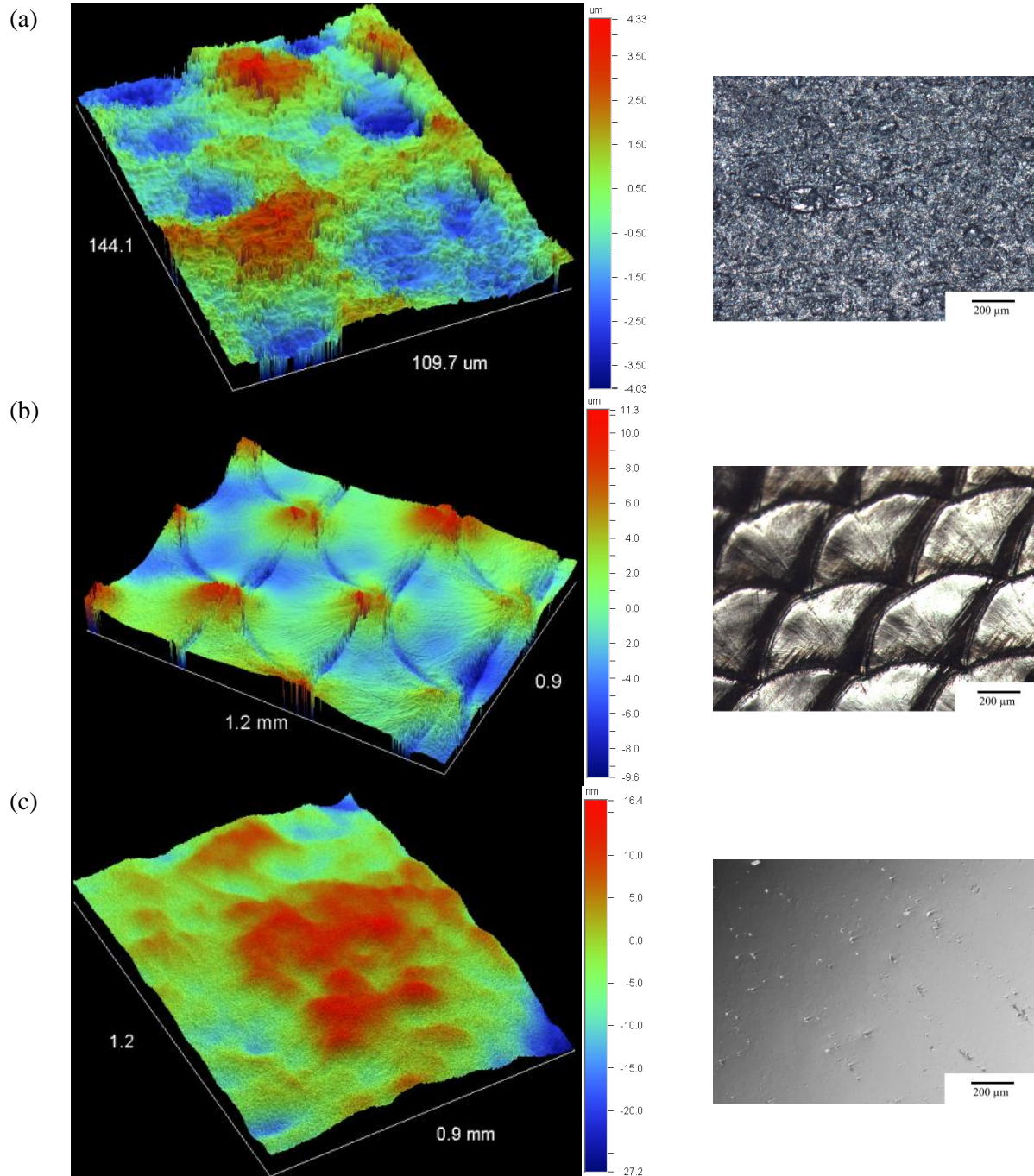


**Figure 4.2**  Surface profiles from 3D optical profilometer and corresponding optical microscopy images of NiTi strips used in corrosion tests (a) after etching and (b) laser processed, (c) mechanically polished.

### 4.1.2 Cyclic potentiodynamic polarization

Cyclic potentiodynamic polarization (cyclic polarization) is a standardized accelerated corrosion simulation test for metals and metal alloys established for ease of comparison between studies. Specifically, ASTM standard F2129, which this work closely followed, outlines a method for conducting cyclic potentiodynamic polarization for determining the corrosion susceptibility of small implant devices.

Cyclic polarization tests were carried out in a double layer cell with the inner cell containing a biology grade phosphate buffered saline (PBS) electrolyte at pH 7.4. Chemical composition of the PBS consisted of following: 8.0 g/L of NaCl, 0.2 g/L of KCl, 1.15 g/L of $Na_2HPO_4$, and 0.2 g/L of $KH_2PO_4$. Throughout the test, the electrolyte solution was purged with $N_2$ gas at a rate of 50 ml/min. Outer layer of the cell was connected to a temperature regulated heater pump that kept the entire cell at $37^{o}C \pm 0.5^{o}C$. The reference electrode used was a standard calomel electrode (SCE) in a KCl salt bridge ($233 \pm 10$ mV versus SHE in $37^{o}C$). A platinum wire mesh was used as the counter electrode. The working electrode was custom made with an active area of $0.25cm^2$, following the ASTM standard, shown in Figure 4.3(a) and (b), respectively. Samples were secured at the tip of the brass rod by a rubber washer and a Teflon® cap. Figure 4.4 provides a photograph of the experimental corrosion cell during test and the ASTM standard F2129 corrosion cell set up, which was followed closely. Gamry Instruments Series G-300 potentiostat was used as voltage supply and data acquisition for this experiment. All the voltage mentioned in this work will be with respect to SCE. Applied potential was to scan from -0.7 to 1.45V and from 1.45V to -0.3V at a rate of 0.167 mV/s. All the samples tested in this experiment are listed in Table 4, and four cyclic polarization tests were conducted for each NiTi BM, 3 pulse, and 5 pulse samples to generate good resolution in data for analysis.
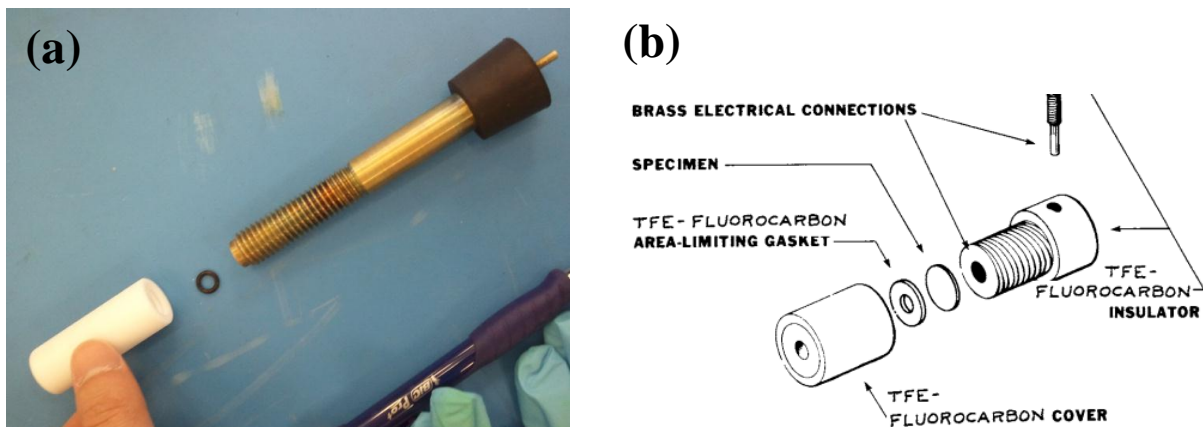


**Figure 4.3** Cyclic polarization electrode (a) custom made probe, with Teflon cap (white), Rubber o-ring washer, and brass rod. The sample will be held between the washer and the bass rod. (b)ASTM standard set up showing similar configuration.
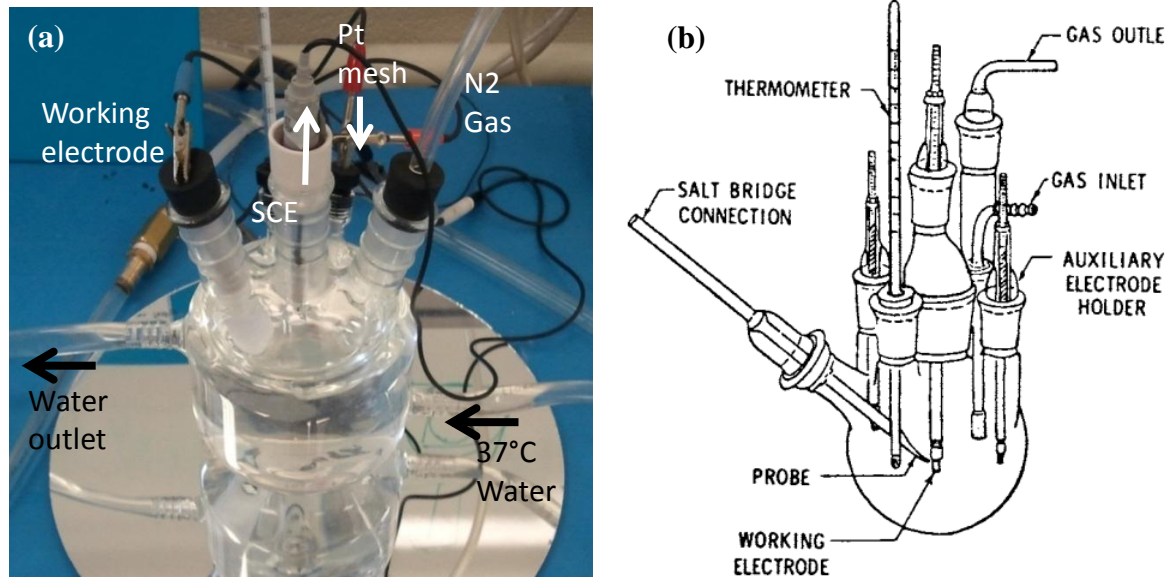
**Figure 4.4** (a) Cyclic polarization cell with double layer temperature control, built according to (b) ASTM Standards F2129 for Cyclic polarization testing for implant materials.

### 4.1.3 Ni ion release test

Ion release tests are benchmark for release of metal ions of implants, especially for toxic ions like lead and allergenic ions such as nickel present in this study. Each sample was 0.25 cm$^2$ in size and immersed in 30 mL of phosphate buffered saline (PBS) solution at 37.5$^o$C for 18 days. All 30 mL of solution were taken out and replenished after 1, 24, 72, 144, 240, 360, 432 hours, and stored for ICP analysis. Ion concentration detection was done readily through Prodigy inductive coupled plasma atomic emission spectroscopy (ICP AES) (Teledyne Leeman Labs Company). Each sample was scanned five times with 10 second per scan to achieve good average. Lower limit of detection (LLOD) of ICP AES is 9.7 ppb for Ni ions. (1 ppb = 1 μg/mL).

### 4.1.4 Analytical Methods

To analyze the surface chemistry, two sets of composition were investigated. First, the bulk compositional analysis of the laser processed spots was conducted using a Jeol JSM-6460 scanning electron microscope equipped with an INCA energy system 350 EDX microanalysis system. EDS specimens were cross-sectioned and mechanically polished. Surface oxide thickness and surface depth composition profiles were analyzed with Thermo Scientific K-Alpha X-ray photoelectron spectroscopy (XPS). XPS scans were coupled with argon plasma sputtering, which etches away surface during scanning to achieve the depth composition profile. Prior to the XPS test, the samples were polarized electrochemically from -650mV to 200mV above their equilibrium potential at 0.167mV/s. The purpose

of the polarization was to allow the XPS investigation to be an accurate capture of the surface oxide composition during the passivation portion of the cyclic polarization curve.

## 4.2        Results and discussion

### 4.2.1   Compositional analysis – EDX and XPS

Bulk compositions of BM and laser processed NiTi strips are presented in Figure 4.5. For the BM, the atomic percent of Ti and Ni were measured to be 50.1% and 49.9%, respectively. This result did not match the reported Ni to Ti ratio from the supplier, likely due to accuracy of EDX (±0.5 at%); however, the relative difference was still significant data. An increase in Ti:Ni ratio was observed in the bulk of the processed samples. The 3 pulse sample had 51 at% of Ti and 49 at% of Ni, and the 5 pulse sample had 52 at% of Ti and 48 at% of Ni. An incremental decrease of Ni with laser pulse also confirmed the findings reported by MMM related studies [28–30]. This increase in Ti:Ni ratio should show differential oxide formation and corrosion behaviour, presented in the following sections.
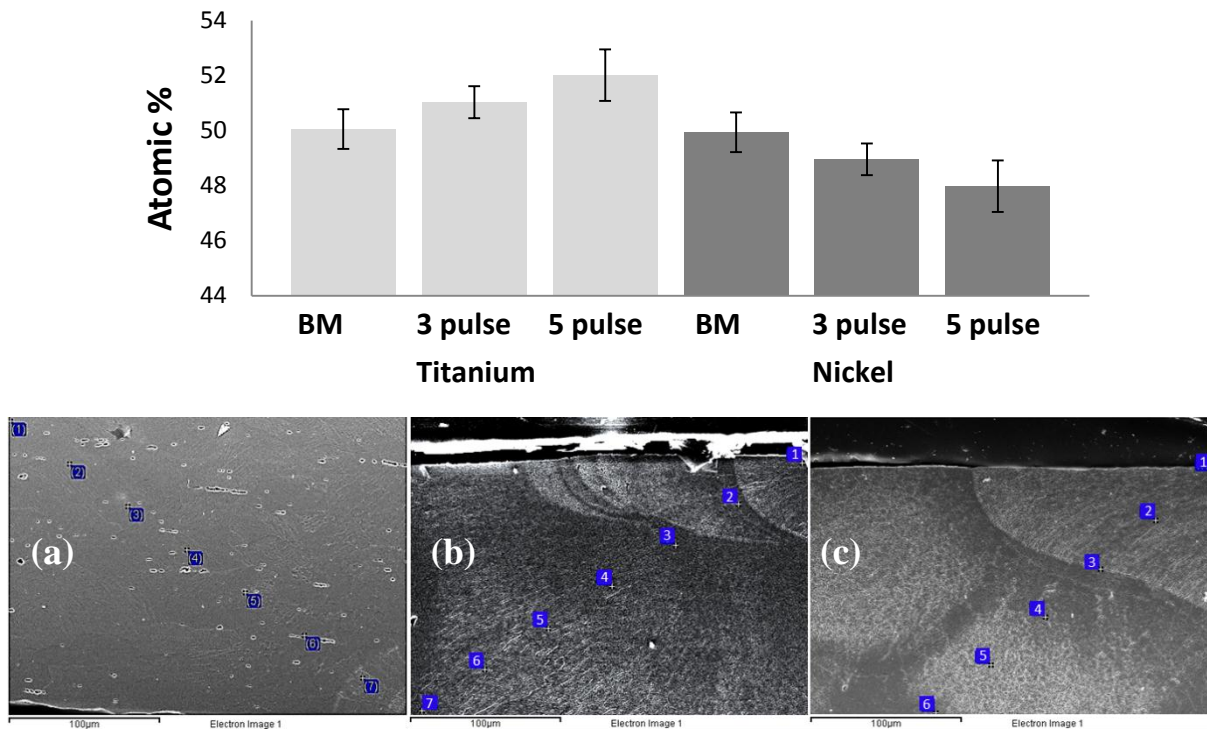


**Figure 4.5** Plot of average bulk composition analysis from EDS and SEM cross sectional image of NiTi (a) base metal (BM), (b) 3 pulse sample and (c) 5 pulse sample. Ti:Ni ratio increased with laser pulsing.

Surface oxide thickness and surface depth composition profiles of BM and 5 pulse samples are presented in Figure 4.6. Sample depth of XPS scans is directly correlated to the sputtering time. The Ni-2P3, Ti-2P, and O-1s electron shell signals corresponded to the relative concentrations of each element in the BM and laser processed sample. Selected values are summarized in Table 5 for ease of comparison.
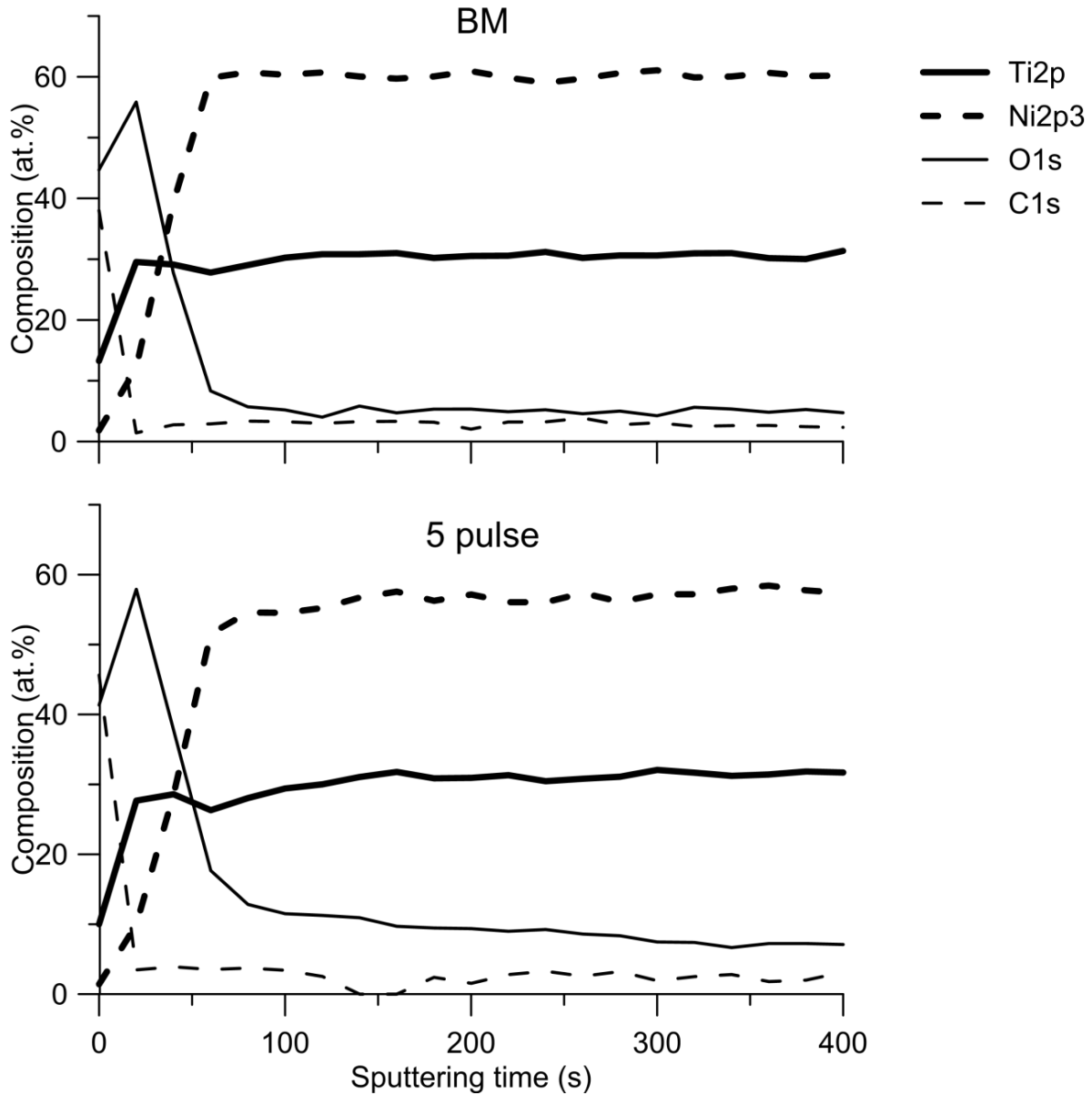


**Figure 4.6** XPS depth profiles of NiTi base metal and 5 pulse sample.

**Table 5.** Relative concentration of surface elements as measured by XPS

| Sputtering time (sec) | Sample | Ni – 2p3 (at %) | Ti – 2p (at %) | O – 1s (at %) | C – 1s (at %) |
|---|---|---|---|---|---|
| **0** | BM | 1.83 | 13.26 | 44.69 | 38.01 |
| | 5 pulse | 1.42 | 10.01 | 41.35 | 45.63 |
| **20** | BM | 12.11 | 29.54 | 55.85 | 1.44 |
| | 5 pulse | 9.96 | 27.67 | 57.91 | 3.47 |
| **40** | BM | 39.32 | 29.12 | 27.74 | 2.76 |
| | 5 pulse | 28.52 | 28.59 | 37.79 | 3.91 |
| **80** | BM | 60.73 | 29.02 | 5.71 | 3.36 |
| | 5 pulse | 54.59 | 28.05 | 12.83 | 3.73 |
| **200-400 (average)** | BM | 60.19 | 30.66 | 5.01 | 2.80 |
| | 5 pulse | 57.15 | 31.32 | 7.97 | 2.51 |

The XPS measurements showed that the 5 pulse sample had lower Ni concentration and thicker oxide layer than that of BM. Near the surface, the Ni concentration was also significantly reduced through laser ablation, from 39 at% to 28% at 40s sputtering time. Similar lower Ni concentration was observed throughout the surface layer from 0 to 80s sputtering time. At high sputtering times from 200s to 400s, an average of 3% decrease in Ni concentration was observed in 5 pulse sample. The decrease in Ni-2P3 and increase in Ti-2P shell signals corresponded well to the amount decrease in Ni concentration obtained through the EDX analysis. Oxide thickness, determined at the intercept of Ti-2P and O-1s signals, was observed to be higher in the processed sample (~55s) than BM (~39s). Furthermore, the oxygen concentration was higher overall through the thickness of the oxide, around 7.97 at% for 5 pulse sample and 5.01 at% for BM. The cause of this could be oxygen mixing in the laser melted zones from the impurity of the Ar shielding. Carbon contamination of the surface could also be mixed in the bulk composition during laser melting, causing higher surface carbon concentration.

Overall, the surface composition indicated that the polished laser processed sample formed a thicker $TiO_2$ layer with less Ni impurity than BM. The increase in oxide thickness and decrease in Ni concentration near the surface and in the bulk material was expected to have a positive impact on the corrosion resistance and the direct decrease in Ni release, as presented in the following sections.

### 4.2.2   Effects of laser processing on corrosion performance

Figure 4.7 (a) presents three polarization curves of NiTi BM, 3 pulse, and 5 pulse samples; selected from their statistical median. All of the polarization curves are provided in Appendix I. The average corrosion potential, breakdown potential, protection potential, and protection current are summarized in Table 6. The values were obtained with assistance of Gamry Echem Analyst v5.61 with exception of protection potential and current, which were determined at the first intercept of forward and reverse current after breakdown had occurred.

The three NiTi cyclic curves differs very slightly in terms of magnitude of protection current, breakdown potential, protection potential, and passivation hysteresis. Similarity at the high potential region indicated that the pitting and self-healing behaviours were invariant to the laser processing and composition change.

The key differences between processed and BM samples were their corrosion potentials and corrosion current at low potentials, shown more clearly in Figure 4.7(b). The BM, 3 pulse, 5 pulse had $E_{corr}$ of -0.34 , -0.29, and -0.27V vs SCE respectively. Comparing current at -0.05V vs SCE, the current of 3 pulse and 5 pulse samples were roughly 500% and 360% lower, respectively, than that of BM. The increase in $E_{corr}$ of processed samples indicated an overall decrease in surface reactivity compared to base metal. Decrease in current indicated a decrease in corrosion rate and charge transfer. Villermaux et al. has shown that a similar enhancement of NiTi corrosion potential and current is observed when surface oxide thickness increased from 7.5 to 20 nm [106]. Many laser welding studies in literature have reported improvement of corrosion potential and corrosion rate in processed NiTi samples [12, 31, 93]. Likewise, the improvements in the current investigation of laser processed NiTi could be attributed to the thicker $TiO_2$ layer on the laser processed surface as seen in XPS analysis.

**Table 6.** Summary of average key cyclic polarization values

| Samples | $E_{corr}$(V vs SCE) | $E_{break}$(V vs SCE) | $E_{prot}$(V vs SCE) | $I_{prot}$ (A) | I (A) at 0.05V vs SCE |
|---|---|---|---|---|---|
| NiTi base metal | -0.34 | 1.20 | 0.90 | $1.33 \times 10^{-6}$ | $4.03 \times 10^{-7}$ |
| 3 pulse sample | -0.29 | 1.20 | 0.91 | $6.60 \times 10^{-7}$ | $7.51 \times 10^{-8}$ |
| 5 pulse sample | -0.27 | 1.18 | 0.90 | $7.73 \times 10^{-7}$ | $1.09 \times 10^{-7}$ |

Comparing 3 pulse to the 5 pulse sample, the increase in laser pulsing and subsequent Ti concentration did not improve the overall current when comparing the corrosion potential. Man et al. and Yan et al. have identified surface defects and inclusions as sources of decreasing corrosion resistance [95, 101]. In the work by M.I. Khan et al. [112], through transmission electron microscopy (TEM), the laser ablation process with Nd:YAG laser has shown lattice inclusions of submicron $Ti_2Ni$, which is a brittle intermetallic compound (IMC). The brittle $Ti_2Ni$ does not exhibit phase transformation and has been reported as crack initiation sites of rapidly solidified weld zones [38]. More $Ti_2Ni$ IMCs were also likely present in the 5 pulse specimens as a result of being more Ti-rich than the 3 pulse specimens. Therefore, the surface activity was suspected to have increased due to higher density of micro-cracks in the 5 pulse microstructure, leading to increase in corrosion current. However, further TEM, compositional, and microstructure analysis are required to confirm this theory.
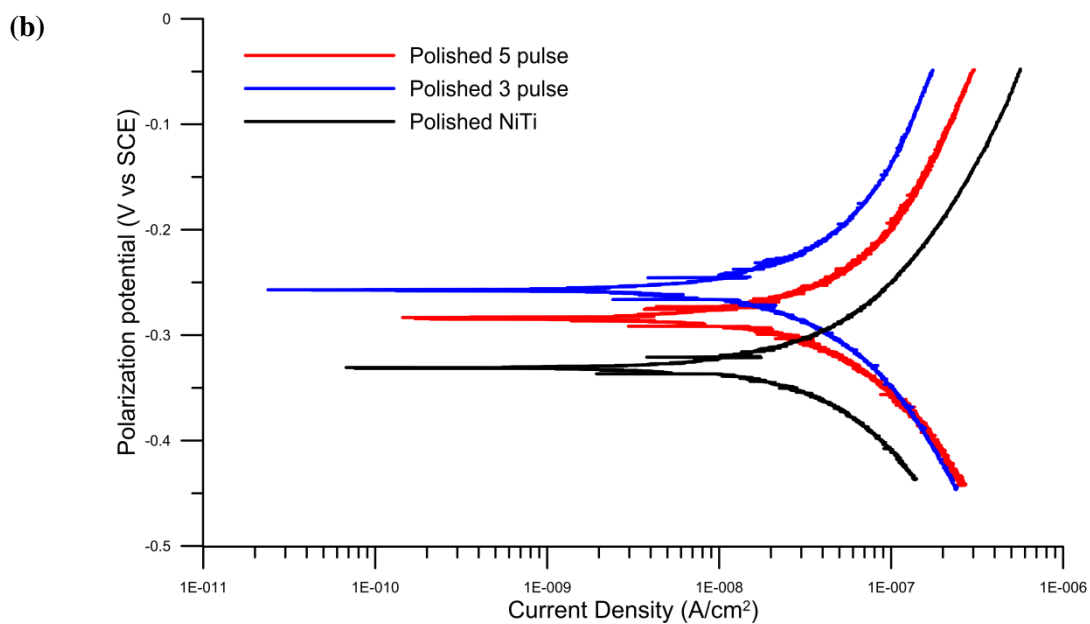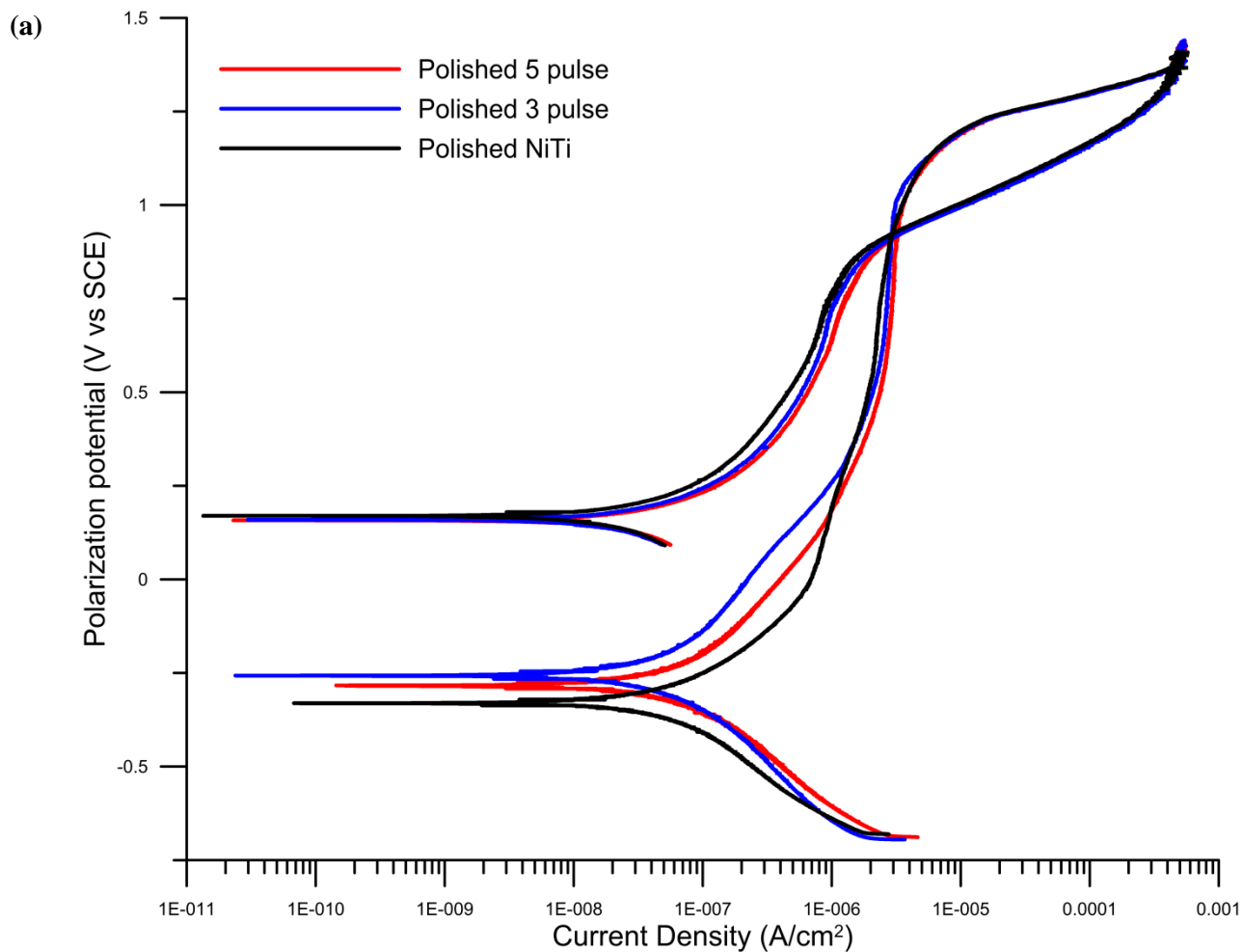
**Figure 4.7** (a) Cyclic polarization curve of polished base metal NiTi, polished 3 pulse sample, and polished 5 pulse sample. (b) Zoom-in of forward scan at voltage range of -0.45 to -.02 V vs SCE.

### 4.2.3   Effects of laser surface vapourization on Ni-ion release

Cumulative Ni ion concentrations in PBS over 18 days are listed Table 7, showing both laser processing protocols had achieved reduction in Ni ion release.   The finding corresponded to the Ni removal through increased laser ablation, in that decrease in Ni released matched the decrease in Ni concentration in the processed samples.   Decrease in Ni under the $TiO_2$ layer, shown in the XPS depth profile has been suggested to decrease Ni-ion release in other surface modification studies [63, 72]. However, the individual samplings were not above the lowest limits of detection (LLOD).   Thus, these preliminary results could only be used as a relative comparison.   Careful study with larger sample sizes and longer sampling time gaps is needed to obtain more accurate measurements of ion release.

**Table 7.** Cumulative experimental Ni ion release over 18 days with lower limits of detection (LLOD)
Note: The results are not statically significant and shown for general comparison only.

| Samples (Polished) | Ni ion (ppb) |
| --- | --- |
| BM | 24.3 |
| 3 pulse | 21.3 |
| 5 pulse | 18.2 |
| LLOD | 9.7 |

## 4.3      Chapter summary

This chapter demonstrated how Ti-rich NiTi can be created from Ni-rich NiTi strip through laser ablation. Furthermore, the corrosion behavior of these laser processed samples was investigated via cyclic polarization testing.   Increase in Ti:Ni ratio was first presented through EDX analysis of the cross-sectioned laser processed region.   XPS depth composition profile showed a noticeable decrease in Ni concentration, an increase in oxide thickness, and a rise in oxygen concentration in the surface layers of laser processed samples.   The improved surface oxide quality through laser processing was responsible for suppression of surface reactivity and lower corrosion rate at low potential passivation region in cyclic polarizations.   The increasingly Ti-rich surface was also suspected to be the reason for correspondingly lowered Ni ion release in ICP investigation; however, more precise instrumentation is required to accurately characterize the Ni ion release profile.

# Chapter 5

## 5. Summary of major findings and recommended future work

The purpose of this work is to further understand the MMM laser processing technique to improve design freedom and customization capabilities of medical devices. For that, the effect of laser processing on pseudoelastic response and the corrosion performance were investigated experimentally. More specifically, the studies was focused on addressing the following topics i) the effect of laser processing on microstructure and mechanical properties of medical grade SMA; ii) the subsequent mechanism of the precise augmentation of PE stress; and iii) the corrosion behaviour of laser processed medical grade NiTi surface. The major findings as a result of this thesis work are as follows:

## 5.1　　Microstructural, mechanical, and pseudoelastic augmentation

1. Laser energy input was demonstrated to cause solutionization of the local LPZ microstructure and remove the cold-work in the as-received BM. The LPZ possessed phase transformation temperatures and hardness similar to that of solutionized BM.

2. The change in PE during tensile cycling was proposed to be caused by the different deformation mechanisms of the LPZ and BM, which is suspected to be irreversible detwinning and SIM transformation, respectively. By increasing laser power and subsequently increasing the volume of the LPZ, the pseudoelastic stress of the wire was decreased.

3. Since the volume of LPZ was strongly linked to the decreased in PE in a predictable fashion, a phenomenological model for the pseudoelastic plateau augmentation was proposed. By identifying the relationship of the volume fractions of LPZ vs base metal and their respective tensile response, the pseudoelastic behaviour of laser processed wire could be predicted with 94% accuracy.

4. Using the pulsed fibre laser, augmentation of the local pseudoelasticity using the multiple memory material technology has been demonstrated. Furthermore, a phenomenological model was developed to enable predictability, high resolution, and accuracy. A proof of concept was successfully demonstrated where double pseudoelastic plateau were introduced in a monolithic NiTiCu wire.

## 5.2　　Corrosion behaviour and ion release of laser processed NiTi surface

1. Using the MMM processing method, application of laser pulse over the strip of Ni-rich NiTi induced preferential vapourization of Ni and created in a Ti-rich NiTi surface. The ratio of Ti:Ni in the laser processed region rises with increasing number of laser pulses.

2. XPS analysis revealed that the laser treated sample had thicker $TiO_2$ layer, higher Ti:Ni concentration beneath the oxide, and higher oxygen concentration in comparison to those of BM.

3. The laser treated surface was found to have improved corrosion potential and lower current when compared to BM NiTi. However, Ti-rich IMC formation was suspected to increased corrosion current when comparing moderately and heavily processed samples (i.e. 3 vs 5 pulses).

4. Reduction in Ni constituents and improved surface oxide quality showed proportional reduction in cumulative Ni ion release in preliminary results however, more accurate analytical method is required for confirmation.

## 5.3    Recommendations for future direction

Significant contribution to the science of SMAs has been made in this thesis project, in particular in the development of a new laser processing protocol for locally augmenting pseudoelastic behaviour. However, through developing this new protocol several questions have arisen. This thesis has provided answers to some of these questions and theories for the remainder. For proving all of the theories presented in this work more extensive research is, therefore, required. Below is a list of some future work that is recommended for the researchers who will build on this preliminary work in the future:

1. An in-depth microstructural investigation on the stress/strain interaction of the LPZ and BM is highly suggested to better predict the pseudoelasticity for industrial applications. A numerical modeling of the LPZ and BM interaction is also recommended to systematically predict the modification in PE.

2. Investigation on low cycle and high cycle fatigue of laser processed wires is recommended in order to further understand how partial change in microstructure impact the life time.

3. Particle-induced X-ray emission analysis is strongly suggested to gain accurate compositional analysis for NiTiCu, which would assist in correlating mechanical performance as well as corrosion behaviour

4. More systematic Ni-ion release experiments and cytotoxicity studies are suggested for MMM processed surfaces in order to validate that feasibility of surface modifications.

5. Scanning electrochemical microscopy mapping is highly suggested to map the surface reactivity of laser processed SMA in greater detail and to better understand possible galvanic effect which occurs at the BM-LPZ interface.

# References

[1]     W. J. Buehler, J. V. Gilfrich, and R. C. Wiley, "Effect of Low-Temperature Phase Changes on the Mechanical Properties of Alloys near Composition TiNi," *Journal of Applied Physics*, vol. 34, no. 5, p. 1475, 1963.

[2]     S. Shabalovskaya, J. Anderegg, and J. Van Humbeeck, "Critical overview of Nitinol surfaces and their modifications for medical applications.," *Acta biomaterialia*, vol. 4, no. 3, pp. 447–67, May 2008.

[3]     D. J. Hartl and D. C. Lagoudas, "Aerospace applications of shape memory alloys," *Proceedings of the Institution of Mechanical Engineers, Part G: Journal of Aerospace Engineering*, vol. 221, no. 4, pp. 535–552, Jan. 2007.

[4]     T. Duerig, A. Pelton, and D. Stöckel, "An overview of nitinol medical applications," *Materials Science and Engineering: A*, vol. 273, pp. 149–160, 1999.

[5]     M. Kohl, *Shape Memory Microactuators*. Springer Verlag, 2004.

[6]     C. T. Dotter, "Transluminally placed expandable graft prosthesis," U.S. Patent US 45035691985.

[7]     W. Nitinol, A. R. Pelton, D. Stockel, and T. Duerig, "Medical Uses of Nitinol," *Materials Science Forum*, vol. 327, pp. 63–70, 2000.

[8]     D. Stoeckel, A. Pelton, and T. Duerig, "Self-expanding nitinol stents: material and design considerations.," *European radiology*, vol. 14, no. 2, pp. 292–301, Feb. 2004.

[9]     G. F. Andreasen and R. E. Morrow, "Laboratory and clinical analyses of nitinol wire," *American Journal of Orthodontics*, vol. 73, no. 2, pp. 142–151, Feb. 1978.

[10]   G. F. Andreasen, "Method and system for orthodontic moving of teeth," U.S. Patent 40373241977.

[11]   F. Miura, M. Mogi, and Y. Ohura, "Japanese NiTi alloy wire: use of the direct electric resistance heat treatment method," *The European Journal of Orthodontics*, vol. 10, no. 3, pp. 187–191, 1988.

[12]   P. Sevilla, F. Martorell, C. Libenson, J. A. Planell, and F. J. Gil, "Laser welding of NiTi orthodontic archwires for selective force application," *Journal of Materials Science: Materials in Medicine*, vol. 19, no. 2, pp. 525–529, 2008.

[13]   W. Kiattiwongse, A. Khantachawana, and P. Santiwong, "Effect of Direct Electric Resistance Heat Treatment on Mechanical Properties of NiTi Orthodontic Arch Wires," *Advanced Materials Research*, vol. 55, pp. 249–252, 2008.

[14]   Y. Shima, K. Otsubo, T. Yoneyama, and K. Soma, "Anisotropic orthodontic force from the hollow super-elastic Ti-Ni alloy wire by transforming the wire cross-section," *Journal of Materials Science: Materials in Medicine*, vol. 13, no. 2, pp. 197–202, 2002.

[15]   G. B. Kauffman and I. Mayo, "The story of nitinol: the serendipitous discovery of the memory metal and its applications," *The chemical educator*, vol. 2, no. 2, pp. 1–21, 1997.

[16]     K. Otsuka and X. Ren, "Physical metallurgy of Ti–Ni-based shape memory alloys," *Progress in materials science*, vol. 50, no. 5, pp. 511–678, 2005.

[17]     A. Tuissi, S. Besseghini, T. Ranucci, F. Squatrito, and M. Pozzi, "Effect of Nd-YAG laser welding on the functional properties of the Ni–49.6 at.% Ti," *Materials Science and Engineering: A*, vol. 273, pp. 813–817, 1999.

[18]     A. Falvo, F. M. Furgiuele, and C. Maletta, "Laser welding of a NiTi alloy: Mechanical and shape memory behaviour," *Materials Science and Engineering: A*, vol. 412, no. 1, pp. 235–240, 2005.

[19]     M. I. Khan, S. K. Panda, and Y. Zhou, "Effects of welding parameters on the mechanical performance of laser welded Nitinol," *Materials Transactions*, vol. 49, no. 11, pp. 2702 – 2708, 2008.

[20]     C. W. Chan, H. C. Man, and T. M. Yue, "Effects of Process Parameters upon the Shape Memory and Pseudo-Elastic Behaviors of Laser-Welded NiTi Thin Foil," *Metallurgical and Materials Transactions A*, vol. 42, no. 8, pp. 2264–2270, 2011.

[21]     B. Tam, M. I. Khan, and Y. Zhou, "Mechanical and functional properties of laser-welded Ti-55.8 Wt Pct Ni nitinol wires," *Metallurgical and Materials Transactions A*, vol. 42, no. 8, pp. 2166–2175, 2011.

[22]     T. W. Duerig, D. E. Tolomeo, and M. Wholey, "An overview of superelastic stent design," *Minimally Invasive Therapy & Allied Technologies*, vol. 9, no. 3–4, pp. 235–246, 2000.

[23]     T. D. Creekmore and R. L. Kunik, "Straight wire: The next generation," *American Journal of Orthodontics & Dentofacial Orthopedics*, vol. 104, no. 1, pp. 8–20, 1993.

[24]     P. D. Wilkinson, P. S. Dysart, J. A. A. Hood, and G. P. Herbison, "Load-deflection characteristics of superelastic nickel-titanium orthodontic wires," *American Journal of Orthodontics and Dentofacial Orthopedics*, vol. 121, no. 5, pp. 483–495, 2002.

[25]     T. R. Meling and J. Odegaard, "On the variability of cross-sectional dimensions and torsional properties of rectangular nickel-titanium arch wires," *American Journal of Orthodontics and Dentofacial Orthopedics*, vol. 113, no. 5, pp. 546–557, May 1998.

[26]     M. I. Khan and Y. Zhou, "A method to locally modify shape memory and pseudoelastic properties," in *The international conference on shape memory and superelastic technologies (SMST Extended Abstracts). Pacific Grove, CA*, 2010, pp. 16–20.

[27]     M. I. Khan and Y. Zhou, "Effects of local phase conversion on the tensile loading of pulsed Nd: YAG laser processed Nitinol," *Materials Science and Engineering: A*, vol. 527, no. 23, pp. 6235–6238, 2010.

[28]     M. I. Khan, A. Pequegnat, and Y. Zhou, "Multiple memory shape memory alloys," *Advanced Functional Materials*, vol. In Press, 2013.

[29]     A. Pequegnat, M. Vlascov, M. Daly, Y. Zhou, and M. I. Khan, "Dynamic actuation of a multiple memory material processed nitinol linear actuator," 2011.

[30] M. Daly, A. Pequegnat, Y. N. Zhou, and M. I. Khan, "Fabrication of a novel laser-processed NiTi shape memory microgripper with enhanced thermomechanical functionality," *Smart Materials and Structures*, vol. 21, no. 4, p. 45018, 2012.

[31] X. J. Yan, D. Z. Yang, and X. P. Liu, "Corrosion behavior of a laser-welded NiTi shape memory alloy," *Materials Characterization*, vol. 58, no. 7, pp. 623–628, Jul. 2007.

[32] Y. T. Hsu, Y. R. Wang, S. K. Wu, and C. Chen, "Effect of CO2 Laser Welding on the Shape-Memory and Corrosion Characteristics of TiNi Alloys," *Metallurgical and Materials Transactions A*, vol. 32, no. March, pp. 569–576, 2001.

[33] C. W. Chan, H. C. Man, and T. M. Yue, "Effect of post-weld heat-treatment on the oxide film and corrosion behaviour of laser-welded shape memory NiTi wires," *Corrosion Science*, vol. 56, pp. 158–167, Mar. 2012.

[34] L. C. Chang and T. A. Read, "Plastic deformation and diffusionless phase changes in metals - The Gold-Cadmium beta phase," *Columbia University*, no. 191, pp. 147–152, 1952.

[35] M. W. Burkart and T. A. Read, "Diffusionless phase change in the Indium-Thallium system.," no. 197, pp. 1516–1524, 1953.

[36] Z. S. Basinski and J. W. Christian, "Crystallography ofdeformation by twin boundary movements in indium-thallium alloys," vol. 2, no. 1, pp. 101–113, 1954.

[37] T. B. Massalski, H. Okamoto, P. R. Subramanian, and L. Kacprzak, *Binary Alloy Phase Diagrams*, 2nd ed. Materials Park, OH, USA: ASM International, 1990, p. 2874.

[38] P. C. Hall, "Resistance welding Ti-rich Nitinol wire," in *International conference on Shape Memory and Superelastic Technologies (SMST)*, 2000, pp. 67–75.

[39] X. Huang and Y. Liu, "Effect of annealing on the transformation behavior and superelasticity of NiTi shape memory alloy," vol. 45, pp. 153–160, 2001.

[40] C. P. Frick, A. M. Ortega, J. Tyber, A. E. M. Maksound, H. J. Maier, Y. Liu, and K. Gall, "Thermal processing of polycrystalline NiTi shape memory alloys," *Materials Science and Engineering: A*, vol. 405, no. 1–2, pp. 34–49, Sep. 2005.

[41] T. W. Duerig, K. N. Melton, D. Stoeckel, C. M. Wayman, and D. Stockel, *Engineering Aspects of Shape Memory Alloys*. butterworth-Heinemann Ltd., 1990.

[42] D. C. Lagoudas, *Shape Memory Alloys*. New York, NY, USA: Springer, 2008.

[43] K. Otsuka and C. M. Wayman, *Shape Memory Materials*. Cambridge, U.K.: Cambridge University Press, 1999.

[44] H. C. Ling and K. Roy, "Stress-Induced Shape Changes and Shape Memory in the R and Martensite Transformations in Equiatomic NiTi," *Metallurgical and Materials Transactions*, vol. 12, no. 12, pp. 2101–2111, 1981.

[45]     T. H. Nam, T. Saburi, and K. Shimizu, "Cu-content dependence of shape memory characteristics in Ti-Ni-Cu alloys," *Mater Trans JIM*, vol. 31, no. 959, p. r5, 1990.

[46]     R. H. Bricknell, K. N. Melton, O. Mercier, and I. Introduction, "The Structure of NiTiCu Shape Memory Alloys," vol. 10, no. June, pp. 693–697, 1979.

[47]     Z. Wang, M. Gao, H. Tang, and X. Zeng, "Characterization of AZ31B wrought magnesium alloy joints welded by high power fiber laser," *Materials Characterization*, vol. 62, no. 10, pp. 943–951, 2011.

[48]     Y. Shugo, F. Hasegawa, and T. Honma, "Effects of copper addition on the martensitic transformation of TiNi alloy," in *Bulletin of the Research Institute of. Mineral Dressing and Metallurgy Tohoku University, vol37, no.1*, 1981, pp. 79–88.

[49]     S. MIYAZAKI, S. KIMURA, K. OTSUKA, and Y. SUZUKI, "The habit plane and transformation strains associated with the martensitic transformation in Ti-Ni single crystals," *Scripta metallurgica*, vol. 18, no. 9, pp. 883–888.

[50]     K. N. Melton and O. Mercier, "Deformation Behaviour of NiTi-based Alloys," *Metallurgical and Materials Transactions A*, vol. 9A, pp. 1487–1488, 1978.

[51]     J. Frenzel, E. P. George, a. Dlouhy, C. Somsen, M. F.-X. Wagner, and G. Eggeler, "Influence of Ni on martensitic phase transformations in NiTi shape memory alloys," *Acta Materialia*, vol. 58, no. 9, pp. 3444–3458, May 2010.

[52]     R. . Hamilton, H. Sehitoglu, Y. Chumlyakov, and H. . Maier, "Stress dependence of the hysteresis in single crystal NiTi alloys," *Acta Materialia*, vol. 52, no. 11, pp. 3383–3402, Jun. 2004.

[53]     T. Saburi, S. Nenno, Y. Nishimoto, and M. Zeniya, "Effects of Thermo-Mechanical Treatment on the Shape Memory Effect and the Pseudoelasticity of Ti--50. 2 Ni and Ti-47. 5 Ni--2. 5 Fe Alloys," *Tesu-to-Hagane (The Iron and Steel Institute of Japan)*, vol. 72, no. 6, pp. 571–578, 1986.

[54]     D. Treppmann, E. Hornbogen, and D. Wurzel, "The effect of combined recrystallization and precipitation process on the functional and structural properties in NiTi alloys," *Journal de physique. IV*, vol. 5, no. 8, pp. C8.569–C8.574.

[55]     J. a. Shaw and S. Kyriakides, "On the nucleation and propagation of phase transformation fronts in a NiTi alloy," *Acta Materialia*, vol. 45, no. 2, pp. 683–700, Feb. 1997.

[56]     P. Sittner, Y. Liu, and V. Novak, "On the origin of Lüders-like deformation of NiTi shape memory alloys," *Journal of the Mechanics and Physics of Solids*, vol. 53, no. 8, pp. 1719–1746, Aug. 2005.

[57]     R. Plietsch and K. Ehrlich, "Strength differential effect in pseudoelastic NiTi shape memory alloys," *Acta Materialia*, vol. 45, no. 6, pp. 2417–2424, 1997.

[58]     S. Miyazaki, Y. Ohmi, K. Otsuka, and Y. Suzuki, "Characteristics of deformation and Transformation Pseudoelasticity in Ti-Ni Alloys," *Le Journal de Physique Colloques*, vol. 43, no. C4, pp. C4–255–C4–260, Dec. 1982.

[59]    D. A. Porter and K. E. Easterling, *Phase Transformation in Metals and Alloys*. Van Nostrand Reinhold, 1981, pp. 9–10.

[60]    K. Otsuka and K. Shimizu, "Pseudoelasticity and shape memory effects in alloys," *International Metals Reviews*, vol. 31, no. 1, pp. 93–114, 1986.

[61]    W. Tang, "Thermodynamic Study of the Low-Temperature Phase B19 ' and the Martensitic Transformation in Near-Equiatomic Ti-Ni Shape Memory Alloys," *Metallurgical and Materials Transactions A*, vol. 28A, pp. 537–544, 1997.

[62]    W. Tang, R. Sandström, Z. G. Wei, and S. Miyazaki, "Experimental investigation and thermodynamic calculation of the Ti-Ni-Cu shape memory alloys," *Metallurgical and materials transactions A*, vol. 31, no. 10, pp. 2423–2430, 2000.

[63]    S. a Shabalovskaya, "Surface, corrosion and biocompatibility aspects of Nitinol as an implant material.," *Bio-medical materials and engineering*, vol. 12, no. 1, pp. 69–109, Jan. 2002.

[64]    D. R. Lide, Ed., *CRC Handbook of Chemistry and Physics*, 84th ed. Boca Raton, Florida, USA: CRC Press, Inc., 2003.

[65]    G. S. Firstov, R. G. Vitchev, H. Kumar, B. Blanpain, and J. Van Humbeeck, "Surface oxidation of NiTi shape memory alloy.," *Biomaterials*, vol. 23, no. 24, pp. 4863–71, Dec. 2002.

[66]    G. Rondelli and B. Vicentini, "Evaluation by electrochemical tests of the passive film stability of equiatomic Ni-Ti alloy also in presence of stress-induced martensite.," *Journal of biomedical materials research*, vol. 51, no. 1, pp. 47–54, Jul. 2000.

[67]    H. Huang, "Ion release from NiTi orthodontic wires in artificial saliva with various acidities," *Biomaterials*, vol. 24, no. 20, pp. 3585–3592, Sep. 2003.

[68]    O. Cissé, O. Savadogo, M. Wu, and L. Yahia, "Effect of surface treatment of NiTi alloy on its corrosion behavior in Hanks' solution.," *Journal of biomedical materials research*, vol. 61, no. 3, pp. 339–45, Sep. 2002.

[69]    M. Arndt, a. Brück, T. Scully, a. Jäger, and C. Bourauel, "Nickel ion release from orthodontic NiTi wires under simulation of realistic in-situ conditions," *Journal of Materials Science*, vol. 40, no. 14, pp. 3659–3667, Jul. 2005.

[70]    L. Giner, M. Cortada, O. Rustullet, F. Gil, J. Fernandez-Truel, and D. Rodriguez, "Rev implantol," *Orale Implantodontie*, vol. 29, pp. 35–41, 1998.

[71]    H. Kerosuo, A. Kullaa, E. Kerosuo, L. Kanerva, and A. Hensten-Pettersen, "Nickel allergy in adolescents in relation to orthodontic treatment and piercing of ears.," *American journal of orthodontics and dentofacial orthopedics*, vol. 109, no. 2, pp. 148–54, Feb. 1996.

[72]    B. Fatiha, E. Feninat, G. Laroche, M. Fiset, and D. Mantovani, "Shape Memory Materials for Biomedical Applications," no. 3, pp. 91–104, 2002.

[73]     M. Berger-Gorbet, B. Broxup, C. Rivard, and L. H. Yahia, "Biocompatibility testing of NiTi screws using immunohistochemistry on sections containing metallic implants.," *Journal of biomedical materials research*, vol. 32, no. 2, pp. 243–8, Oct. 1996.

[74]     S. A. Shabalovskaya, J. Anderegg, F. Laab, P. A. Thiel, and G. Rondelli, "Surface conditions of Nitinol wires, tubing, and as-cast alloys. The effect of chemical etching, aging in boiling water, and heat treatment.," *Journal of biomedical materials research. Part B, Applied biomaterials*, vol. 65, no. 1, pp. 193–203, Apr. 2003.

[75]     B. Clarke, W. Carroll, Y. Rochev, M. Hynes, D. Bradley, D. Plumley, and C. E. T. Al, "Influence of nitinol wire surface treatment on oxide thickness and composition and its subsequent effect on corrosion resistance and nickel ion release," pp. 3–12, 2006.

[76]     S. a Shabalovskaya, G. C. Rondelli, A. L. Undisz, J. W. Anderegg, T. D. Burleigh, and M. E. Rettenmayr, "The electrochemical characteristics of native Nitinol surfaces.," *Biomaterials*, vol. 30, no. 22, pp. 3662–71, Aug. 2009.

[77]     S. Barison, S. Cattarin, S. Daolio, M. Musiani, and A. Tuissi, "Characterisation of surface oxidation of nickel–titanium alloy by ion-beam and electrochemical techniques," *Electrochimica Acta*, vol. 50, no. 1, pp. 11–18, Nov. 2004.

[78]     C. L. Chu, C. Y. Chung, and P. K. Chu, "Surface oxidation of NiTi shape memory alloy in a boiling aqueous solution containing hydrogen peroxide," *Materials Science and Engineering: A*, vol. 417, no. 1–2, pp. 104–109, Feb. 2006.

[79]     C. L. Chu, T. Hu, S. L. Wu, Y. S. Dong, L. H. Yin, Y. P. Pu, P. H. Lin, C. Y. Chung, K. W. K. Yeung, and P. K. Chu, "Surface structure and properties of biomedical NiTi shape memory alloy after Fenton's oxidation.," *Acta biomaterialia*, vol. 3, no. 5, pp. 795–806, Sep. 2007.

[80]     S. a. Shabalovskaya and J. W. Anderegg, "Surface spectroscopic characterization of TiNi nearly equiatomic shape memory alloys for implants," *Journal of Vacuum Science & Technology A: Vacuum, Surfaces, and Films*, vol. 13, no. 5, p. 2624, Sep. 1995.

[81]     L. Tan and W. C. Crone, "Surface characterization of NiTi modified by plasma source ion implantation," *Acta Materialia*, vol. 50, no. 18, pp. 4449–4460, Oct. 2002.

[82]     R. W. Y. Poon, K. W. K. Yeung, X. Y. Liu, P. K. Chu, C. Y. Chung, W. W. Lu, K. M. C. Cheung, and D. Chan, "Carbon plasma immersion ion implantation of nickel-titanium shape memory alloys.," *Biomaterials*, vol. 26, no. 15, pp. 2265–72, May 2005.

[83]     D. M. Grant, S. M. Green, and J. V. Wood, "The surface performance of shot peened and ion implanted NiTi shape memory alloy," *Acta Metallurgica et Materialia*, vol. 43, no. 3, pp. 1045–1051, Mar. 1995.

[84]     E. Scientific, P. Company, K. Nag, A. Chakravorty, and A. Introduction, "Monovalent, trivalent and tetravalent nickel," vol. 33, pp. 87–147, 1980.

[85]     S. A. Shabalovskaya, J. Cunnick, J. W. Anderegg, B. Harmon, and R. Sachdeva, "Preliminary data onin vitrostudies of proliferation rat spleen cell response to Ni-Ti surface characterized using

ESCA analysis," in *First Int. Conf. Shape Memory and Superelastic Technologies*, 1994, pp. 209–215.

[86]    S. Shabalovskaya, J. Anrderegg, and J. Cunnick, "X-ray spectroscopicin vitrostudy of porous NiTi," in *Second Int. Conf. Shape Memory and Superelastic Technologies*, 1997, pp. 401–406.

[87]    D. Hodgson and S. Russell, "Nitinol melting, manufacture and fabrication," *Minimally Invasive Therapy & Allied Technologies*, vol. 9, no. 2, pp. 61–65, Jan. 2000.

[88]    D. a. Miller and D. C. Lagoudas, "Influence of cold work and heat treatment on the shape memory effect and plastic strain development of NiTi," *Materials Science and Engineering: A*, vol. 308, no. 1–2, pp. 161–175, Jun. 2001.

[89]    H. Matsumoto, "Transformation behaviour of NiTi in relation to thermal cycling and deformation," *Physica B,*, vol. 190, pp. 115–120, 1993.

[90]    Y. Zheng, F. Jiang, L. Li, H. Yang, and Y. Liu, "Effect of ageing treatment on the transformation behaviour of Ti–50.9at.% Ni alloy," *Acta Materialia*, vol. 56, no. 4, pp. 736–745, Feb. 2008.

[91]    A. R. Pelton, J. Dicellol, and S. Miyazaki, "Optimisation of processing and properties of medical grade Nitinol wire," *Minimally Invasive Therapy Allied Technologies*, vol. 9, no. 1, pp. 107–118, 2000.

[92]    J. I. Kim, Y. Liu, and S. Miyazaki, "Ageing-induced two-stage R-phase transformation in Ti–50.9at.%Ni," *Acta Materialia*, vol. 52, no. 2, pp. 487–499, Jan. 2004.

[93]    H. C. Man, Z. D. Cui, and T. M. Yue, "Corrosion properties of laser surface melted NiTi shape memory alloy," *Scripta Materialia*, vol. 45, no. 12, pp. 1447–1453, Dec. 2001.

[94]    P. Schlossmacher, T. Haas, and A. Schüssler, "Laser-Welding of a Ni-Rich TiNi Shape Memory Alloy: Mechanical Behavior," *J. Phys. IV France*, vol. 7, no. 1 997, pp. 251–256, 1997.

[95]    Y. Ogata, M. Takatugu, T. Kunimasa, K. Uenishi, and K. F. Kobayashi, "Tensile Strength and Pseudo-elasticity of YAG Laser Spot Melted Ti-Ni Shape Memory Alloy Wires," *Materials Transactions*, vol. 45, no. 4, pp. 1070–1076, 2004.

[96]    C. W. Chan, H. C. Man, and T. M. Yue, "Effect of Postweld Heat Treatment on the Microstructure and Cyclic Deformation Behavior of Laser-Welded NiTi-Shape Memory Wires," *Metallurgical and Materials Transactions A*, vol. 43, no. 6, pp. 1956–1965, Jan. 2012.

[97]    M. Daly, "Thermomechanical response of laser processed nickel-titanium shape memory alloy," University of Waterloo, 2012.

[98]    S. A. Shabalovskaya, "Physicochemical and biological aspects of Nitinol as a biomaterial," *International materials reviews*, vol. 46, no. 5, pp. 233–250, 2001.

[99]    H. Sakamoto, K. Uematsu, M. Momota, S. Tanabe, T. Suzuki, and T. Endo, "Guide wire for catheter," U.S. Patent 49254451990.

[100] R. G. Daniel Cluff, Stephen Corbin, "Powder metallurgy fabrication of hybrid monolithic SMA actuators," in *Proceedings of Cansmart 2009*.

[101] S. Brook, "Shape memory TiNi synthesis from elemental powders," vol. 188, pp. 291–300, 1994.

[102] B. V. Krishna, S. Bose, and A. Bandyopadhyay, "Laser Processing of Net-Shape NiTi Shape Memory Alloy," *Metallurgical and Materials Transactions A*, vol. 38, no. 5, pp. 1096–1103, Apr. 2007.

[103] T. Bormann, R. Schumacher, B. Müller, M. Mertmann, and M. Wild, "Tailoring Selective Laser Melting Process Parameters for NiTi Implants," *Journal of Materials Engineering and Performance*, vol. 21, no. 12, pp. 2519–2524, Jul. 2012.

[104] Y. B. Wang, Y. F. Zheng, and Y. Liu, "Effect of short-time direct current heating on phase transformation and superelasticity of Ti–50.8at.%Ni alloy," *Journal of Alloys and Compounds*, vol. 477, no. 1–2, pp. 764–767, 2009.

[105] D. J. Wever, a G. Veldhuizen, M. M. Sanders, J. M. Schakenraad, and J. R. van Horn, "Cytotoxic, allergic and genotoxic activity of a nickel-titanium alloy.," *Biomaterials*, vol. 18, no. 16, pp. 1115–20, Aug. 1997.

[106] F. Villermaux, M. Tabrizian, L. Yahia, M. Meunier, and D. L. Piron, "Excimer laser treatment of NiTi shape memory alloy biomaterials," *Applied Surface Science*, vol. 109–110, pp. 62–66, Feb. 1997.

[107] L. Quintino, A. Costa, R. Miranda, D. Yapp, V. Kumar, and C. J. Kong, "Welding with high power fiber lasers–A preliminary study," *Materials & Design*, vol. 28, no. 4, pp. 1231–1237, 2007.

[108] "Dentistry - Wires for use in orthodontics," *ISO Standard 15841*.

[109] Z. Xu, K. Natesan, C. B. Reed, and D. L. Smith, "Procedure development of laser welding of V-4Cr-4Ti alloy," vol. 18, no. September 2000, pp. 231–236, 2001.

[110] Y. Kawahito, M. Mizutani, and S. Katayama, "High quality welding of stainless steel with 10 kW high power fibre laser," *Science and Technology of Welding and Joining*, vol. 14, no. 4, pp. 288–294, May 2009.

[111] Q. Meng, Y. Liu, H. Yang, B. S. Shariat, and T. Nam, "Functionally graded NiTi strips prepared by laser surface anneal," *Acta Materialia*, vol. 60, no. 4, pp. 1658–1668, Feb. 2012.

[112] M. I. Khan, "Pulse Nd:YAG Laser Processing of Nitinol," University of Waterloo, 2011.

[113] B. Tam, A. Pequegnat, M. I. Khan, and Y. Zhou, "Resistance Microwelding of Ti-55.8 wt pct Ni Nitinol Wires and the Effects of Pseudoelasticity," *Metallurgical and Materials Transactions A*, vol. 43, no. 8, pp. 2969–2978, Mar. 2012.

[114] B. Strnadel, S. Ohashi, H. Ohtsuka, T. Ishihara, S. Miyazaki, and B. Strnadep, "Cyclic stress-strain characteristics of Ti-Ni and Ti-Ni-Cu shape memory alloys," *Materials Science and Engineering: A*, vol. 202, no. 1, pp. 148–156, 1995.

# Appendix I.
## Experimental Data for Cyclic polarization presented in Chapter 4..

The following are the cyclic potentiodynamic polarization plots as a result of experiments described in section 4.1.2.



**Figure A.1** Cyclic polarization curve of polished base metal NiTi trial 1 to 4

**Table A.1.** Summary of key cyclic polarization values of NiTi BM trials

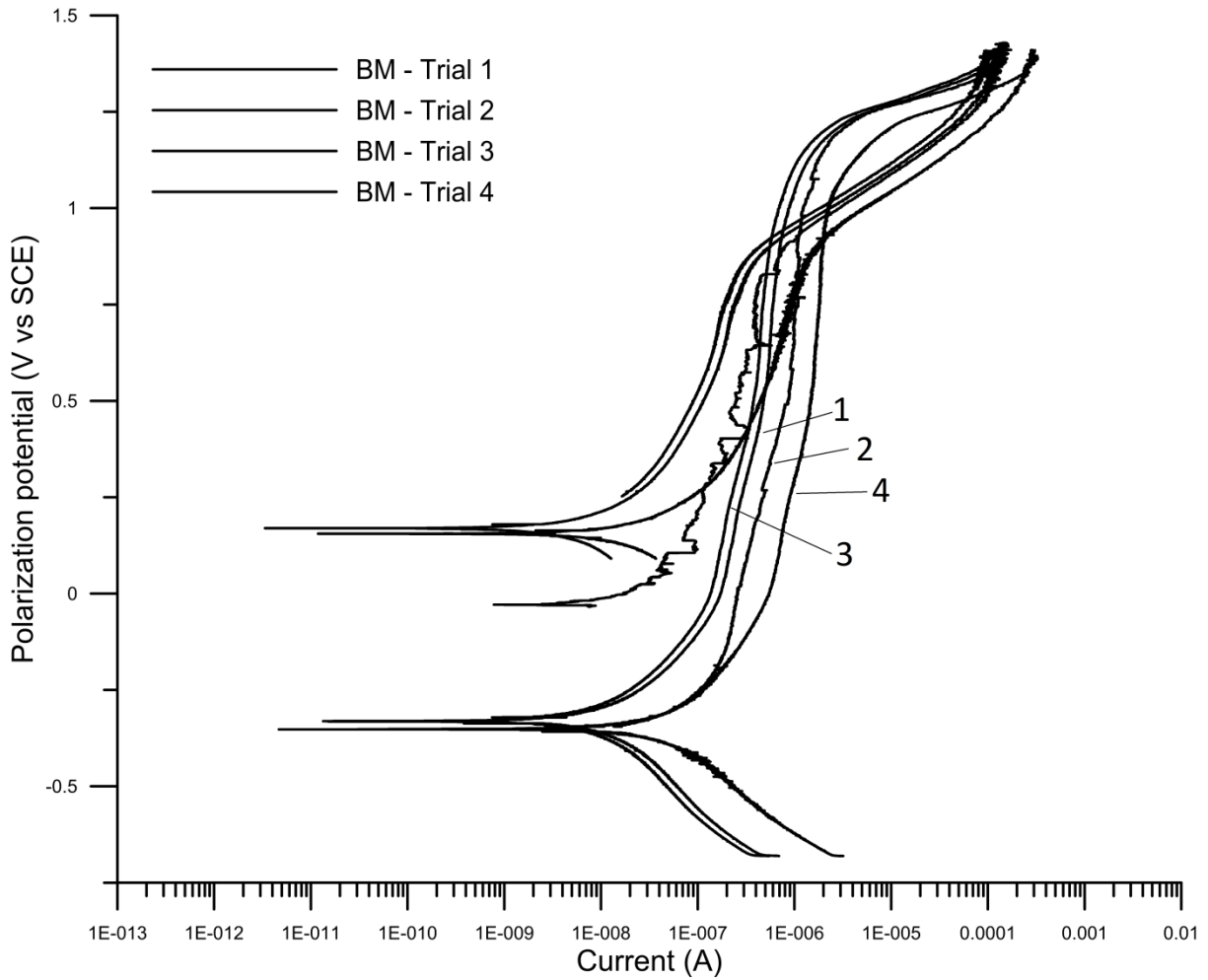| Samples | $E_{corr}$(V vs SCE) | $E_{break}$(V vs SCE) | $E_{prot}$(V vs SCE) | $I_{prot}$ (A) | I (A) at 0.05V vs SCE |
|---|---|---|---|---|---|
| **BM Trial 1** | -0.33 | 1.21 | 0.90 | $7.03 \times 10^{-7}$ | $2.00 \times 10^{-7}$ |
| **BM Trial 2** | -0.35 | 1.21 | 0.92 | $1.07 \times 10^{-6}$ | $2.90 \times 10^{-7}$ |
| **BM Trial 3** | -0.33 | 1.20 | 0.90 | $6.53 \times 10^{-7}$ | $1.60 \times 10^{-7}$ |
| **BM Trial 4** | -0.35 | 1.16 | 0.89 | $2.90 \times 10^{-6}$ | $9.60 \times 10^{-7}$ |
| **Average** | -0.34 | 1.195 | 0.9025 | $1.33 \times 10^{-6}$ | $4.03 \times 10^{-7}$ |
| **Std. Dev.** | 0.01 | 0.020 | 0.011 | $9.20 \times 10^{-7}$ | $3.25 \times 10^{-7}$ |

**Figure A.2** Cyclic polarization curve of polished 3 pulse sample trial 1 to 4

**Table A.2.** Summary of key cyclic polarization values of 3 pulse sample trials

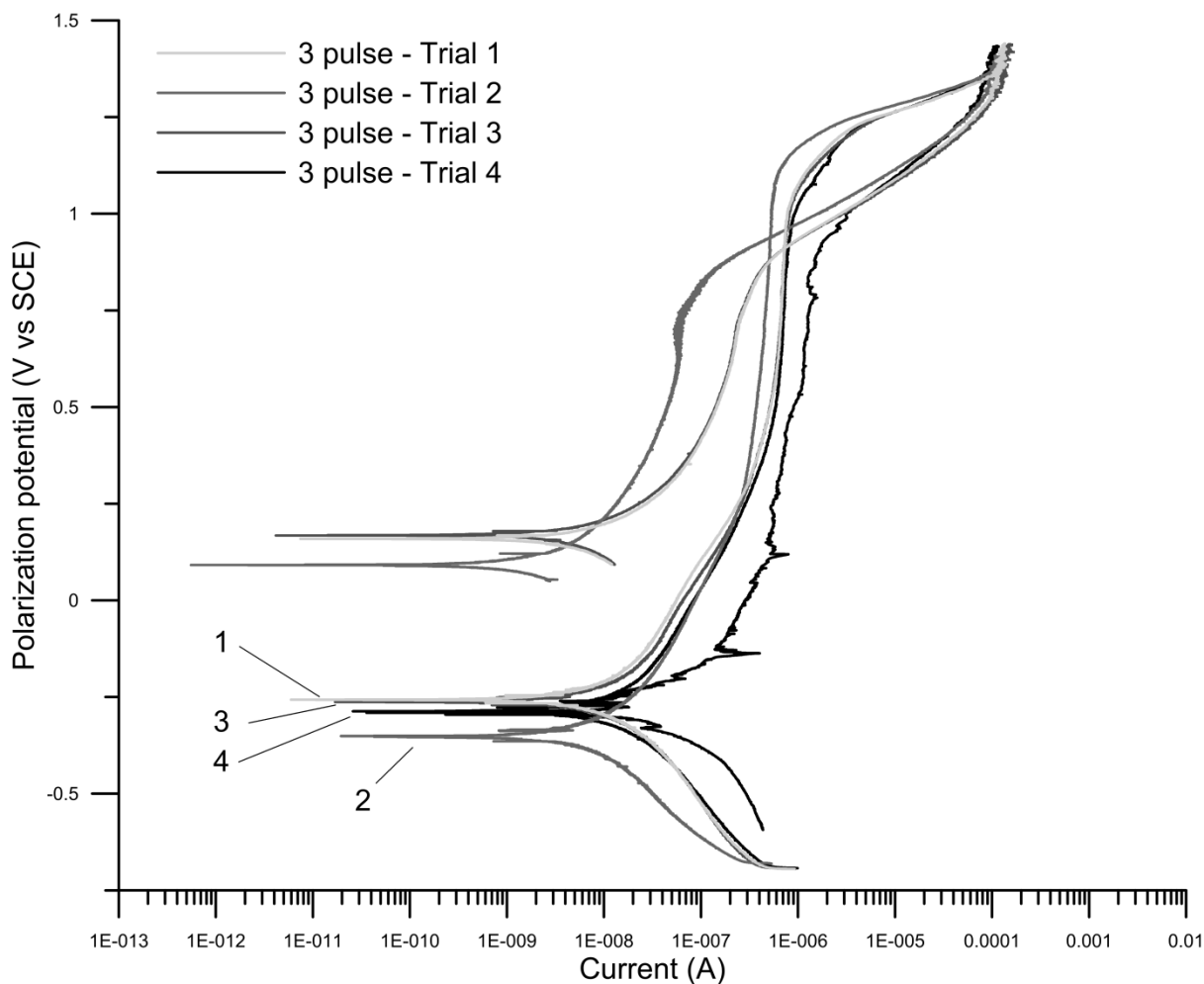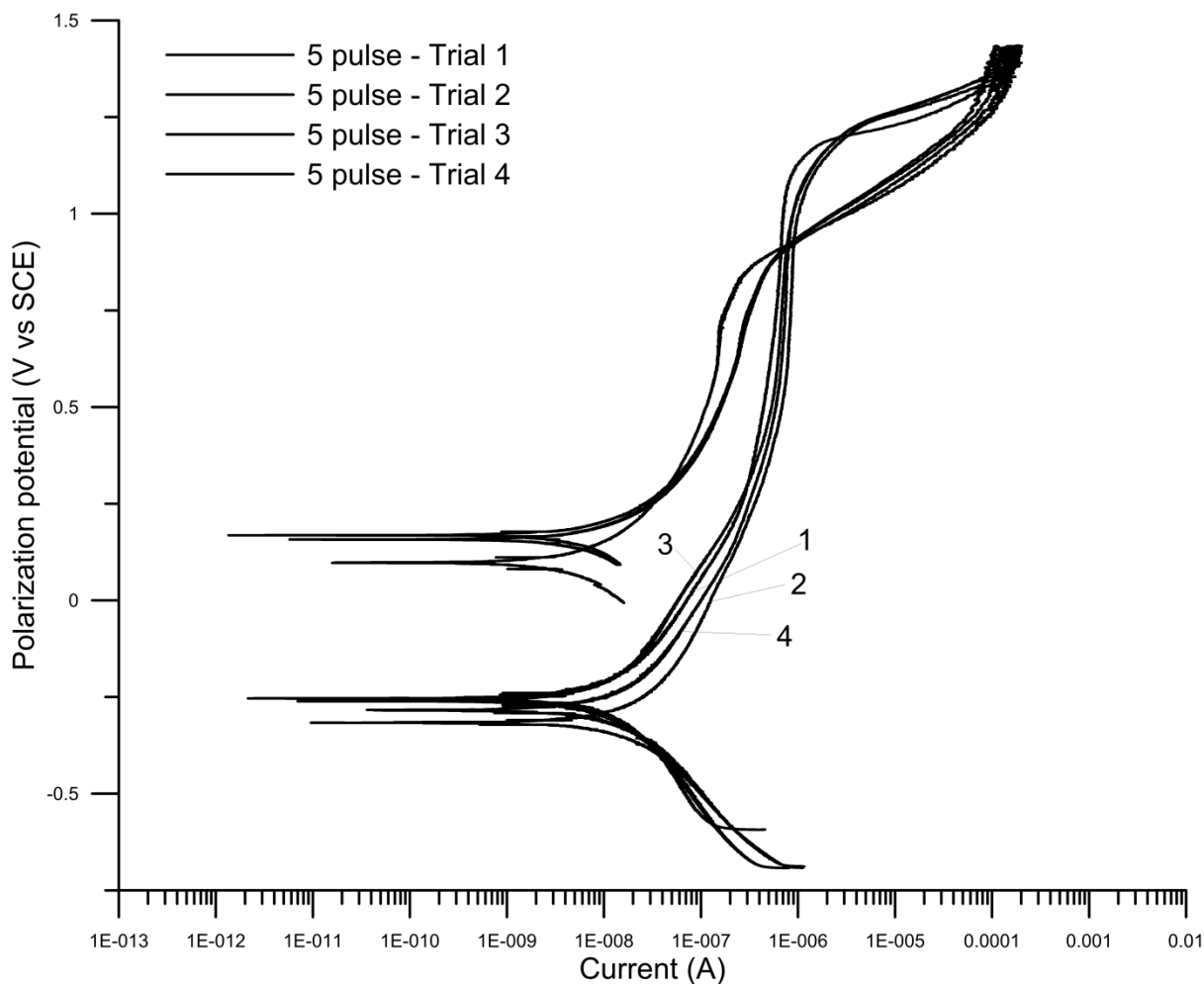| Samples | $E_{corr}$(V vs SCE) | $E_{break}$(V vs SCE) | $E_{prot}$(V vs SCE) | $I_{prot}$ (A) | I (A) at 0.05V vs SCE |
|---|---|---|---|---|---|
| **3 pulse Trial 1** | -0.26 | 1.20 | 0.90 | $7.32 \times 10^{-7}$ | $7.61 \times 10^{-8}$ |
| **3 pulse Trial 2** | -0.35 | 1.19 | 0.92 | $5.16 \times 10^{-7}$ | $7.51 \times 10^{-8}$ |
| **3 pulse Trial 3** | -0.26 | 1.21 | 0.90 | $7.33 \times 10^{-7}$ | $7.41 \times 10^{-8}$ |
| **3 pulse Trial 4** | -0.29 | 1.20 | n/a | n/a | $1.16 \times 10^{-7}$ |
| **Average** | -0.29 | 1.20 | 0.91 | $6.60 \times 10^{-7}$ | $7.51 \times 10^{-8}$ |
| **Std. Dev.** | 0.037 | 0.0071 | 0.0094 | $1.02 \times 10^{-7}$ | $8.16 \times 10^{-10}$ |

**Figure A.3** Cyclic polarization curve of polished 5 pulse sample trial 1 to 4

**Table A.3.** Summary of key cyclic polarization values of 5 pulse sample trials

| Samples | $E_{corr}$(V vs SCE) | $E_{break}$(V vs SCE) | $E_{prot}$(V vs SCE) | $I_{prot}$ (A) | I (A) at 0.05V vs SCE |
|---|---|---|---|---|---|
| **5 pulse Trial 1** | -0.25 | 1.16 | 0.90 | $6.67 \times 10^{-7}$ | $9.84 \times 10^{-8}$ |
| **5 pulse Trial 2** | -3.18 | 1.19 | 0.91 | $8.97 \times 10^{-7}$ | $1.05 \times 10^{-7}$ |
| **5 pulse Trial 3** | -0.26 | 1.19 | 0.90 | $7.63 \times 10^{-7}$ | $7.88 \times 10^{-8}$ |
| **5 pulse Trial 4** | -2.61 | 1.18 | 0.90 | $7.63 \times 10^{-7}$ | $1.55 \times 10^{-7}$ |
| **Average** | -0.27 | 1.18 | 0.90 | $7.73 \times 10^{-7}$ | $1.09 \times 10^{-7}$ |
| **Std. Dev.** | 0.027 | 0.012 | 0.0043 | $8.19 \times 10^{-8}$ | $2.81 \times 10^{-8}$ |

# Glossary of Terms

| | |
|---|---|
| $\varepsilon$ | Tensile strain [%] |
| $\varepsilon_r$ | Retained tensile strain after mechanical loading/unloading of a martensitic nickel-titanium specimen [%] |
| $\sigma$ | Tensile stress [MPa] |
| $\sigma_m$ | Stress required to induce a martensitic transformation [MPa] |
| $\sigma_r$ | Reverse martensitic transformation stress [MPa] |
| $\sigma_s$ | Slip stress [MPa] |
| $\tau$ | Shear stress [MPa] |
| $D_1$ | Laser spot diameter[μm] |
| $D_2$ | Tip width of laser processed zone [μm] |
| H | Penetration depth of laser processed zone |
| $A_f$ | Austenite finish phase transformation temperature [°C] |
| $A_s$ | Austenite start phase transformation temperature [°C] |
| BM | Base metal |
| DSC | Differential scanning calorimetry |
| $E_{corr}$ | Corrosion potential or equilibrium potential |
| $E_{break}$ | Breakdown potential |
| $E_{prot}$ | Protection potential |
| EDX | Emery dispersive X-ray |
| FPF | Forward pseudoelastic force |
| ICP AES | Inductively coupled plasma atomic emission spectroscopy |
| IMC | Intermetallic compound |
| LPZ | Laser processed zone |
| $M_d$ | Temperatures at which shape memory alloy deforms through slip rather than stress-induced martensitic transformation |
| $M_f$ | Martensite finish phase transformation temperature [°C] |
| NiTi | Nickel titanium |
| NiTiCu | Nickel titanium copper |
| PE | Pseudoelasticity or Pseudoelastic effect |
| RPF | Reverse pseudoelastic force |
| SBM | Static base metal zone in between two laser processed zones |

SEM        Scanning electron microscope

SIM        Stress induced martensite

SMA        Shape memory alloy

TEM        Transmission electron microscopy

XRD        X-ray diffraction